MANIPULATING THE ELECTROSPINNING PROCESS VIA STATIC MAGNETIC FIELDS

A Thesis

Presented to the Faculty of the Graduate School

of Cornell University

in Partial Fulfillment of the Requirements for the Degree of

Master of Science

by

Alejandra Andere Jones

February 2010

ABSTRACT

In this thesis we explore the effect of applying a static magnetic field on the development of both the electrified jet and the whipping instability during electrospinning. The effect that viscosity, volumetric flow, conductivity, and electric field play on this process is also reported. Additionally, a preliminary study on the effect that sonication and particle addition have on the rheological properties of polymer solutions is presented.

Magnetic nanoparticles of magnetite (Fe_3O_4) and cobalt ferrite ($CoFe_2O_4$) where suspended in poly(ethylene oxide) (PEO) solutions. These particles where dispersed by either sonication or mechanical stirring. Steady state and oscillatory rheological measurements were performed on the different solutions. Chain scission caused by sonication is reported. Additionally, the effect that particle addition has on the entanglement structure of polymer molecules is reported.

Solutions were electrospun at volumetric flows of 0.6, 0.9 and 1.2mL/hr. At each volumetric flow the electric field was varied from 20 to 100kV/m in steps of 20kV/m. High speed imaging was employed to study the behavior of the electrified jet at the exit of the capillary. These images showed that both solution viscosity and applied electric are the key parameters on determining the onset of the whipping instability. Scanning Electron Microscopy (SEM) was used to examine the final fiber morphology and size. Again, solution viscosity and electric field were the key parameters in determining the size of the resulting fibers.

For each volumetric flow/electric field combination, the electrospinning was carried with and without the presence of a static magnetic field of 3725Ga. High speed imaging was employed to study the effect of the static magnetic field on the electrospinning process. An increase in the electric field required for the electrified jet to initiate was observed when applying the static field. This was attributed to a

magnetic force created between the magnet and the polymer/nanoparticles solution which must be overcome by the electric field. Furthermore, at low electric fields an increase in the onset of the whipping instability is reported. This is related to the magnetoviscous effect, which is known to cause an increase in a magnetic fluid's viscosity. Finally, potential ideas for future work are proposed.

BIOGRAPHICAL SKETCH

Alejandra Andere Jones was born in San Luis Potosi, SLP, Mexico on July 7, 1984. Her father is Jesus Andere Siade, a salesman and Civil Engineer. Her mother is Constance M. Jones Islas, a professional painter and dedicated housewife. Alejandra grew up in San Luis Potosi with her sister Cristina. She attended the Motolinia catholic school and spent her afternoons swimming. After middle school, she attended the "Instituto Tecnologico de Estudios Superiores de Monterrey" (ITESM), were she had the opportunity of studying abroad for one semester in Calgary, Canada.

On August 2002 Alejandra began her undergraduate studies as a Chemical Engineer at the "Universidad Autonoma de San Luis Potosi" (UASLP). Throughout her studies, she received the "Student of Excellence" award by the UASLP during the year 2006 and 2007. In 2006 she was also accredited with a mention from the Mexican Institute of Chemical Engineers (IMIC) for her outstanding GPA. Additionally, she was involved with the faculty student committee during the organization of academic and social events. Alejandra completed her Bachelor of Science in Chemical Engineering in May 2007.

In August 2007, Alejandra moved to Ithaca, New York to attend Cornell University to pursue her Masters in Fiber Science.

ACKNOWLEDGEMENTS

First of all, I would like to thank my family, Alejandro, and my friends (here and at home). Your continuous support and encouragement is what made me hold to the end.

I would like to acknowledge my research advisor, Dr. Juan Hinestroza. The opportunity he provided me allowed me to grow in both personal and professional levels.

I would also like to thank my committee member, Dr. Bruce Van Dover, for his guidance and support during the process. In addition, I would like to thank his graduate student, Jon Petrie, for his help.

I would like to thank my fellow graduate students and group members, Camila Flor, Christina Diaz, Karmann Mills, Dr. Laura McJilton and Dr. Yan Vivian Li. Whenever I needed help, these people where always there to support me.

I would like to thank Dr. Carlos Rinaldi and Dr. Carola Barrera for hosting me in Puerto Rico and providing me with the magnetic material employed in this study.

I would like to thank Dr. Itai Cohen and his graduate students Leif Gibbens and Jon Savage for lending me their high speed camera and helping me with the setup.

I would like to thank the National Science Foundation (CAREER – CMMI 0644012) for funding this project. I would also like to thank the Cornell Center for Materials Research (CCMR) for the use of their facilities.

TABLE OF CONTENTS

LIST OF FIGURES

LIST OF TABLES

1. INTRODUCTION

The inclusion of magnetic nanoparticles into polymeric fibers offers potential applications in a wide range of areas. These applications are possible because the resulting nanofibers retain the magnetic properties of their precursor solutions. Depending on the nature of the filler nanofibers with either ferromagnetic or superparamagnetic behavior can be created. Some of the possible applications of these materials include ultrahigh density data storage materials [1], magnetic filters [2], biomedical [33] and anti counterfeiting applications [4].

Electrospinning has been widely employed as a primary method for producing nanoparticle composite fibers. One of the main parameters that affects this process is the viscosity of the precursor polymer solution [5]. For this reason, electrospinning may benefit from alternative ways to manipulate this parameter. Literature shows that the viscosity of a solution loaded with magnetic nanoparticles can be affected by an external magnetic field [6, 7]. When applying a DC field during the flow of a ferrofluid, an increase in its viscosity has been observed. Oppositely an alternating magnetic field has been reported to have the opposite effect, showing a decrease in the fluid's viscosity. This phenomenon is better known as the "Negative viscosity effect"

In this thesis, we present the first evidence that the electrospinning process can be manipulated by applying a magnetic field while processing polymer solutions filled with magnetic particles. In particular, the effect of a static magnet field was studied.

In Chapter 2 we discuss the pertinent literature for the electrospinning of magnetic composite fibers. First we look into the electrospinning process and the effect of processing parameters such as viscosity, conductivity, surface tension, volumetric flow, applied voltage, and electric field. Next we examine the magnetic properties and synthesis mechanisms for different types of ferromagnetic and superparamagnetic nanoparticles. Finally, theoretical and experimental results of applying either a static

or alternating magnetic field on the flow of magnetic fluids are reviewed. We discuss the theoretical results derived by Shliomis [8] as well as the experimental verification by Bacri *et al.*[6]. These two seminal papers constitute the basis for the development of the theories on negative viscosity.

Chapter 3 describes the experimental approach employed in this study. Solutions with various amounts of magnetic nanoparticles were prepared. These solutions were electrospun while varying process parameters including volumetric flow, electric field, and magnetic field. High speed imaging from the tip of the capillary allowed us to assess the effect that these parameters have on the electrospinning process.

In chapter four we present the main findings of this study. First, we discuss the effect that particle addition had on polymer degradation induced by sonication. Additionally, the effect of particle loading on the rheological properties of the polymer solutions was also studied. Next, we discuss the effect that different processing parameters have on both the development of the whipping instability and the resulting fibers. Finally, we discussed the effect of applying a static magnetic field on the evolution of the jet during electrospinning. Conclusions and recommendations for future work are presented in chapter five and six.

2. LITERATURE REVIEW

2.1 Electrospinning

Electrospinning is a simple and versatile method able to yield well defined polymeric fibers with diameters in the range of nanometers, which are at least one or two orders of magnitude smaller than those produced by conventional melt or solution spinning [5, 9]. The first patent on electrospinning of polymer fibers was issued to Formhals [10] in 1938, but it was not until the 1990's that this technique attracted substantial interest mostly from academic research groups. Sudden interest in electrospun nanofibers arose because of their potential for a variety of applications due to their high surface area to volume ratio, high porosity and large length to diameter ratio [11, 12].

2.1.1 Process Description

During the electrospinning process a polymer solution or melt is contained in a reservoir, usually a syringe, which is connected to a metal capillary tip. An electric field is created by applying a potential difference (usually in the range of 0-30kV) between the tip of the capillary and a grounded collector placed at a given distance [13]. The polymer in solution typically consists of molecular weights from 100,000 g/mol to several million at concentrations ranging from 5% to 15% [14]. This solution is usually fed at a constant rate using an automated pump, making the collection process continuous. An illustration of a typical laboratory electrospinning setup is shown in Figure 1.

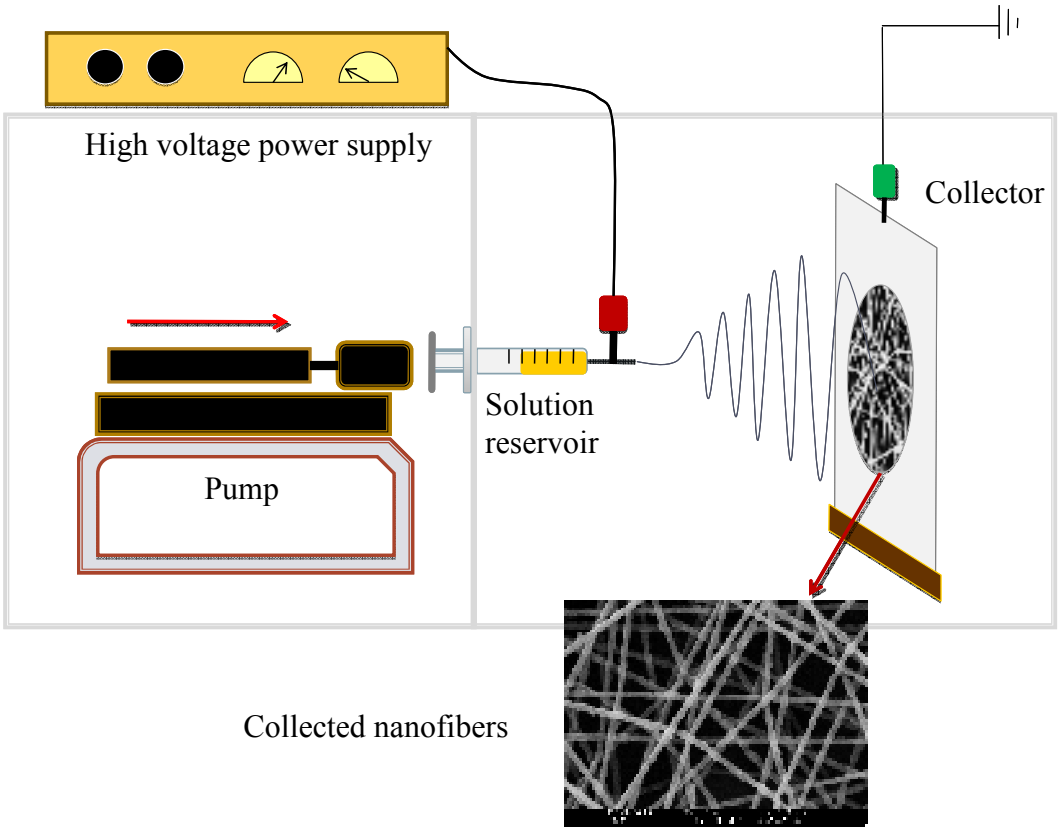

Figure 1. Schematic diagram of a laboratory electrospinning setup.

Under the effect of an applied electric field a drop of polymer solution emanates from the tip of the needle as a consequence of charge repulsion [15]. As the intensity of the electric field increases, so does the repulsion on the surface of the drop, altering its shape into a well known Taylor cone [16]. At a critical voltage, electrostatic forces overcome the surface tension of the polymer solution. This forces cause the ejection of a thin jet from the capillary nozzle. Once the solution is ejected, the charged viscoelastic jet is accelerated towards the counter electrode. During this period, the jet undergoes a series of instabilities, causing it to elongate and become thinner [17]. At the same time evaporation of the solvent takes place resulting in solid fibers being deposited on the grounded collector. These fibers can be obtained in the

form of a random mesh or as uniaxially aligned fibers, depending on the type of collector employed [18].

2.1.2 Parameters Influencing the Electrospinning Process

In order to obtain nanofibers with the desired properties for a given application an appropriate combination of solution and process parameters is critical. Processing variables such as flow rate, applied voltage and applied electric field play important roles in shaping the final characteristics of the fibers [12]. As for the solution, surface tension, conductivity and viscosity are essential for the formation of continuous fibers [5, 11, 19]. By manipulating these parameters, a variety of fiber structures, ranging from beads to smooth fibers, can be obtained.

2.1.2.1 Applied Electric Field

The series of instabilities that arise during the flight path of the jet are the result of the Coulombic interaction between the applied electric field and the free charges in solution [20]. Three different types of instabilities have been reported: the Rayleigh (axisymmetric) instability, the axisymmetric conductive instability and the whipping instability (shown in Figure 2) [21].

The Rayleigh instability is characterized by statistical fluctuations in the jet diameter. At low electric fields, the strong surface tension of the polymer solution tends to decrease the total energy of the system by changing the shape of the elongated jet into droplets. As one increases the strength of the electric field this type of instability is suppressed since the electric force is large enough to overcome the surface tension of the polymer solution [14]. However, a second instability arises with increasing electric field. This instability is known as the axisymmetric instability and results from a statistical modulation of the jet diameter which induces a movement on the surface charge density. The axisymmetric instability happens due to the fluids

finite conductivity and is enhanced as the intensity of the field is increased where charge mobility increases as well [22, 23].

Of utmost importance is the whipping instability which takes place at high electric fields. This instability has been identified as the one in charge of elongating and thinning the electrospun jet [21]. At first it was thought that the reduction in the jet diameter was a consequence of *splaying*: the splitting of the primary jet into multiple filaments due to radial repulsion within the jet [24]. When using a high speed camera, what appeared as an inverted cone representing the splaying of the jet turned out to be a single, rapidly whipping jet [20, 25]. This instability can occur through either: i) small lateral fluctuations in the centerline of the jet, resulting in the induction of a dipole charge distribution. These dipoles will interact with the external field, causing a torque which further bends the jet; and ii) mutual repulsion of surface charges causing the centerline to bend [25].

Reneker *et al.* [14, 20] were able to describe the flight path of the jet. They observed how the growing perturbed path of the jet bent into a three-dimensional coil, which was carried downstream and decreased in diameter as both the elongation and bending continued. Besides this first bending instability they were able to distinguish higher order instabilities as the jet traveled to the collector. Figure 2 shows a diagram of the whipping jet and the onset of the instabilities.

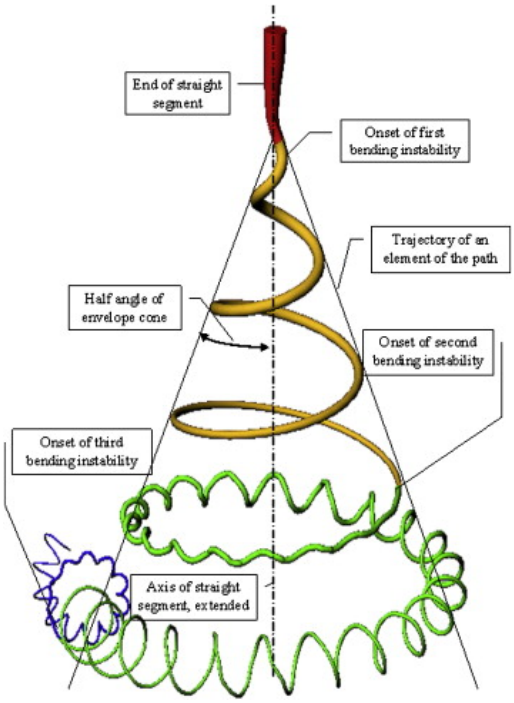

Figure 2. Diagram showing the instantaneous position of the path of an electrospinning jet containing three successive electrical bending instabilities[14].

In order to understand the effect of the different modes of instability several mathematical models have been developed. Reneker *et al.* [20] created a nonlinear model, with small and large perturbations, to describe the bending instability in a system of connected viscoelastic dumbbells employing the Maxwell viscoelastic model. Shin *et al.* [25] developed a linear stability analysis in a small capillary and performed bending perturbations on the viscous Newtonian jets. Yarin *et al.* [26] formulated a electrohydrodynamical theory for the electrospinning jet which provided a basis for the development of a computational model that successfully described the path of the jet including the high order bending instabilities. Thompson *et al.* [27] varied solution and operating parameters in a previously developed theoretical model in order to comprehend their effect on the resulting fiber diameter. A strong linear increase in fiber diameter was obtained with increasing polymer concentration in solution. The effect of viscosity values were not reported in this study. By gaining a better

understanding of the instability modes and the effect that they have on the resulting fibers, a better control of the electrospinning process can be achieved.

2.1.2.2 Applied Voltage

After a voltage has been applied between the capillary and the grounded collector, a drop of solution emerges at the end of the capillary forming a well known Taylor cone [16]. As soon as the applied voltage exceeds a critical value, a jet will emanate from the vertex of the cone. Following the jet initiation, the shape of the cone cannot be maintained if the flow of solution to the capillary does not match the rate of removal. When the rate of removal exceeds the flow of solution the cone collapses into an originating surface [28].

While electrospinning poly(ethylene oxide) (PEO), Deitzel *et al.* [28] observed a change in the morphology of the electrospun fibers from straight, defect-free fibers to high defect density fibers as the applied voltage increased. They noticed a relationship between the change in fiber morphology and the change in the morphology of the originating jet (either a well established cone or an originating surface). As the equilibrium voltage is exceeded, the rate of solution removal is greater than the rate at which the solution is supplied to the capillary. The consequence of this inequality is the collapse of the conical surface leading to an unstable jet. Similar results were reported by Andrews *et al.* [29] for low viscosity solutions, but no explanation was given. Figure 3 shows a set of SEM images of the fibers obtained by Andrews. The effect of increasing the applied voltage on the morphology of the resulting fibers can be seen.

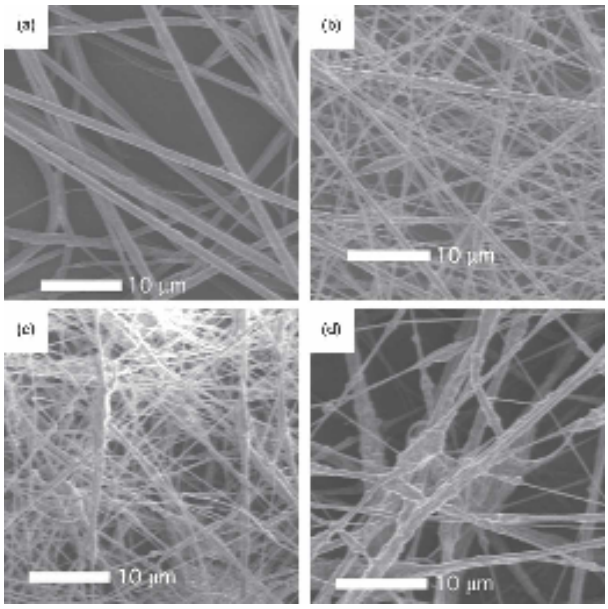

Figure 3. SEM images of Polyvinylidene difluoride–$NiZnFe_2O_4$ fibers spun at (a) 7 kV, (b) 10 kV, (c) 15 kV, and (d) 20 kV[26].

Opposed to the results reported by Deitzel *et al.*, Zuo and coworkers [30] found that increasing the applied voltage tends to suppress the formation of beads when electrospinning poly(hydroxybutirate-co-valerate). They related these results to the higher drawing stress due to an increased electric field, favored by the whipping instability.

Ojha *et al.* [12] studied the effect of the applied voltage on the electrospinning of Nylon-6. They were able to determine an optimum voltage for each molecular weight which maximized the whipping instability. Their results showed how an increase in the applied voltage will slightly increase the resulting fiber diameter. This behavior was attributed to the fact that more solution was ejected from the tip of the capillary as the electrostatic force increased. No defects in the resulting fibers as the voltage increased were reported.

2.1.2.3 Flow Rate

As one increases the flow rate more polymer solution is available at the end of the capillary to be ejected. A balance between the rate of removal and the feeding rate must be reached in order to obtain a stable Taylor cone. If the flow rate is increased to a point where it may exceed the rate of removal at a fixed electric field, non uniform drawing and beaded nanofibers are obtained. Further raising the flow rate will increase the bead size and density [12, 29, 30]. Wang *et al.* [31] studied the impact of the Taylor cone shape on the resulting fibers for a given flow rate and voltage. They found the solution's rheological properties more important than the shape of the Taylor cone when it comes to the formation of smooth fibers.

2.1.2.4 Rheological Properties of the Precursor Solution

Solution viscosity is considered as one of the most influential parameters for the formation of smooth, defect-free fibers during electrospinning [32]. Viscosity is a function of concentration and molecular weight, which has been established through empirical relations such as the Huggins equation for solution viscosity (1) and the Mark-Houwink-Sakurada for intrinsic viscosity (2) [33]:

$$\eta_{sp}(c) = [\eta]c + k_H([\eta]c)^2 + \cdots \qquad (1)$$

$$[\eta] = KM^a \qquad (2)$$

Empirical relationships between viscosity and resulting fiber diameter have been reported. Gupta *et al.* [5], while working with low molecular weights, found that the final diameter of PMMA fibers scaled with viscosity to the 0.72 power. A similar result was obtained by McKee *et al.* [34] in a study involving linear and branched polymers, from which a universal relationship was derived.

Several studies have been aimed at determining the relationship between solution concentration and the morphology of the resulting fibers. Four different concentration regimes have been reported: dilute, semidilute unentangled, semidilute entangled and

concentrated [34]. For fiber formation to occur, a minimum concentration, which corresponds to the boundary between dilute and semidilute unentangled regime, is required. This state is known as the critical entanglement concentration, c*, and can be approximated by $c^* \sim 1/[\eta]$ [5]. As one surpasses this threshold molecular chains start to overlap, forming beads with incipient fibers. A further increase in concentration results in the formation of chain entanglements [35]. Figure 4 illustrates the different concentration regimes in polymer solutions.

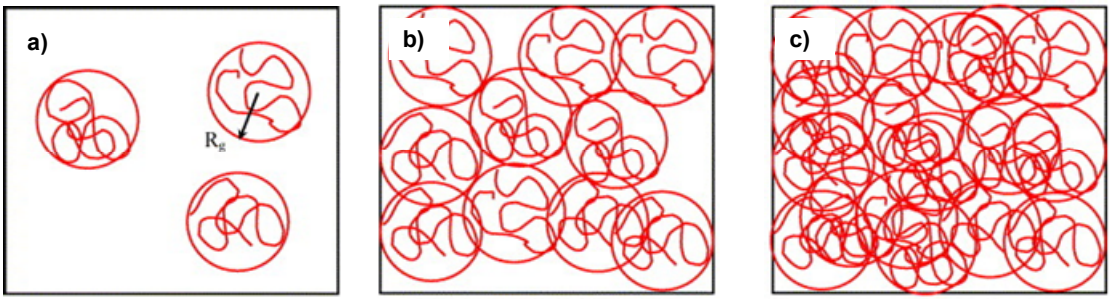

Figure 4. Physical representation of three solution regimes, (a) dilute, (b) semidilute unentangled and (c) semidilute entangled[5].

Chain entanglements consist of physical interlockings of polymer chains, which are a requirement for the formation of smooth, defect-free fibers [31]. These entanglements behave in a similar manner as chemical cross links, with the ability of chains to slide past another [35]. Wang *et al.* [31], while working with polystyrene (PS), obtained smooth fibers at concentrations ranging from 1.8 c* - 2.5 c*. Similar results were obtained by McKee and coworkers [34] while electrospinning linear poly(ethylene terephthalate – *co* – ethylene isophthalate). For the production of smooth fibers, a concentration range of 2c* - 2.5c* was reported. Finally, a further increase in concentration has been reported to increase the final diameter of the fiber [11, 36, 37].

Besides concentration, molecular weight and molecular weight distribution (MWD) play an important role in electrospinning. An increase in molecular weight of the

polymer at a fixed concentration will result in the formation of smooth fibers. From polymer chain statistics, the radius of gyration R_g of a polymer molecule is given by:

$$R_g = {}^{1}/_{6}\sqrt{x}a \qquad (3)$$

Where a is the average length of a polymer repeat unit and x corresponds to the degree of polymerization of the polymer [33]. It can be seen from Equation 3 how increasing molecular weight will increase the radius of gyration (illustrated in Figure 3-a) of the molecule. This increase will raise the amount of chain overlapping and in turn the number of chain entanglements [5, 35].

The effect of molecular weight distribution has also been studied. Using a polymer with a broad MWD results in the formation of beads, compared to smooth fibers produced with a narrow MWD. When using a narrow MWD, there is a narrow distribution of hydrodynamic volumes. A broad MWD comes with a broad distribution of these hydrodynamic volumes. Small chains act as weak links by reducing the entanglement density. These links cause the premature breakage of the jet, resulting in beads as the final product [5]. Similar results have been reported elsewhere [12].

2.1.2.5 Surface Tension

As the jet elongates, surface tension tends to inhibit the rapid increase in superficial area by changing the jet morphology into spheres. This effect is more prominent at low viscosities for which a decrease in its value is needed to produce continuous filaments [19, 32]. Yang *et al.*[19] electrospun poly(vinyl pyrrolidone) (PVP) from a variety of solvents with different surface tension values. The system with the lowest surface tension was able to produce smooth fibers, contrary to beads or beaded fibers produced by solutions with higher surface tension.

Fong and coworkers [32] studied the electrospinning of PEO while varying several parameters such as polymer concentration, cosolvent ratio (ethanol/water) and

salt (NaCl) concentration. While doing this the surface tension of each system was being monitored. Figure 5 shows the effect of changing the cosolvent ratio on the resulting fibers. Increasing the ethanol concentration made the solution's viscosity higher and its surface tension lower. This behavior led to the formation of smooth fibers. Similar results have been reported by Zuo *et al.* [30] during the electrospinning of poly (hydroxy butyrate/valerate) (PHBV).

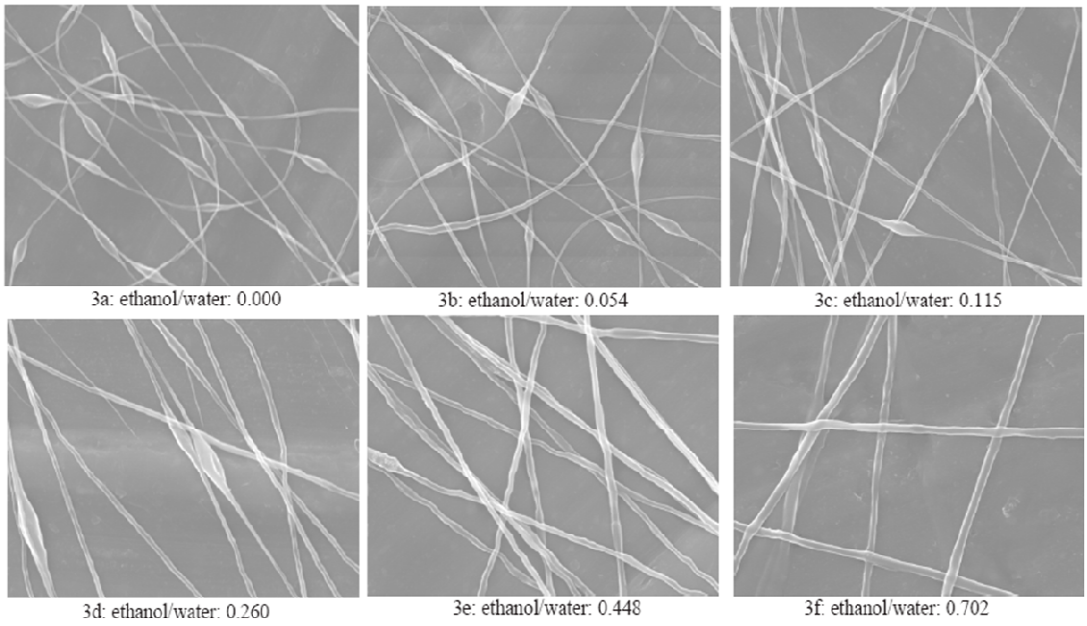

Figure 5. Variation of beaded fibers as the mass ratio of water/ethanol is changed. Electric field is 0.5 kV/cm, weight fraction of PEO is 3.0%. The horizontal edge of each of the figures is 20 microns long[32].

2.1.2.6 Conductivity

It has been reported that increasing the conductivity of a polymer solution will favor the production of smooth, small diameter fibers [30, 38]. As the jet forms and the solvent evaporates the charge density increases. This increase will results in charge repulsion within the jet and the development of the whipping instability [39].

For non conductive polymer solutions the addition of salt has proven effective to increase conductivity. You *et al.* [19] investigated the effect of the addition of NaCl during the electrospinning of poly(D,L-lactic-*co*-glycolic acid) (PLGA) solution. As expected, by adding 2% of salt to the polymer solution the conductivity raised drastically. This increase decreased the final fiber diameter from 760 to 490 nm. Furthermore, the addition of superparamagnetic nanoparticles into the polymer solution has also been reported as a mean of increasing the solution conductivity. When adding 7.5% of ferrite oxide particles into a PEO solution, smooth fibers were obtained [38] .

2.1.3 A Review of Electrospun Polymer Systems

A broad range of polymers have successfully been electrospun in the past years. Polymers can be electrospun from solution or from the melt, being electrospinning from solution the most studied. Ogata *et al.* [40] developed a melt-electrospinning equipment in which a CO_2 laser was used as the melting device. They were able to electrospun polyethylene terephthalate (PET), polyarilate (PAR) and poly-lactide (PL) successfully, although their resulting fibers were in the order of microns. Employing a shielded heating unit has also been employed as a heating device for electrospinning polypropylene (PP) [41].

One of the advantages of solution electrospinning is the ability of using water as a solvent. Water soluble polymers such as PEO [9, 17, 25] and poly(vinylalcohol) (PVA) have been successfully electrospunn with no risks of solvent toxicity [42]. Polymers such as PS [43-45], PMMA [5], polyamides [46, 47] and PAN [48], have been successfully electrospunn from a wide variety of solvents. Moreover, volatile solvents, such as THF [43-45] or HFP[19, 49], as well as solvent mixtures[9, 11, 50] have been employed in order to study several properties such as bead formation, solvent-polymer interaction and surface morphology of the resulting fibers.

Recently, research efforts have focused in developing nanofibers from biodegradable polymers. These fibers show outstanding properties such as biodegradability, biocompatibility, good mechanical properties as well as FDA approval for medical devices. As a result, they can be used in a wide variety of applications such as surgical sutures, implant materials, drug carriers as well as cell growth scaffolds for tissue engineering [19]. Some polymers that have been electrospun for these purposes include PLGA [19], PLLA [37, 51], PDLLA [11], PCL[52], and collagen[49].

2.1.4 Electrospinning of Composite Nanofibers

Composite materials are a mean to achieve properties otherwise not present in their individual components. Two types have been described: series and product composites. The former are composites which properties are a weighted average of their constituent phases, whereas the latter show unique properties which result of the coupling between phases [29].

Polymers have been considered as excellent host matrices for composite materials due to their attractive properties such as non corrosiveness, light weight and mechanical strength. By using a composite approach several properties of polymer fibers, such as gas barrier and mechanical strength, can be enhanced. For instance, montmorillonite (MMT) has been used for polymer composites since its high aspect ratio and available layer surface area enhance mechanical properties, thermal stability, flame retardancy, and gas-barrier property of the polymer host [53]. As an example, successful electrospinning of Polyurethane/MMT composites has been achieved [54].

The inclusion of ferromagnetic or superparamagnetic nanoparticles in a polymer matrix presents potential applications since they exhibit interesting magnetic field-dependent mechanical behavior [38]. These materials can be used as ultrahigh density data storage applications [1], magnetic filters [2], biomedical[33] and anti counterfeiting applications [4], among others.

Below a diameter of approximately 100nm, these magnetic particles don't exhibit the cooperative phenomenon of ferromagnetism found in the bulk, since thermal energy at room temperature is sufficient enough to reorient the magnetic moment within their domains. As a result these particles behave as superparamagnetic, in that there is zero remnant magnetization at zero applied external field [3, 38]. When incorporated into polymeric nanofibers, superparamagnetic materials can be produced. As an example, Figure 6 shows a TEM image of PEO/magnetite fibers obtained during this work.

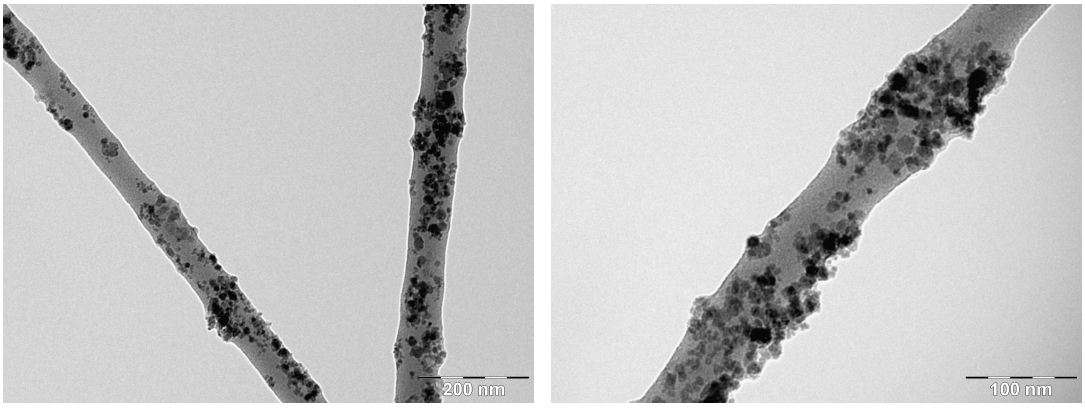

Figure 6. TEM images of 1vol% PEO/magnetite nanofibers.

Electrospinning of these polymer-nanoparticles systems has been achieved with good results. In order to obtain a homogeneous dispersion, the particles are usually functionalized with a surfactant compatible with the polymer matrix [29]. Gupta *et al.* [2] electrospun a solution of elastomeric polyurethane with ferrite (MnZnFe-Ni) nanoparticles of approximately 14nm in diameter. The resulting nanofibers retained the superparamagnetic properties of the particles. Figure 7 shows the magnetization curves obtained from the resulting fibers at different particle concentration. As concentration increased, so did the saturation magnetization. The superparamagnetic behavior is evident from the little hysteresis in the fibers, as shown in the inset of the figure.

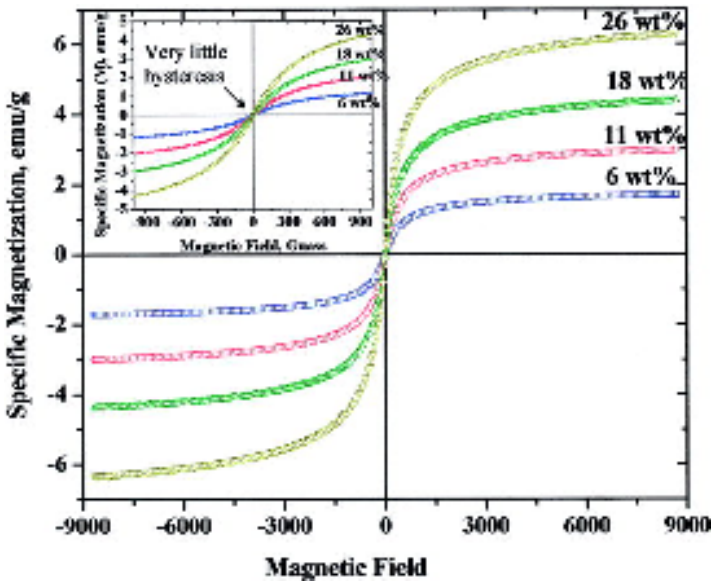

Figure 7. Specific magnetic saturation vs. magnetic field of polyurethane/ferrite composites at different nanoparticles concentrations[2].

Wang *et al.* [38] produced PEO and PVA composite nanofibers with Fe_3O_4 (magnetite) particles via electrospinning. Their results showed a column-type alignment of the particles within the fibers probably due to the hydrodynamic in the capillary or induction by the local electric field. Under the application of an external magnetic field, these particles are expected to align their magnetic moments with it, resulting in a deflection of the nonwoven mat, as shown in Figure 8.

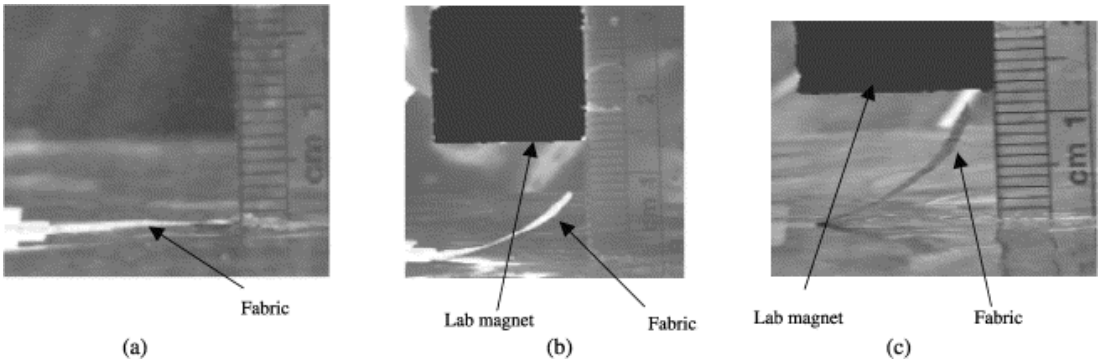

Figure 8. Field responsive behavior of PVA/magnetite fabric: (a) without magnetic field, (b) within low gradient of magnetic field, (c) within high gradient of magnetic field[38].

Besides producing superparamagnetic flexible substrates, electrospinning of polymer-magnetic nanofibers has proven useful for other purposes. Tan *et al.* [37] electrospun a solution of 5% PHEMA containing 5 wt% Fe_3O_4 and 1% albumin in order to develop magnetic drug delivery systems with the possibility of using external magnetic fields to guide the drug carrier to precise target areas. Research has also focused in the creation of metallic nanofibers by electrospinning a saturated solution of polymer with metallic or magnetic nanoparticles and subsequently calcinating the polymer matrix. This technique has allowed the production of Fe, Co, Ni, cobalt ferrite ($CoFe_2O_4$) and nickel ferrite ($NiFe_2O_4$) nanofibers, among others [1, 55-57].

2.1.5 Characterization of Nanofibers and Composite Nanofibers

In order to study the physical and chemical properties of nanofibers and their composites, a wide variety of techniques can be used. *Scanning Electron Microscopy* (SEM) is usually employed for measuring parameters such as fiber diameter, morphology and orientation [25, 29, 32]. When higher resolution is needed, as to observe surface roughness or porosity, *Field Emission Scanning Electron Microscopy* (FESEM) has proven useful [5, 34, 58]. Megelsky *et a.l* [43] studied the morphology, size, and distribution of pores on the surface of electrospunn nanofibers by means of FESEM. Figure 9 shows some of their results.

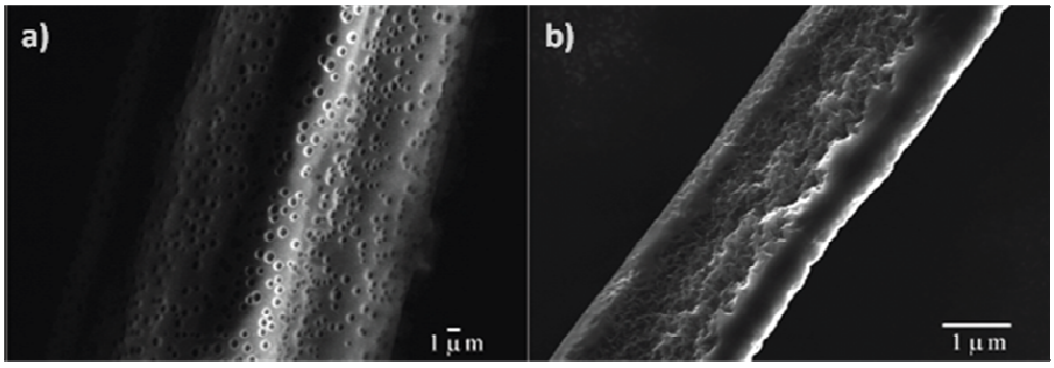

Figure 9. FESEM images of a) polystyrene and b) polycarbonate nanofibers produced by electrospinning [43].

Transmission Electron Microscopy (TEM) is employed to study the interior structure of the nanofibers [38, 53, 59]. For fillers consisting of metallic or magnetic particles this technique allows one to assess their good dispersion, as well as the particle core size and size distribution [60]. Orientation of fillers such as carbon nanotubes and montmorillonite layers has also been studied using TEM. The last is an extremely important factor since the enhancement of mechanical properties is direction dependent; hence the filler must be oriented along the fiber long axis to obtain good results [53, 59].

Other equipments are available in order to study properties like molecular crystallization, mechanical strength and fiber composition. Lu *et al.* [60] used *Fourier Transform Infrared Spectroscopy* (FTIR) to determine the existence of a chemical interaction between the polymer matrix and the filler, by looking at the change in the characteristic C=O peak intensity. FTIR has also been employed to study molecular conformation within the fibers. With a polarized FTIR, Kakade and coworkers [61] were able to study the molecular alignment parallel to the macroscopic orientation of the fiber. The fibers were uniaxially aligned employing countercharged aluminum plates as collectors.

The effect of electrospinning on the molecular crystallization within the fiber has also been studied. Shao *et al.* [62] studied the effect of silica concentration in the crystallization of PVA/SiO2 composite fibers using *X-Ray Diffraction* (XRD). Pure PVA fibers tend to crystallize due to the hydroxyl groups in the side chain. The addition of silica disrupts this interaction, decreasing the fiber crystallinity as concentration is increased. Crystallization studies of different polymer such as poly(ε-caprolactam) and aligned PEO, as well as metallic nanofibers produced by electrospinning, have also been performed using XRD [61, 63, 64]. *Differential Scanning Calorimetry* (DSC) can sometimes be employed to support XRD results.

In addition, mechanical properties of nanofibers are important in determining the material functionality and its possible applications. Properties such as yield stress, tensile strength and mechanical modulus can be measured by employed a common Universal Testing Machine [63]. Guhados *et al.* [65] developed a technique to accurately measure the elastic modulus of nanofibers using *Atomic Force Microscopy* (AFM) by measuring the cantilever deflection across a suspended fiber. On the other hand, Wang *et al.* [38] employed the AFM indentation technique to analyze PEO filled with magnetite nanofibers. Their results showed an increase in mechanical properties due to the filler. Besides studying mechanical properties, AFM can also be employed to study the resulting fiber surface morphology [53].

2.2 Magnetic Nanoparticles

Ferrofluids are colloidal mixtures of nonmagnetic liquid carriers (usually oil or water) containing single domain magnetic particles in the order of 5-15nm with volume concentrations up to 10% [66]. Current applications include magnetic fluid rotary seals, sink float separation of minerals, magnetic clutch, and tunable dampers [67]. One of their most prominent uses is in the biomedical field, used in magnetic cell separations, targeted drug delivery and diagnostics [68]. Even though a great amount of

research has been done in this field, a more precise and reproducible control in their synthesis is important for these applications, since properties such as size and shape play an important role in determining their magnetic properties.

2.2.1 Magnetic Properties

2.2.1.1 Macroscopic Theory

To understand the basic concepts of magnetism, consider a long solenoid with vacuum as the medium inside [69]. One can create a magnetic field within the solenoid, denoted as $\mathbf{B}_o$, by passing an electric current. The relation between electric current (I) and the number of turns per unit lenght (n) to the generated field is given by:

$$\boldsymbol{B}_o = \mu_o nI \qquad (4)$$

where μ_o is the permeability of free space ($4\pi \times 10^{-7}$ Henries/m). If we place a solid inside the solenoid, a magnetic field (**B**) of different magnitude will be generated. This results from the response of the individual atoms to $\mathbf{B}_o$, acquiring an individual magnetic moment. Consequently, the medium becomes magnetized, with a magnetic vector (**M**) that describes the degree of magnetization. A diagram of a magnetized medium within a solenoid carrying a current is shown in Figure 10.

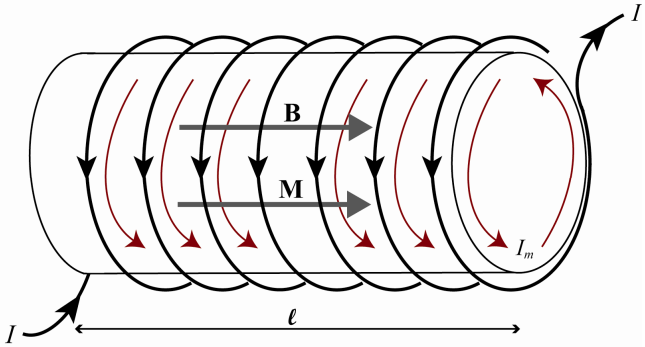

Figure 10. Schematic diagram showing how a material develops a magnetization M when inserted into a solenoid carrying a current. Adapted from (69).

M can be defined as the *magnetic dipole moment per unit volume*. The magnetic field **B** inside the solenoid can be expressed in terms of the magnetization vector by:

$$\boldsymbol{B} = \boldsymbol{B}_o + \mu_o \boldsymbol{M} \qquad (5)$$

The magnetizing field **H**, also known as magnetic field intensity, represents the contribution of external currents which magnetize the material. This field is defined as:

$$\boldsymbol{H} = (1/\mu_o)\, \boldsymbol{B}_o \qquad (6)$$

Two important parameters relate these three quantities: the magnetic susceptibility χ_m (7) and the relative permeability μ_r (8). The former relates the increase in the magnetic field, as compared with free space, when a new material is introduced. The later represents the degree of magnetization of a material in response to an applied magnetic field [69, 70].

$$\boldsymbol{M} = \chi_m \boldsymbol{H} \qquad (7)$$

$$\boldsymbol{B} = \mu_r \mu_o \boldsymbol{H} = \mu \boldsymbol{H} \qquad (8)$$

2.2.1.2 Magnetic Materials Classification

In magnetic materials, specific interactions between the spins of neighboring atoms lead to their magnetization. For the synthesis of magnetic nanoparticles, ferromagnetic or ferrimagnetic materials are usually employed. *Ferromagnetism* originates from the quantum mechanical exchange interaction between the constituent atoms. This results in the spontaneous alignment of the magnetic spins in one direction, creating a permanent magnetization vector in the absence of an external field [69].

Consider a system comprising two atoms. The exchange interaction can be represented in terms of exchange energy (E_{ex}) as:

$$E_{ex} = -2\, J_e\, S_1 \bullet S_2 \qquad (9)$$

where S_1 and S_2 are the spin angular momenta and J_e is the exchange integral. For the majority of solids, J_e has a negative value. In order to reduce the exchange energy, S_1

and S_2 align in opposite directions, cancelling each other and resulting in zero net magnetization. This is the case of *antiferromagnetism.*

Transition metals such as Fe, Co and Ni, have a positive J_e, therefore S_1 and S_2 must align in the same direction to obtain a negative E_{ex}. As shown in Figure 11, this spontaneous coupling result in the magnetization of the material, which correspond to the ferromagnetism phenomenon. These materials possess a large saturation magnetization (M_s) and magnetic susceptibility (χ_m). Above a given characteristic temperature, called the Curie temperature (T_c), ferromagnetism is lost and the material becomes paramagnetic.

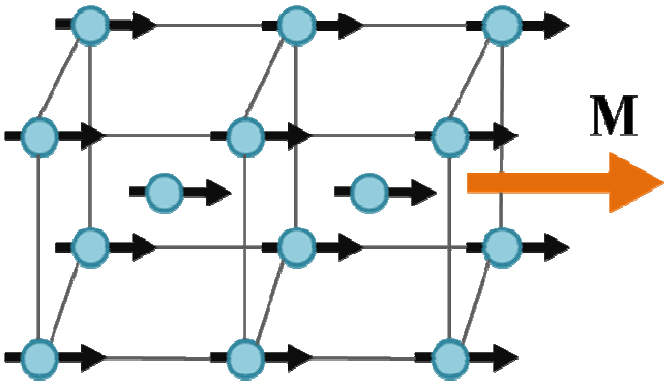

Figure 11. Magnetized region of a ferromagnetic material such as Fe. The magnetic moments are spontaneously aligned in the same direction. Adapted from (69).

Paramagnetic materials do not show the cooperative phenomenon seen in ferromagnetism. When applying a magnetic field, the magnetic moments of the constituent atoms will align in the same direction. As soon as the field is removed, the moments will randomize as a result of thermal fluctuations, resulting in zero magnetization of the material [71]. This compounds present very small magnetic susceptibilities (in the order of 10^{-5}) and are extremely affected by temperature [69].

Ferrimagnetism is usually exhibited in compound materials such as ferrites (Fe_3O_4 and γ-Fe_2O_3). In this case, the exchange interaction causes the different sets of magnetic moments to line up antiparallel to each other (See Figure 12). If the

magnetic moments are unequal in magnitude a net magnetization will result from this coupling. These materials behave as ferromagnetic materials with lower saturation magnetizations [70]. Table 1 lists several ferromagnetic of ferrimagnetic materials in ascending order of magnetization [72].

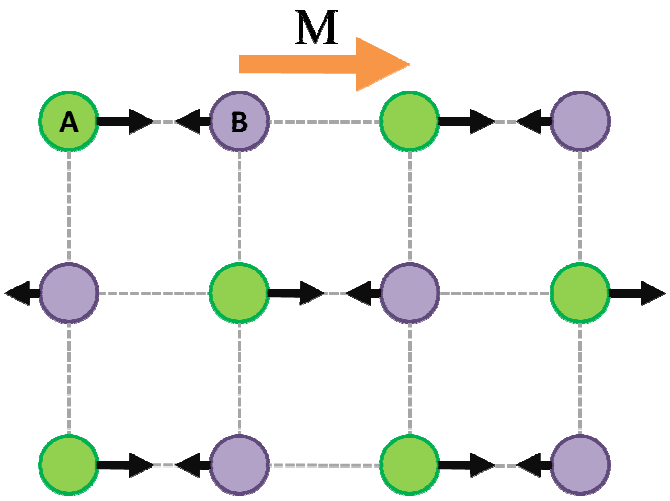

Figure 12. Schematic diagram showing the ordering of magnetic moments in a ferrimagnetic crystal. Since the magnetic moment of atom A is greater than that of atom B, there is a net magnetization M in the crystal represented by the orange arrow. Adapted from (69).

Table 1. Commonly employed ferromagnetic and ferrimagnetic materials [69].

Material	Type of magnetism	T_c (^{0}C)	M_s (A/m)
Chromium dioxide (CrO_2)	Ferrimagnetic	117	410
Maghemite (γ-Fe_2O_3)	Ferrimagnetic	590	414
Cobalt Ferrite ($CoFe_2O_4$)	Ferrimagnetic	520	422
Magnetite (Fe_3O_4)	Ferrimagnetic	585	470
Nickel (Ni)	Ferromagnetic	358	485
Cobalt (Co)	Ferromagnetic	1131	1400
Iron (Fe)	Ferromagnetic	770	1707

2.2.1.3 Magnetic Domains

Magnetic materials possess potential energy, known as magnetostatic energy (E_m), which is determined by the density of magnetic flux lines in free space. In accordance with the natural tendency to reduce energy, magnetic domains are created within the internal crystal structure. As shown in Figure 13, a reduction in the external magnetic field lines results from these internal magnetic domains. Within each domain, saturation magnetization is reached; however, neighboring domains tend to point in opposite directions, cancelling each other. This behavior results in a material with no permanent magnetization and occurs when a material is annealed without the presence of an external field [73].

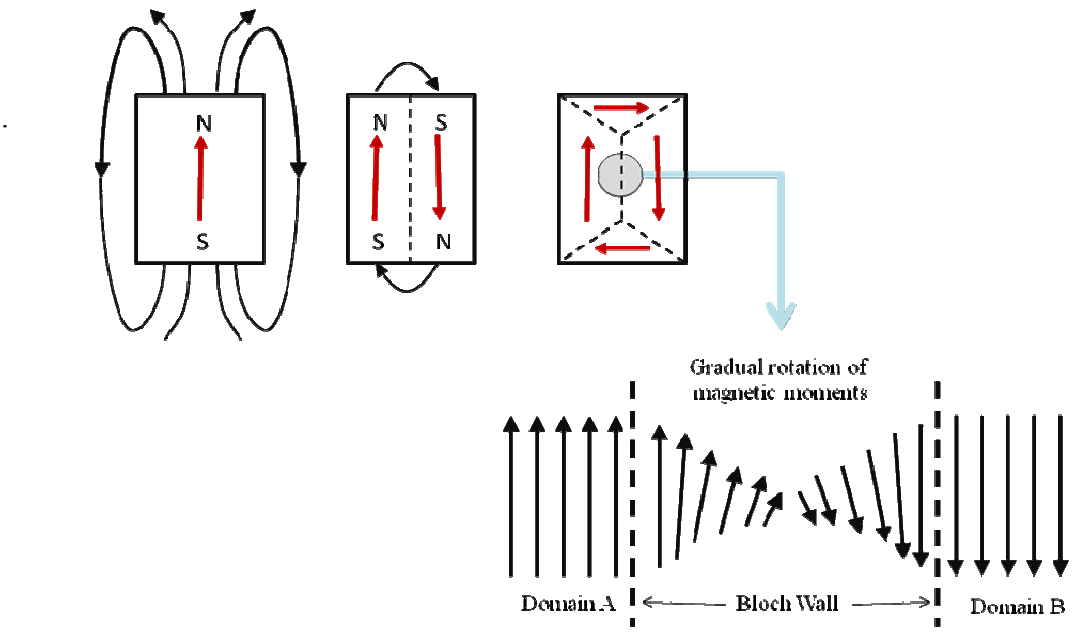

Figure 13. Formation of magnetic domains in a ferromagnetic material showing the moment transition within the Bloch wall. Adapted from (69).

The magnetization vector within each domain is oriented along a given crystallographic direction, called the *easy axis of magnetization,* making magnetic properties anisotropic. Between each two domains lies a boundary called *Bloch Wall*, were the orientation of the atomic spins change from one direction to the opposite

(180^o rotation). Rotating the magnetic vector from its easy axis of crystallization requires energy, known as *anisotropy energy* (E_a). This energy depends on the magnetocrystalline anisotropy constant (K) as well as the size of the material (E_a=KV) [72]. To employ the minimum amount of energy, the rotation of the magnetic vectors must be done gradually through a wall of finite thickness (in the order of 0.1μm for Fe) as shown in the magnified region of Figure 13. The domain formation goes further until the potential energy reduction in creating an additional domain equals the increase in creating an additional wall [69].

By slowly raising the temperature of a magnetized sample, thermal oscillations within the crystal become more vigorous. At a given point they will be strong enough to overcome the anisotropy energy, causing the magnetization vector to rotate around its easy axis. In the absence of an applied field, this tends to randomize the magnetic moments, progressively demagnetizing the sample. The temperature at which the onset of demagnetization occurs is called the *blocking temperature*, Tb. At an even higher temperature, denoted as the *Curie temperature* (Tc), the individual spins cease to align with each other, even when an external field is applied. At this point, the material behaves as paramagnetic [69]

2.2.1.4 Magnetization Curve

The magnetization curve describes the change in the magnetization or magnetic flux of a material with an applied field. In a polycrystalline sample each grain will possess a magnetic domain that depends on its size and shape. The magnetization of a single ferromagnetic crystal involves the motion of domain boundaries, allowing the domains oriented with the field to grow at expense of those that are not [73]. Figure 14 shows the magnetization curve for a ferromagnetic material.

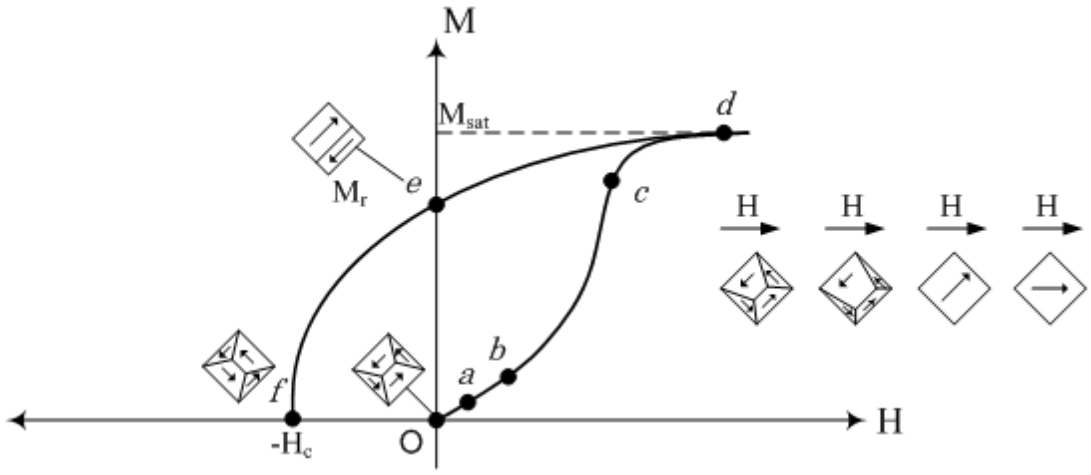

Figure 14. Magnetization curve of a previously unmagnetized polycrystalline specimen. Adapted from (69).

Starting from an unmagnetized material, when applying a small magnetic field along an arbitrary direction, the domain walls of favorably oriented domains begin to move. At this point (a), the domain motion is reversible. As one continues to increase the applied field the domains grow larger (b), until the material reaches a point were nearly all the grains are single domains with saturation magnetization in the same direction as the field (c). At a given field, the magnetization value becomes constant, indicating that all the single domain grains have rotated to align with the field. This point is known as *saturation magnetization*, M_s, and is the highest value that magnetic materials can exhibit.

When decreasing the field the moment in each grain will rotate to align antiparallel, developing smaller domains in some grains. This process leaves the specimen with a finite magnetization at zero field, characteristic of ferromagnets, called *remanent or residual magnetization*, M_r (e). As contrast, paramagnetic materials do not exhibit residual magnetization.

By reversing the direction of the applied field, eventually the material will be demagnetized at a given field intensity (f). This is called the *coercivity* or coercive field (H_c), and represents the resistance of the sample to demagnetization. By

continuing to increase the field in the *–x* direction, a process similar to the one described above occurs. In the end, this will lead to a closed loop, called *hysteresis loop*, which represents the full M versus H behavior of the material.

Materials can be classified as soft or hard magnets from M versus H behavior. Soft magnetic materials are easy to magnetize or demagnetize, showing a narrow hysteresis loop. On the other hand, hard magnets require large magnetic field intensities in order to magnetize or demagnetize them, showing an almost rectangular hysteresis curve [69, 7071].

2.2.1.5 Magnetic Properties of Nanoparticles

When the size of a ferromagnetic material is reduced below a critical size the creation of magnetic domains is no longer energetically favorable, resulting in magnetic particles with single domains. This critical size fluctuates around 15nm and is dependent on several factors such as shape, anisotropy energy and saturation magnetization [74].

The coercivity of fine particles is size dependent. As the particle size is reduced, the coercivity increases until it reaches a maximum, further decreasing towards zero. At this point, were H_c=0, the thermal energy of the surrounding medium overcomes the anisotropy energy of the material, causing the magnetic moments to fluctuate around the easy axis with a characteristic relaxation time. These particles behave as paramagnetic, with their magnetization values varying usually in the ferromagnetic range. This regime is known as *superparamagnetism*. For a given particle size, the blocking temperature marks the onset of the ferromagnetic-superparamagnetic transition [71].

The shape of the magnetization curve of a diluted assembly of superparamagnetic particles is well described by the Langevin equation [75]:

$$\frac{M}{\phi M_d} = coth(\alpha) - \frac{1}{\alpha} \equiv L(\alpha) \qquad (10)$$

$$\alpha = \frac{\pi}{6}\frac{\mu_0 M_d H d^3}{kT} \qquad (11)$$

Where φ is the volume fraction of the magnetic cores, M_d the domain magnetization, μ_o the magnetic permeability of free space, d the diameter of the magnetic core, k is Boltzman constant and T is the absolute temperature. For small applied fields, which corresponds to the initial slope of the hysteresis curve, a Taylor expansion shows that

$$L(\alpha) = \frac{\alpha}{3} \quad (12) \qquad \text{therefore} \quad \boldsymbol{M}=\chi_i \boldsymbol{H} \qquad (13)$$

χ_ι is defined as the initial susceptibility of the suspension, given by

$$\chi_i = \frac{\pi}{18}\phi\mu_0\frac{M_d^2 d^3}{kT} \qquad (14)$$

At high magnetic fields, when the sample is approaching saturation, Equation 10 has the limit

$$M = \phi M_d\left(1 - \frac{6}{\pi}\frac{kT}{\mu_0 M_d H d^3}\right) \qquad (15)$$

Typical nanoparticle synthesis methods usually yield polydisperse samples. Because of this, it is necessary to distinguish the diameters that appear in Equation 14 and 15. At low fields Brownian motion dominates the behavior of magnetic particles; hence the larger particles contribute primarily in Equation 14. At higher fields the larger particles have reached saturation and the small nanoparticles are the ones that contribute primarily in Equation 15. This approach allows one to set the upper and lower limit of the particle size distribution [4].

2.2.2 Synthesis of Magnetic Nanoparticles

According to the chemical nature of the particles their synthesis will be different. Some of the most representative magnetic materials are metal oxides such as ferrites. However, these are often obtained as mixtures of several oxides, which imply that their magnetic properties are not always well defined and reproducible [76]. Magnetic metals such as Ni, Fe and Co have higher specific magnetization than oxides,

but are highly unstable and tend to oxidize under air, losing their magnetic properties [77]. For colloidal applications, like commercial ferrofluids, the most commonly used materials are iron oxides, such as magnetite (Fe_3O_4) and maghemite (γ-Fe_2O_3) [72].

2.2.2.1 Magnetite and Maghemite Nanoparticles

2.2.2.1.1 Wet Grinding

Wet grinding was the original method for producing magnetite-based ferrofluids [77]. It involved wet-grinding magnetite grains in a ball mill in the presence of a surfactant and a liquid carrier. Usually, one starts with micron-sized particles and carries on until the particles reach a colloidal state. It takes from 500 to 100 hours to obtain particles around 10nm [66]. The surfactant helps with the grinding process by avoiding particle agglomeration [72, 77].

2.2.2.1.2 Co-Precipitation Method

The co-precipitation method for the production of magnetite and maghemite has been the subject for many publications. It is an extremely versatile method capable of producing magnetic particles ranging from 3 to 20 nm [77]. This technique can be approached by two ways: the first consists on the co-precipitation of a partly oxidized Fe^{2+} to Fe^{3+} by means of an oxidizing solution. The second approach consists in the direct co-precipitation of Fe^{2+} and Fe^{3+} in an alkaline media [78].

Although a simple method, particle size and size distribution are roughly controlled. In order to obtain reproducible results, process variables such as nature of alkali and concentration, concentration of ferric and ferrous salts, Fe(II)/Fe(III) ratio, ionic strength and temperature must be kept constant [72]. The overall chemical reaction for the precipitation of magnetite is given by [66]:

$$2Fe^{3+} + Fe^{2+} + 8OH^- \longleftrightarrow Fe_3O_4 + 4H_2O \qquad (16)$$

For this synthesis, a molar ratio of Fe^{2+} : Fe^{3+} = 1 : 2 is usually employed. This stoichiometry has proven to form magnetite particles homogeneous in size and

chemical composition, when keeping all other parameters constant [79]. Jiang *et al.* [80] improved the co-precipitation procedure using NH_4OH as well as urea to manipulate the pH of the resulting ferrite solution. This procedure produced a narrow particle size distribution with a tunable average diameter of 8 to 50 nm. Kim *et al.* [79] flowed N_2 gas to avoid magnetite critical oxidation, avoiding secondary reactions and allowing its complete precipitation. Vayssieres and coworkers [81] demonstrated a strong dependence of the average particle size with the acidity and ionic strength of the medium.

Magnetite can be oxidized very easily. Kept under usual atmosphere it quickly oxidizes into bertholite. This material is a ferric oxide which composition is between that of magnetite (Fe_3O_4) and maghemite (γ-Fe_2O_3). In order to produce maghemite, magnetite is deliberately oxidized by dispersing the magnetite particles in acidic medium and stirring them with ferric nitrate. The resulting particles are chemically stable in acidic or alkaline medium. Although maghemite has a lower saturation magnetization than magnetite, it is preferred over the later for some applications due to its chemical stability [72]. Bee *et al.* [82] reported the synthesis of maghemite via co-precipitation of Fe^{2+} and Fe^{3+} under alkaline medium in the presence of citrate ions. The final particle size of maghemite decreased from 8 to 2nm in the presence of citrate. This has been attributed to citrate ions inhibiting the nuclei growth.

2.2.2.1.3 Microemulsion Technique

As a way to control particle uniformity, average size, and size distribution, the microemulsion technique has been developed [83]. These micelles consist of thermodynamically stable isotropic dispersions of two relatively immiscible (i.e. water-in-oil) liquids stabilized by a surfactant, which have been successfully employed as nanoreactors for the synthesis of magnetic nanoparticles [84]. Due to the dynamic

nature of the micelles aqueous components gather and react to form particles constrained to the size of the micelle [83].

The method requires the preparation of two different microemulsions. The first consists of an aqueous solution of a metal salt or a mixture of metal salts such as Cobalt and Ferric nitrate. The second contains a precipitating agent. When mixing these two solutions in the appropriate ratio both reactants come in contact, resulting in the formation of a precipitate consisting of metallic nanoparticles [77, 84]. The size and distribution of micelles depend on the water/surfactant molar ratio in the system [85]. Sometimes a co-surfactant is employed to stabilize the micelles within the solution [86].

Lee *et al.*[87] reported a large scale synthesis of uniform and highly crystalline magnetite nanoparticles. It was reported that the particle size could be controlled from 2 nm to 10 nm by varying the relative concentrations of the iron salts, surfactant, and solvent.

2.2.2.2 Other Ferric Oxides

Ferrite oxides with a spinel-like structure (MFe_2O_4, M=Co, Mn, etc.) can be obtained in the form of nanoparticles with the methods already presented. The method of co-precipitation of the particles is essentially the same as described above, except that in some cases, the precipitate must be hydrothermally aged in order to facilitate the formation of the ferrites [77]. M can also represent a mixture of two components such as Zn and Mn, Ni or Co, resulting in $M_{1-x}\ Zn_xFe_2O_4$. Magnetic properties of these compounds are largely dependent on x, making its control one of the main difficulties during the synthesis of these compounds [72].

Cobalt ferrite ($CoFe_2O_4$) is an interesting material due to its high magnetocrystalline anisotropy, high coercivity and moderate saturation magnetization [88]. Several forms of synthesizing $CoFe_2O_4$ nanoparticles have been reported. Kim *et al.* [88] studied the effect of temperature during the synthesis of cobalt ferrite through the

co-precipitation method. They reported an increase in the particle size with temperature as well as a transition between 40 and 60^{o}C. Particles prepared below 40^{o}C behaved superparamagnetic whereas particles prepared above 60^{o}C comprised a mixture of superparamagnetic and ferromagnetic components, reducing the superparamagnetic fraction as temperature increased. Wang *et al.* [89]} found that the reactant mixing procedure and Fe^{2+}/Fe^{3+} ratio of initial solution were critical in the size, magnetic properties and shape uniformity of $CoFe_2O_4$ synthesized through the co-precipitation method.

A novel hydrothermal treatment of an aqueous solution consisting of cobalt dodecyl sulfate ($Co(DS)_2$), $FeCl_3$ and NaOH at 120^{o}C was developed for the production of cobalt ferrite particles [90]. The resulting particles were polydisperse in size ranging from 2 to 8nm. This method may also be useful for the synthesis of $NiFe_2O_4$ and $ZnFe_2O_4$. Figure 15 shows a TEM micrograph of the resulting $CoFe_2O_4$ particles after 4 hours of hydrothermal treatment. The variability in sizes and shapes is evident.

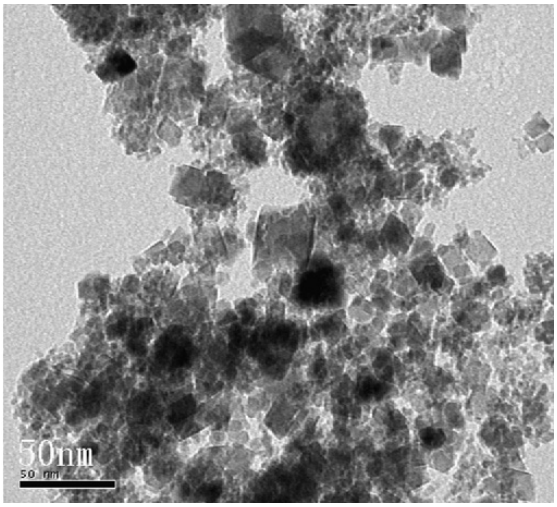

Figure 15. TEM of $CoFe_2O_4$ nanocrystals obtained via hydrothermal treatment of Co(DS)2, $FeCl_3$, and NaOH solutions at 120 ◦C for 4 hours[90].

Water-in-oil microemulsions have also been widely employed for the synthesis of particles such as $MnFe_2O_3$, $CoFe_2O_3$ [85], FeNi [91, 92], $CoFe_2O_4$ [84] and $CoZnFe_2O_4$ [93], to mention a few.

2.2.2.3 Metal Nanoparticles

Some of the mayor advantages of using metal nanoparticles over oxides are their high magnetic saturation and the easiness of production with a narrow size distribution. Iron is one of the most attractive materials since it has the largest saturation magnetization at room temperature as well as low magnetocrystalline anisotropy, making it the ideal soft magnet for commercial applications [94]. Metals such as iron, cobalt, and niquel are unstable by nature. Only by keeping them under an inert atmosphere, or coating them with a surfactant, they can have an extended lifespan [95].

2.2.2.3.1 Decomposition of Metallic Compounds

Thermal decomposition of metal carbonyl compounds is a convenient method that generates large amounts of small, uniform and monodisperse nanoparticles with small amounts of byproducts [94]. However, it is an uneconomical process because elevated temperatures and expensive, highly toxic precursors are needed [96]. Usually, iron particles are obtained by the thermal decomposition, at around 200^{o}C, of iron pentacarbonyl ($Fe(CO)_5$) in the presence of a stabilizer such as oleic acid or poly(isobutene) (PIB) [97]. The purpose of employing a surfactant is to control particle size, prevent particle agglomeration and protect them against oxidation [72]. By varying the Fe/PIB ratio, Butter *et al.* [97] were able to control the final diameter of the particles.

As an alternative to high temperatures synthesis sonochemical decomposition has been employed. Its mechanism relies on the acoustic cavitation phenomenon were transient localized spots of approximately 5000K are generated within an ultrasonically irradiated liquid. These spots act as micro reactors were decomposition

reaction takes place [98]. Iron [99] and nickel [100] nanoparticles have been synthesized using this technique.

Another form of obtaining metallic particles is by means of decomposing organometallic precursors. Nickel nanoparticles have been produced by the spontaneous decomposition of bis(cyclooctadiene)nickel ($Ni(COD)_2$) at room temperature. Using poly(vinylpyrrolidone) (PVP) as a stabilizer, monodisperse nanoparticles can be obtained with tunable sizes (20-30nm) depending on the the Ni/PVP ratio [101, 102]. Cobalt nanoparticles of approximately 6 nm have also been synthesized using this method with reproducible results [103].

2.2.2.3.2 Reduction of Metallic Salts

An economical method to obtain nanoparticles is the chemical reduction of metal salts [96]. Generally the reduction is performed in the presence of a surfactant which prevents the agglomeration of the insoluble metal [94]. One commonly employed variant of this method is the polyol process. Here, metal salts are dissolved in a liquid polyol which acts as the solvent, reducing agent and oxidation stabilizer at the same time [104]. Under and inert atmosphere the solution is then heated to high temperatures, leading to the formation of fine metal nanoparticles.

Iron nanoparticles can be obtained by reducing iron chloride ($FeCl_3$) with reducing agents such as sodium borohydrate ($NaBH_4$) and hydrazine hydrates ($N_2H_4 \cdot H_2O$). The nature of the products by borohydride reduction strongly depends on the reaction conditions [96, 105]. Huang and coworkers [96] synthesized 6 nm particles of iron from the $FeCl_3$ reduction by $NaBH_4$ using polyacrylic acid as the dispersant and palladium ions as nucleating seeds. By controlling the amount of dispersing agent ad Pd seeds, particles with a variety of diameters and morphologies can be synthesized.

Sodium borohydrate has also been employed in the reduction of cobalt salts [76]. Petit *et al.* [106] employed this compound to produce 5.8 nm particles of Co by reducing

cobalt bis(2-ethylhexyl)-sulfosuccinate ($Co(AOT)_2$) in Na(AOT) micelles. Monodisperse cobalt nanoparticles have been synthesized by the high temperature reduction of $CoCl_2$ in the presence of oleic acid as a stabilizing agent. Here, a Dioctylether solution of superhydride (LiBEt3H) was employed, producing nanoparticles ranging from 2-11 nm with a standard deviation of 7.5% [107].

2.2.2.3.3 Synthesis of Metal Nanoalloys

The synthesis of monodispersed alloy nanoparticles is of fundamental importance for the development of novel technologies. Nanoalloys are formed from the nanoscale co-aggregation of two or more metals with the ability to form compositionally-ordered phases [108]. Nanoalloys are at the border between molecular and bulk state, resulting in unique properties unlike to those of the individual constituents or of the bulk-alloy materials [103, 108].

Recently, a wide variety of nanoalloys have been successfully synthesized, for example: FePt, FeCo, FeNi and CoNi to mention a few. In particular, FePt nanoparticles are important for permanent magnetic applications due to their large anisotropy energy, high coercivity and good chemical stability [109]. CoPt can also be employed for these purposes [110]. When it comes to soft magnetic applications, materials with a large permeability, high saturation magnetization, low coercivity and good stability are required. For this case FeCo is the perfect candidate [111].

The synthesis of these particles can be carried out by simultaneous thermal decomposition of the carbonyl precursors or by reduction of their constituent salts. Zubris *et al.* [108] studied the kinetics involved in the simultaneous decomposition of $Fe(CO)_5$ and $Co_2(CO)_8$ to produce FeCo particles. Although thermal decomposition is often used for the synthesis of Fe and Co nanoparticles, it tends to be very complicated for the synthesis of alloy nanoparticles due to the difference in decomposition temperature.

As an alternative, the polyol process has been widely employed. The reduction of metal ions must happen together, otherwise the formation of separate metal entities or the sole reduction of one of the metals will occur [104]. Elkins and coworkers [112] synthesized monodisperse FePt nanoparticles from the reduction of $Fe(acac)_3$ (acac=acetylacetonate) and $Pt(acac)_2$ by 1,2-hexadecanediol in dioctyl ether. When using a 2:1 molar ratio of $Fe(acac)_3$: $Pt(acac)_2$, high coercivity particles where obtained. Another method for producing monodisperse FePt consists in reducing $Pt(acac)_2$ and simultaneously decomposing $Fe(CO)_5$ under the presence of oleic acid. By controlling the molar ratio of iron carbonyl to the platinum salt, the size and composition of the resulting particles can be controlled [109].

For the synthesis of FeCo the simultaneous reduction of $Fe(acac)_3$ and $Co(acac)_2$ using the polyol method has proved useful for the production of 20 nm particles. Depending on the choice of surfactants, the shape and size of the resulting particles can be controlled [111]. Figure 16 shows the resulting particles synthesized with this method. Kodama *et al.* [113] synthesized cubic FeCo nanoparticles through the polyol process. They found that shape varied from cubic to spherical when resulting particles were rich in Fe or Co, respectively. The final composition can be controlled by modifying the reaction temperature. $FeCl_2$ can also be employed, usually in a polyol of ethylene glycol with NaOH [104].

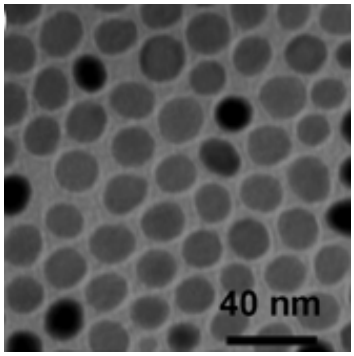

Figure 16. TEM bright-field image FeCo nanoparticles[111].

2.2.3 Surface Functionalization of Magnetic Nanoparticles

Because of their nature as well as potential application, surface modification of magnetic nanoparticles is often indispensable. A great amount of technological applications require magnetic nanoparticles to be homogeneously dispersed in a non-magnetic matrix such as water [114]. One of the limitations of using as-synthesized particles in a colloidal dispersion is the formation of clusters. Due to their large surface to volume ratio, magnetic nanoparticles tend to agglomerate in order to reduce their surface energy. This is the result of magnetic dipole-dipole interactions and has a significant effect in the magnetic properties of the material [79]. Therefore, the coating of the particles helps in the generation of a monodisperse solution.

Another main reason for compatibilizing the particle surface is to retain the physical and chemical properties of the material. Metal nanoparticles such as iron and niquel are easily oxidized under ambient conditions, for which surface coating is needed to maintain their chemical stability [115].

Biocompatibility is another reason why surface functionalization is so important. These particles offer a high potential in the biomedical field, with applications ranging from cellular labeling and tissue repair to drug delivery and magnetic resonance imaging [3]. Particle coating provides them with biocompatibility as well as a biofunctional surface for modification [115].

Several materials can be used for this purpose. Depending on the application, materials such as polymers, surfactants, non-magnetic metals, and monomeric organic molecules have been employed [79, 83, 99, 116]. It has to be taken into consideration that the particle magnetic moment decreases with coating, since there is a partial contribution of diamagnetic material to the total volume [79]. An illustration of nanoparticles coated by a surfactant is shown in Figure 17.

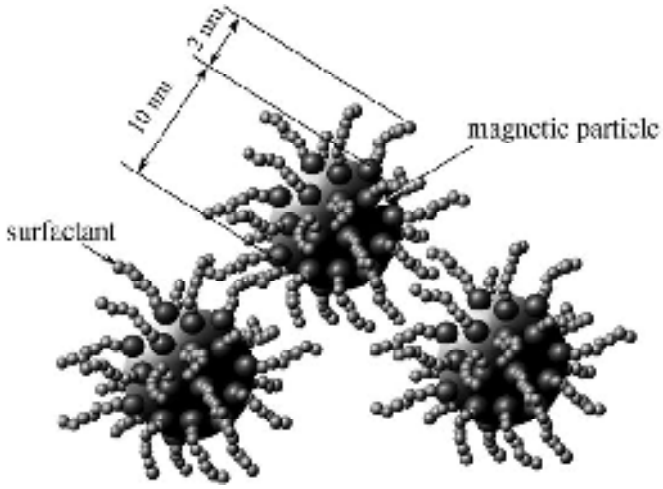

Figure 17. A schematic view of the coated magnetic particles in a ferrofluid[95].

2.2.3.1 P*olymeric Stabilizers*

When using polymers as stabilizers two main techniques may be followed: *grafting to* and *grafting from*. In the *grafting to* technique pre-existing chains are grafted onto the particles surface by electrostatic or hydrophobic interactions, while in the *grafting from* polymerization takes place from the particle surface [117]. Macromolecules can also be physically adsorbed and entangled with the particles. However, one major drawback of all these techniques is the easiness of dissolution and/or depletion .

Liu *et al.* [116] synthesized magnetic microbeads consisting of a magnetite core and a strongly bound polymer coating prepared by microemulsion polymerization of styrene and methacrylic acid. The polymeric coating increased the resistance to corrosion and oxidation of the core. However, the magnetic moment of the particle/coating decreased compared to that of the bulk since the coating decreased the magnetic fraction in the mixture. Flesh *et al.* [118] coated maghemite with poly (ε-caprolactone). The grafting density increased with longer reaction times whereas it decreased when higher molecular weight polymers were employed. The last trend was attributed to steric hindrance. In order to obtain compounds with a high saturation

magnetizations, iron nanoparticles have been coated with polymers such as poly(ethylene glycol) (PEG) [105] and poly(isobutene) (PIB) [97]. Poly(vinylpyrrolidone) (PVP) has been used as stabilizer when working with Co and Ni due to its little interaction with the particle surface, not modifying its magnetic properties [102].

The *grafting from* technique has also been widely used. Chen *et al.* [119] reported the surface-initiated ring opening polymerization of lactic acid on surface functionalized magnetite. The reaction steps are shown in Figure 18. Burke and coworkers [99] produced iron particles by the thermal decomposition process in the presence of a polymeric dispersant consisting of polyethylene (PE), poly (isobutylene) (PIB), and polystyrene (PS). PE and PIB created uniform size individual core/shell particles while particles with PS tend to agglomerate due to interaction between the polymer and the solvent.

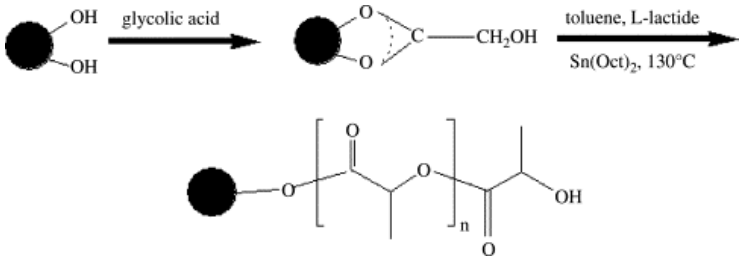

Figure 18. Synthesis scheme of Fe_3O_4–PLA particles via *grafting from* method[119].

2.2.3.2 Non-Polymeric Organic Stabilizers

In order to avoid a large shell thickness, monomeric organic molecules can be employed as particle stabilizers. Oleic acid has been commonly used for coating nanoparticles which will be dispersed in non-polar solvents such as hexane [3, 109, 120]. Sahoo *et al*. [120] reported the surface derivatization of magnetite types of biocompatible phosphates and phosphonates. Stable dispersions were obtained with the phosphates and phosphonates. TGA results suggested a quasi-bilayer structure where the first

layer is strongly bound to the surface of the particle while the second layer interacts through weak Van der Waals forces.

Portet *et al.* [121] developed monomeric organic molecules for homogeneous particle coating employed in magnetic resonance imaging. Magnetite was functionalized with molecules like taurine, imino diacetic acid, nitrilo triacetic acid, among others. They found that biphosphonates were the more efficient to stabilize these particles at neutral pH.

2.2.3.3 Non-Organic Stabilizers

Synthesis of core-shell structures, in which the core consists of a magnetic compound and the shell of a metallic one, have been developed by several research groups. Iron by itself has one of the largest specific magnetization but it tends to oxidize under ambient conditions and ignites spontaneously [83]. When coated whit a noble metal such as gold, particles are stable at ambient conditions and retain most of their magnetic properties [3]. The microemulsion technique is usually employed to synthesize these compounds. Once the magnetic core is formed, the micelles are expanded using a larger micelle and the shell is formed by adding a third solution of a metal salt immediately after[92]. Fe-Au [83, 86, 122], Co-Au [123] and Fe_3O_4-Ag [124] core-shell structures have been synthesized following this method.

The deposition of silica (SiO_2) shells on magnetic particles has been reported by several authors [76, 114, 115]. Silica has several advantages over other surfactants such as providing an excellent stability in aqueous solution, improving the particle's chemical stability and offering a biofunctional surface for modification [3]. Fu *et al.* [114] synthesized cobalt nanoparticles covered by SiO_2. A uniform silica shell which thickness changed with time was obtained. The particle's magnetic properties could be tailored by controlling the coating thickness. Figure 19 shows the TEM images of these particles under different reaction times. Using a modified sol-gel route, Aslam

and coworkers were able to encapsulate FePt in SiO_2. This method also worked with Co, Fe and Ni as the magnetic core.

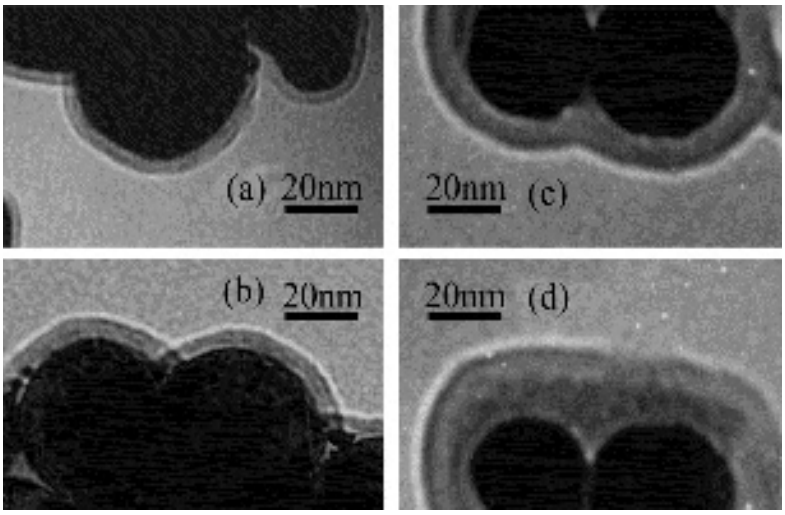

Figure 19. High magnification TEM images of silica shell thickness of core–shell Co/SiO_2 composite nanoparticles changing with reaction time: a) 1hr, b) 3hr, c) 4hr, d) 10hr[114].

2.2.4 Characterization of Magnetic Nanoparticles

It is of utmost importance the characterization of magnetic nanoparticles since their potential applications depend on parameters such a size and magnetic properties. To achieve this, high resolution equipment are needed in order to determine their properties which lie in the nanometric range.

Transmission Electron Microscopy (TEM) is frequently employed for determining average particle size, size distribution, shape and dispersion [77, 123]. Depending on its composition, the coating thickness may or it may not be evaluated by means TEM. Polymeric or silica stabilizers may be distinguished from the magnetic core, allowing the determination of its thickness [99, 114]. For particles in which the coating consists of a metal, such as Fe/Au nanoparticles, *Electron Dispersive Absorption Spectroscopy* (EDAX) provides an elemental analysis of the particle, allowing one to calculate the core diameter and the coating thickness [83]. Cryo-TEM is

employed for analyzing liquid films that had been cooled sufficiently fast to avoid crystallization. This proves useful to analyze particles in solution [97].

Another technique employed in the determination of particle size, as well as distribution, is *Dynamic Light Scattering* (DLS). By obtaining the diffusion coefficient, one is capable of determining the hydrodynamic radius (R_h) of particles in solution through the Stokes-Einstein equation [125]. For the case of functionalized particles, the hydrodynamic radius consists of both the magnetic core and the coating. By subtracting the core diameter from R_h, obtained usually with TEM, one can estimate the average thickness of the stabilizer [126].

In order to study the crystallographic nature of the particles, *X-Ray Diffraction* (XRD) is usually employed [92]. This technique is also useful for estimating the average particle size using the Scherrer equation [127].

Of particular interest is the study of their magnetic properties. Depending on the magnetization degree of the system, magnetization measurements can be performed with either a *Superconducting Quantum Interference Device* (SQUID) or a Vibrating Magnetometer [72]. Besides magnetic properties such as blocking temperature (T_b), saturation magnetization (M_s), coercivity (H_c) and remanescence, an estimate of the particle size can be obtained from the magnetic susceptibility as well as the saturation magnetization value [4, 83]. From the blocking temperature, one can also estimate the particle size as long as the anisotropy constant is known [68].

Molecular characterization of the particle coating can be done by several techniques such as Fourier Transform Infrared Spectroscopy (FTIR), Electron Difraction Scattering (EDS) or Atomic Absorption Spectroscopy (AAS) [91, 111, 128]. Willis *et al.* [128] employed Nuclear Magnetic Resonance (NMR) to study the interaction at the interface between maghemite and oleic acid. Even though NMR is difficult to perform with magnetic materials, they were able to obtain sharp resonance peaks

which allowed them to determine the change in chemical structure of the oleic acid due to its interaction with the surface of the particles. This analysis can also be done using FTIR [60].

2.3 Magnetoviscous Effect in Ferrofluids

One of the most important properties of magnetic fluids is the possibility to exert a significant influence to their flow and physical properties by means of moderate magnetic fields. For the first time in 1969, Rosensweig *et al.* [129] published a paper dealing with viscosity changes in colloidal suspensions of magnetic particles. They reported an increase in the viscosity of a ferrofluid composed of nanosized particles under the influence of an external magnetic field. This was called the *Magnetoviscous Effect* and has been a topic of great interest for the past 30 years.

2.3.1 Magnetoviscous Effect in Diluted Ferrofluids

Numerous articles dealing with changes in viscosity of diluted suspensions of magnetic nanoparticles have been published over the last 30 years. McTague [7] published a paper describing the change in viscosity of diluted suspensions of cobalt particles. The final theoretical explanation for this phenomenon was given by Shliomis and it represents the basis for the theory of ferrohydrodynamics [130].

When an external field is applied to a ferrofluid the moment of each magnetic nanoparticle tends to align with the field experiencing a torque$\mu_o \bar{m} \times \bar{H}$. Two important processes are in charge of determining how long it takes to align *m* with *H*: the Brownian relaxation and the Neel relaxation. In the former, the magnetic moment is fixed to the particle within the hydrodynamic volume V_h and the whole rotates within the fluid with viscosity η. During the Neel relaxation, the magnetic moment rotates relative to the crystal axis without particle rotation. Their characteristic time is given in Equation 17 and 18, where τ_B corresponds to the Brownian relaxation and τ_N to the Neel relaxation[15].

$$\tau_B = \frac{3\eta V_h}{kT} \qquad (17)$$

$$\tau_N = \tau_0 e^{KV_p/kT} \qquad (18)$$

In the Neel relaxation time, K represents the materials anisotropy constant and V_p the volume of the magnetic core. At a diameter near the size of particles commonly making up ferrofluids, both effects are comparable in rate. For a ferrofluid with particle diameter of 10nm, the Brownian relaxation time is in the order of $10^{-7} – 10^{-6}$s. In the case of particle aggregation, τ_B can reach 10^{-4}-10^{-2}s.

Under the influence of a shear flow, the particles contained within a ferrofluid will rotate with their axis of rotation parallel to the vorticity of the flow. One main assumption is that these nanoparticles have their magnetic moment fixed in an easy axis. This means that the Brownian relaxation is orders of magnitude shorter than the Neel relaxation, making the particles magnetically hard [131].

When an external magnetic field is applied to a ferrofluid two different extreme situations have to be considered. First, the applied magnetic field is perpendicular to the vorticity of the flow (Figure 20-a). The magnetic field will try to align the moment in the field direction while the viscous torque exerted by the flow tries to rotate the particle, forcing a misalignment of magnetic moment and field. This force will give rise to a magnetic torque trying to realign the moment, counteracting the free rotation of the particle in the flow and increasing the fluid's viscosity. The change in viscosity should reach a maximum at high magnetic field strengths, when the rotation of particles is completely hindered. In the second situation, the field can be applied collinear with the vorticity (Figure 20-b). Here the magnetic moment is aligned with the direction of the field and no influence on the rotation of the particle will appear, resulting in no change in the viscosity of the fluid [131].

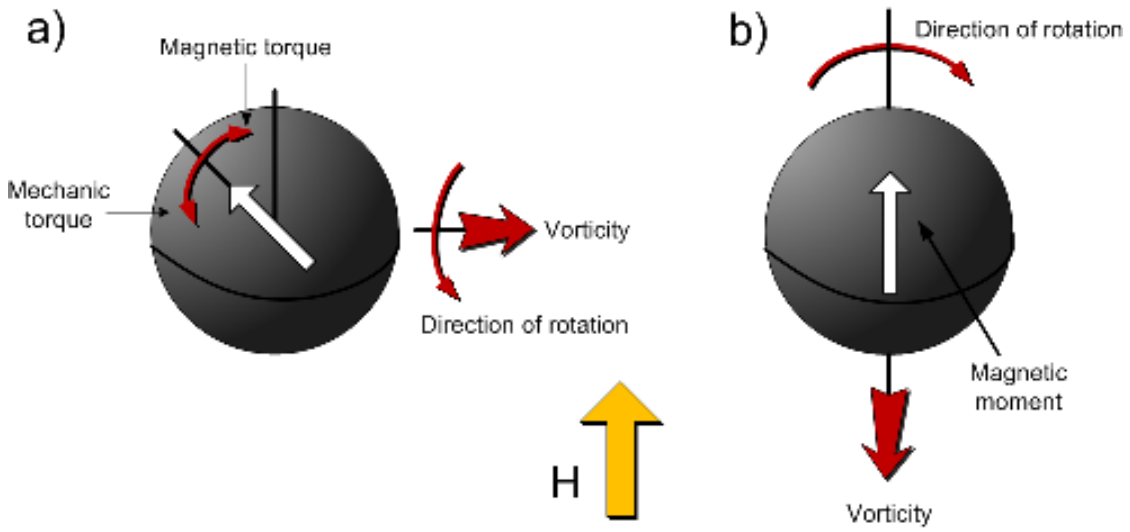

Figure 20. The origin of rotational viscosity. An increase in the viscosity of the fluid is observed when the applied magnetic field is perpendicular to the direction of vorticity (a). Adapted from (131).

Two major assumptions were made in this discussion. First, the magnetic moment is fixed within the particle; hence the Brownian relaxation dominates in the process. Second, no interaction between particles is considered based on the assumption that the suspension is highly diluted. As will be discussed later, these assumptions fail most of the times since commercially ferrofluids are usually not diluted. Nonetheless, with these assumptions there is a good qualitatively agreement between experimental results and theory [8, 77, 131].

McTague [7] investigated the effect of a static external field in the flow of a ferrofluid inside a capillary. The suspension consisted in Co nanoparticles of approximately 6nm in diameter and the position of the field was applied parallel and perpendicular to the flow. In their results they observed a larger increase in viscosity (approximately two times higher) with the parallel field as compared to the perpendicular. When the field is parallel to the flow a perpendicular arrangement

between the field and the vorticity is created, resulting in a larger hindrance of particle rotation. In contrast, applying the field perpendicular to the flow direction leads to the necessity of averaging over the angle between the field and vorticity, since the direction of the vorticity vector varies across the diameter of the capillary. This leads to a viscosity increase of approximately half the value than the one obtained with a parallel arrangement [131]. The vorticity of the flow within the capillary is given by:

$$\Omega_{tube} = \frac{V_{oz} r}{a^2} \tag{19}$$

were a is the tube diameter, v_{oz} the maximum velocity of flow in the direction of flow and r the variable radial distance.

A first theoretical approach to explain this behavior was given by Hall and Busenberg [132]. Based on the physics of rotation hindrance previously discussed, they end up with an extension of Einstein's viscosity for suspensions:

$$\eta_{(H)} = \eta_0 \left[1 + \frac{5}{2}\phi + \frac{3}{2}\phi' sin^2\varepsilon\right] \tag{20}$$

where ϕ' denotes the volume fraction of particles with surfactant and ϕ the volume concentration of all suspended material. The magnetic contribution is given by:

$$sin^2\varepsilon = \frac{1}{2}(1 + \xi^{-2}) - \left[\frac{1}{4}(1 + \xi^{-2}) - \xi^{-2} sin^2\beta\right]^{\frac{1}{2}} \tag{21}$$

Here, β represents the angle between the vorticity vector and the magnetic field and ξ (22) the ratio between the magnetic and viscous torque acting on a particle.

$$\xi^{-1} = \frac{\mu_0 m H}{4\pi\eta_0 d^3 \dot{\gamma}} \tag{22}$$

Theory and experiments agree qualitatively well with this approach in the limit of high fields, predicting an increase in the viscosity with the parallel setup of double the value of the one obtained with a perpendicular setup. For low fields this theory predicts a too strong increase, which results from neglecting the competition between thermal motions of the particles [131]. Nevertheless, it represents the starting point to the theory of ferrohydrodynamics postulated by Shliomis *et al.* [8]. In this theory Shliomis

defines a rotational viscosity which is the field dependent part of the viscous friction in a ferrofluid. A simple expression to relate the rotational viscosity with the external field was derived:

$$\Delta\eta = \frac{3}{2}\eta\varphi\frac{\xi - tanh\xi}{\xi + tanh\xi}sin^2\beta \qquad (23)$$

with $\xi = mH/kT$ being the Langevin parameter, which relates the ratio of the energy of the particle's magnetic moment to the thermal energy (absent in the theory derived by Hall and Busenberg), φ=nV is the volume concentration of particles and β represents the angle between **H** and **Ω**. Here **Ω** refers to the angular velocity (previously defined as vorticity) of a volume element within the liquid and is denoted by $\mathbf{\Omega} = \nabla \times \mathrm{v}/2$, where v represents the fluid velocity [130].

For a low stationary field, Equation 23 reduces to

$$\Delta\eta = \frac{1}{4}\eta\varphi\xi^2 \qquad for\ \xi \ll 1 \qquad (24)$$

And tends to a saturation value at strong fields given by:

$$\Delta\eta = \frac{3}{2}\eta\varphi \qquad for\ \xi \gg 1 \qquad (25)$$

The above theoretical analysis is in excellent agreement with the experimental results reported by McTague. The authors made the assumption of dilute suspensions, were one can neglect both hydrodynamic and magnetic interparticle interactions [8].

Up to now the magnetoviscous effect has only been considered for stationary fields. It wasn't until 1994 when for the first time Shliomis proposed the theory of induced negative viscosity under an alternating, linearly polarized field $H = (H_o \cos\omega t\,, 0,0)$ [8]. When the field is shifted in direction the particle's magnetic moment regains its equilibrium by means of Brownian or Neel relaxation. The orienting influence of an alternating field decreases with increasing frequency. This influence tends to zero for $\omega\tau_B >> 1$ since the particle does not have enough time to remagnetize. According to the previously discussed theory a reduction in the

magnetization of the particle should be accompanied by a reduction in rotational viscosity, approaching zero for $\omega\tau_B \to \infty$.

When solving the ferrohydrodynamic equations, the fluid's viscosity behavior resulted to be much more interesting than expected. At a characteristic field frequency ω_0 $\Delta\eta$ changes its sign from a region of positive to negative values. Within this negative region, $\Delta\eta(\omega)$ attains a minimum and after that begins to grow up until it reaches zero for $\omega\tau_B \to \infty$. This solution takes into account static as well as alternating applied fields.

The following set of equations, consisting of the equation of fluid motion (26), the magnetization equation (27) and the equation of rotational motion of the particles (28), are the base for the theory of ferrohydrodynamics proposed by Shliomis and Morozov [8]:

$$\rho \frac{d\mathbf{v}}{dt} = -\nabla p + (\mathbf{M}\cdot\nabla)\mathbf{H} + \eta\Delta v + \frac{1}{2\tau_s}\nabla\times(\boldsymbol{\Theta}-\boldsymbol{\Omega}) \qquad (26)$$

$$\frac{d\mathbf{M}}{dt} = \boldsymbol{\Theta}\times\mathbf{M} - \frac{1}{\tau_B}(\mathbf{M}-\mathbf{M_0}) \qquad (27)$$

$$I\frac{d\boldsymbol{\Theta}}{dt} = \mathbf{M}\times\mathbf{H} - \frac{1}{\tau_s}(\boldsymbol{\Theta}-\boldsymbol{\Omega}) \qquad (28)$$

Here $\boldsymbol{\Theta}$ is the macroscopic angular velocity of the rotating particles, $\boldsymbol{\Omega}$ the angular velocity of a local volume element, $\tau_s = \rho_s d^2/60\eta$ the decay time for the deviation of $\boldsymbol{\Theta}$ from $\boldsymbol{\Omega}$ in the absence of magnetic field, I the sum of particles moment of inertia over a unit volume and $\mathbf{M}_0$ the "instantaneous" equilibrium magnetization that would exist in a given H(t) at τ_B=0.

The resulting expression that describes the rotational viscosity behavior under static and alternating fields is given by:

$$\Delta\eta = \frac{3}{2}\eta\varphi\frac{\boldsymbol{\Omega}-\boldsymbol{\Theta}}{\boldsymbol{\Omega}} \qquad (29)$$

$$\boldsymbol{\Theta} = \boldsymbol{\Omega}\left(1 - \frac{\xi^2}{6}\frac{(1-\xi^2\tau_B^2)}{(1+\omega^2\tau_B^2)^2}\right) \qquad (30)$$

The explanation for this set of equations goes as follows: in the absence of an external field, the particles rotate together with the fluid ($\boldsymbol{\Theta} = \boldsymbol{\Omega}$), resulting in $\Delta\eta = 0$. A static or slowly varying field ($\omega\tau_B << 1$) hampers the rotation of the particles in the vortical flow. Here the particles rotate slower than the fluid ($\boldsymbol{\Theta} < \boldsymbol{\Omega}$) forcing the latter to to flow past the particles, which leads to an additional dissipation of the kinetic energy of the fluid. This behavior manifests in an increase of the rotational viscosity, reaching the saturation value given by (25). Under a fast, alternating field ($\omega\tau_B > 1$) the particles rotate faster than the fluid ($\boldsymbol{\Theta} > \boldsymbol{\Omega}$), accelerating it and resulting in $\Delta\eta < 0$. This decrease is the consequence of transforming part of the alternating field into kinetic energy of the fluid [8]. Figure 21 shows the dependence of the relative rotational viscosity with the frequency of the field.

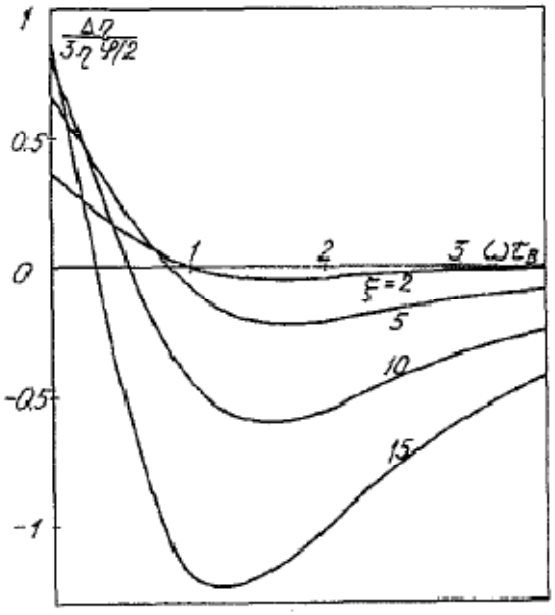

Figure 21. The relative rotational viscosity as a function of the frequency of the field for different values of the Langevin parameter ξ calculated from Equation 29 and 30[8].

The first experimental evidence of the negative viscosity effect was given by Bacri *et al.* [6]. In their work, they used a ferrofluid composed of cobalt ferrite particles in water with a large anisotropy constant. The particles possessed an average diameter of 10nm and had their magnetic moments fixed to one of their easy axis. In order to maximize the effect, a concentrated solution of 20%wt was employed. For viscosity measurements their setup consisted of a horizontal capillary inside a solenoid capable of producing an alternating field.

The experimental reduced viscosity obtained with a magnetic field of arbitrary magnitude and frequency, $\eta_r(H,f)$, was calculated by means of $\eta_r(H,f) = \Delta\eta/\eta(0,0) = [\eta(H,f) - \eta(0,0)/\eta(0,0)]$. Figure 22 shows their experimental results. The viscosity of the magnetic fluid was tuned between 220 and 50cP by employing magnetic fields up to 2500Oe and frequencies between 0 and 700Hz.

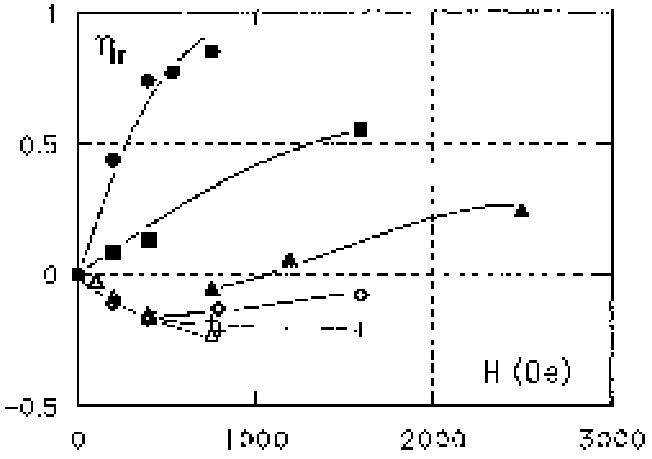

Figure 22. Experimental reduced viscosity versus magnetic field for different frequencies f: •: f = 0Hz; ■:f=52Hz; ▲: f = 150Hz; ◊: f = 345Hz; +: f = 645Hz; Δ: *f*=1480H [6].

Zeuner *et al.* [133] performed experiments on negative and positive magnetoviscosity using a 4.5wt% solution of magnetite. The experimental setup used in this study is shown in Figure 23.

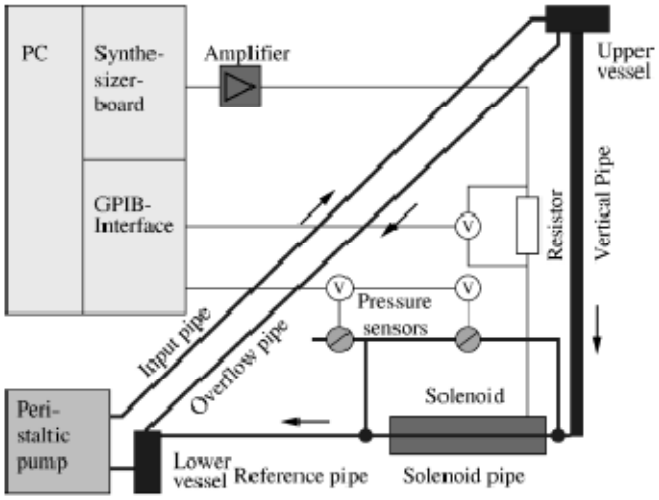

Figure 23. Schematic diagram of the experimental apparatus employed by Zeuner *et al.* to measure the negative viscosity effect[133].

Zeuner compared quantitatively their experimental results with the model proposed by Shliomis and Morozov [8].When fitting their results two main inconsistencies appeared: the value of the hydrodynamic volume resulted too high and the τ_B appeared to be frequency dependent. These discrepancies were attributed to the assumptions made in the theoretical model. Their experiment dealt with a broad distribution of particle size and therefore, magnetic moments and Brownian relaxation times. In contrast the theory assumes a monodisperse sample. Moreover the theory was developed for diluted samples. Zeuner employed a solution loaded with 4.5wt% of magnetite in water. This solution had a lower concentration than the one employed by Bacri and coworkers [6]. Still, this concentration could still be too large to satisfy the original assumptions. Taking into account these discrepancies a good qualitative agreement between theory and experimental results was obtained.

2.3.2 Magnetoviscous Effect in Concentrated Ferrofluids

The previously discussed theory assumes monodisperse samples and neglects interparticle interactions. Commercial ferrofluids are usually polydisperse, with

particle size ranging from 5-15nm and volumetric concentrations up to about 10% [66]. When dealing with these materials, particle interactions cannot be ignored.

As mentioned earlier only the magnetically hard particles contribute to the viscosity change. Their magnetic relaxation mechanism strongly depends on particle size. For magnetite, the critical diameter for the transition from Neel relaxation to magnetically hard behavior is around 13nm. Additionally, due to magnetic interactions larger particles tend to form agglomerates [77].

Zubarev *et al.* [134, 135] proposed a new theoretical model that aims to explain the change in viscosity of a concentrated ferrofluid. To take into account the polydispersity of the system, a bidisperse liquid consisting of two fractions of particles with significant difference in diameters is used. It is assumed that one of the fractions consists of smaller particles with a diameter close to the mean average and a concentration close to the overall concentration of magnetic material. The second fraction is assumed to be highly diluted and the particle diameter is large relatively to the one in the first fraction.

The large particles can form chain like aggregates. These aggregates are treated as rigid rod-like materials. The magnetic particle interaction occurs only within chains and not between. Additionally, interaction between particles of different fractions is neglected, as it is small compared to the interaction between large particles. Finally, the interaction between neighboring particles is greater than that between a single particle and the magnetic field, leading to an alignment of the magnetic moment with the axis of the chain [135].

In their work, they obtained an expression for the mean number of particles in a chain described by

$$\langle n \rangle = \frac{\phi_1'}{V_1' \sum_n g_n} \qquad (31)$$

Where ϕ_1' and V_1' being the concentration and particle volume of the large fraction and g_n represents the distribution function of interaction energies with the field and nearest neighbor. Knowing$< n >$, one can calculate the components of the stress tensor σ of the system and its rheological properties for vanishing shear rate $\dot{\gamma}$ [136].

The effective viscosity of the suspension can be given by

$$\eta = \frac{\sigma}{\dot{\gamma}} \qquad (32)$$

Using this approach they have calculated the viscosity dependence on the applied field for a commercial ferrofluid with 6.7%wt of magnetic phase and a mean diameter of 10nm using a special rheometer for magnetic measurements. Additionally, they calculated η(H) for vanishing γ and fitted the diameter and hydrodynamical volume concentration of the large particles. Figure 26 shows the comparison between experimental and theoretical results.

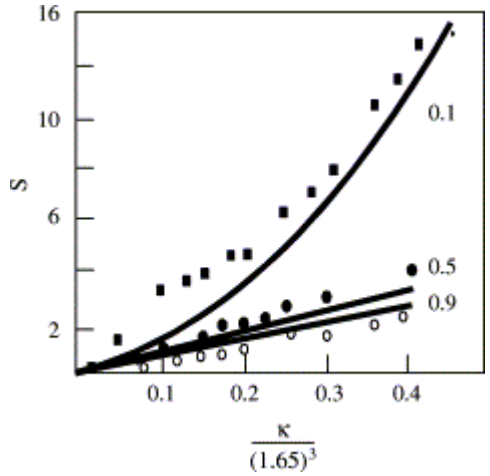

Figure 24. Experimantal (dots) and theoretical (lines) dependences of parameter S of magnetoviscous effect on dimensionless magnetic field κ for different shear rates[136].

Here $\kappa = \mu_0 mH/kT$ and $S = (\eta(H) - \eta(0))/\eta(0)$. A good agreement can be seen between theoretical and experimental results. The strong magnetoviscous effect at small shear rates is attributed to the chain-like agglomerates of large particles. When the shear rate increases, the chains are destroying and the magnetoviscous effect

disappears fast. The small particles with sizes near typical mean sizes in real magnetic fluids are too small to unite into heterostructures. Therefore, they don't contribute to the magnetoviscous effect.

3. EXPERIMENTAL PROCEDURE

3.1 Materials

Polyethylene oxide (PEO) (Mw~2,000,000 g/mol, CAS: 253222-68-3), $CoCl_2 \cdot 6H_2O$ (CAS:7791-13-1), poly(ethylene glycol) methyl ether (PEG) (Mw~2.000 g/mol, CAS: 9004-74-4), diethyl ether (CAS: 60-29-7), toluene (CAS:108-88-3), acetic acid (CAS: 64-19-7), oleic acid (CAS: 112-80-1), ethanol (CAS: 64-17-5) and 1-octadecene (CAS: 112-88-9) were purchased from Sigma-Aldrich. Sodium Oleate (CAS: 143-19-1) was obtained from TCI. $FeCl_2 \cdot H_2O$ (CAS: 10025-77-1) was purchased from Acros. A water based ferrofluid MSG W11 from Ferrotec Corporation was provided by our collaborators at the University of Puerto Rico. All solutions were prepared using deionized water.

3.2 Magnetic Nanoparticles

3.2.1 Magnetite (Fe_3O_4)

Magnetite nanoparticles were obtained from Ferrotec (MSG W11). The properties of this material were provided by our collaborators at the University of Puerto Rico. The ferrofluid has a magnetic saturation of 0.02 Tesla with a particle volumetric percentage of 3.6%. The synthesis procedure and surfactant composition are unknown. At room temperature this material behaves as superparamagnetic, showing no net magnetization in the absence of an external magnetic field {Reference proceeding}. Figure 24 shows a TEM micrograph of the magnetite nanoparticles from the commercial ferrofluid.

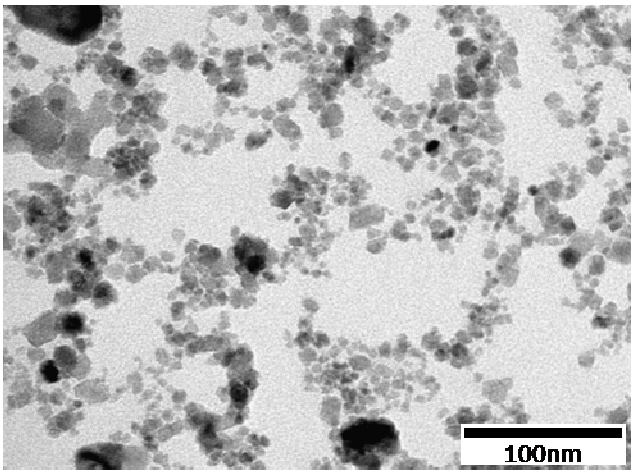

Figure 25. TEM micrograph of the MSG W11 commercial ferrofluid.

The average particle diameter was measured with an image analyzer software (Image J). Figure 25 shows the particle size distribution for the commercial ferrofluid. The sample consists of a fairly polydisperse collection of particles, with sizes ranging from 4 to 16nm. The average diameter was calculated to be 8.7 ± 3.0 nm.

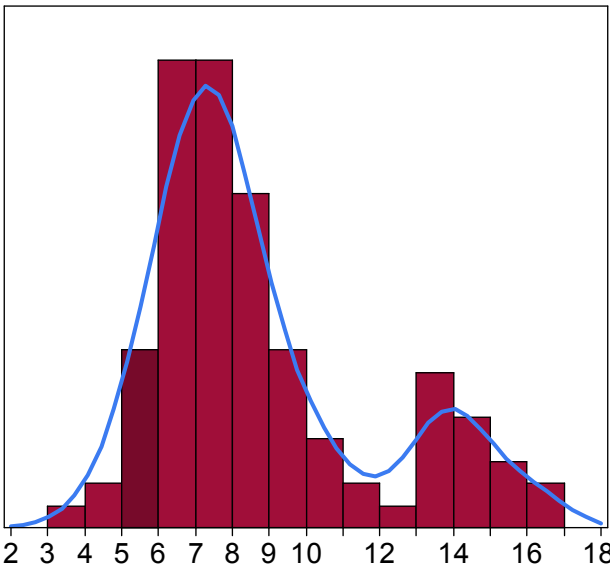

Figure 26. Particle size distribution for the MSG W11 commercial ferrofluid. Particle size exhibited a bimodal distribution centered at 7.5 and 14nm. An average diameter of 8.7 ± 3.0 nm was calculated.

3.2.2 Cobalt Ferrite ($CoFe_2O_4$)

Cobalt ferrite nanoparticles were synthesized following a thermal decomposition method proposed by Park *et al*. [137] by our collaborators at the University of Puerto Rico. The synthesis consisted of three steps. First, a metal–oleate complex was prepared by reacting metal chlorides and sodium oleate. In a typical synthesis of iron–oleate complex, 5.40g of iron chloride ($FeCl_3 \cdot 6H_2O$), 2.40g of cobalt chloride ($CoCl_2 \cdot 6H_2O$) and 24.36g of sodium oleate were dissolved in a mixture solvent composed of 50 ml ethanol, 50 ml distilled water and 100 ml hexane under continuous stirring (100rpm). The resulting solution was heated to its boiling point for four hours. After cooling, the upper organic layer containing the iron–oleate complex was separated and washed three times with distilled water in a separatory funnel. After washing, hexane was evaporated off, resulting in the iron-cobalt-oleate.

25g of the synthesized iron-cobalt-oleate complex and 2g of oleic acid were dissolved in 100mL octadecene under continuous stirring (100rpm) at room temperature. The reaction mixture was heated to 320 °C at a constant heating rate of 3.3 °C/min, and then kept at that temperature for 3 hours. N_2 is added to the reaction until it reaches 200^{o}C. After cooling down, the resulting solution was washed with acetone and the particles were precipitated using a magnet bar. The resulting nanoparticles (shown in Figure 26) consisted of a cobalt ferrite core coated with oleic acid. As seen in Figure 26, good dispersion and well defined shapes were obtained with this method. Particle size ranged from 8 to 24nm with an average diameter of 14.2 ± 2.1 nm.

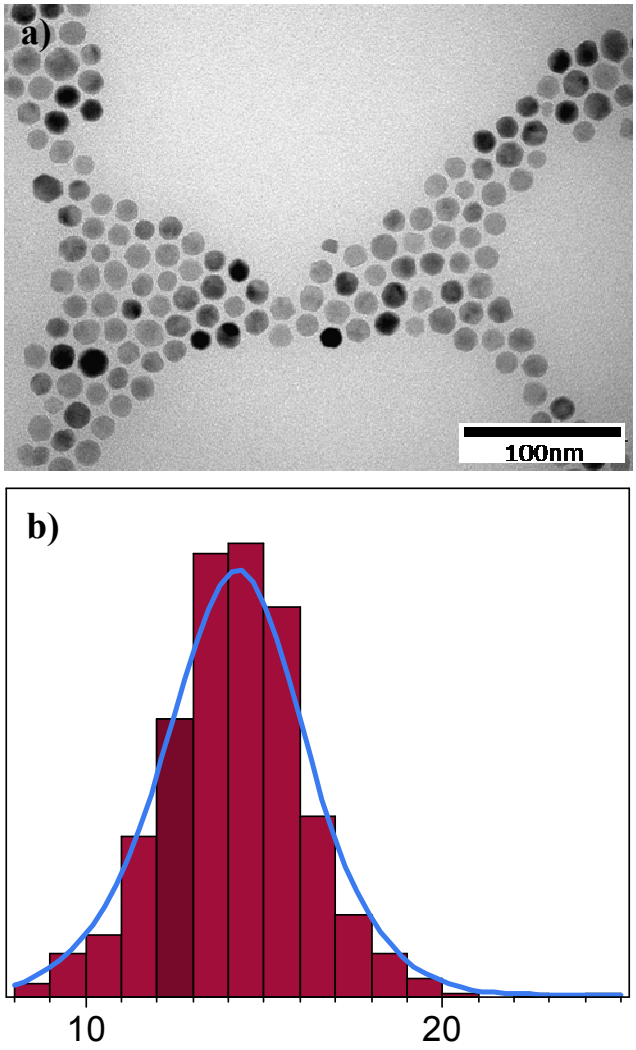

Figure 27. a) TEM micrograph and b) Particle size distribution for the synthesized $CoFe_2O_4$ nanoparticles. Particle size ranged from 8 to 24nm with a with an average diameter of 14.2 ± 2.1 nm.

To avoid agglomeration when mixing the particles with the polymer solution, the oleic acid on the surface of the nanoparticles was exchanged for PEG-Silane following the method reported by Barrera *et al.*[138]. 3g of PEG-Silane and 0.2g of cobalt ferrite nanoparticles were dissolved in 90mL of toluene and sonicated to promote a good dispersion. 50mL of acetic acid was added to the homogeneous solution, allowing it to stir for 72 hours. After stirring, the particles were precipitated

using diethyl ether. The resulting particles consisted of a core of cobalt ferrite coated by PEG. As seen in Figure 27, agglomeration was less significant when coating with PEG-Silane.

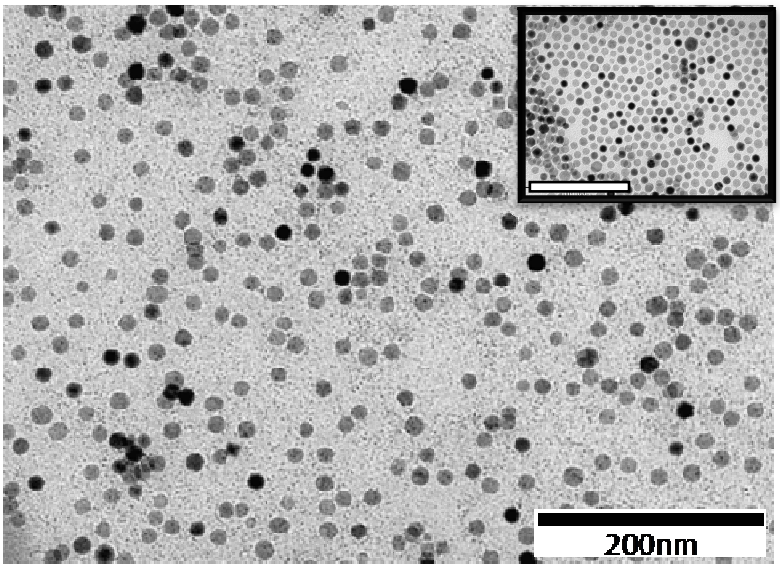

Figure 28. Cobalt Ferrite nanoparticles coated with polyethylene glycol (PEG) with a molecular weight of 2,000g/mol. The insert corresponds to the cobalt ferrite particles coated with oleic acid. The proximity between particles decreased when exchanging the oleic acid for PEG. The white scale bar corresponds to a distance of 200nm.

3.3 Solution Preparation

2g of PEO were dispersed in 100mL of water and stirred for 24 hours. Magnetic nanoparticles were added as needed to obtain solutions containing 1vol% Fe_3O_4, 5vol% Fe_3O_4 and 1vol% of $CoFe_2O_4$ to PEO. This resulted in solutions loaded with 0.04vol%Fe_3O_4, 0.2vol%Fe_3O_4 and 0.04vol%Fe_3O_4. Two magnetite solutions of each concentration were prepared and dispersed using either a mechanical stirrer (Fisher Scientific; Cat: 14-503Q) or a sonicator (Fisher Scientific FS20; Cat: 15-335-20) for 22 hours. Due to limiting amounts, cobalt ferrite nanoparticles were only dispersed by mechanical stirring. Two PEO solutions, one of them subjected to sonication and the other mechanically stirred for 22 hours, were prepared as a control.

3.4 Electrospinning Experiments

Solutions were electrospun from a 5mL syringe coupled to a copper capillary (OD=1.6mm, ID=0.88mm, Length=75mm, McMaster) using a programmable syringe pump (NE-500 New Era Pump Systems Inc.). To study the magnetoviscous effect, a neodymium ring magnet (OD=3/8", ID=3/16", Length=3/8", B=3725Ga, Axially Magnetized, K&J Magnetics) was placed around the copper capillary. The tip of the needle was connected to the positive electrode of a high voltage power supply (Series EH 0 – 60kV Glassman High Voltage Inc.). Upon applying a voltage, a fluid jet emerged from the tip of the capillary and traveled towards a grounded collector placed 25cm apart. The collector plate consisted of a 15x15cm copper sheet covered with aluminum foil (Fisher Scientific). The spinning time for all samples was 4 minutes. All experiments were carried at room temperature. Figure 28 shows an image of the setup employed for this study.

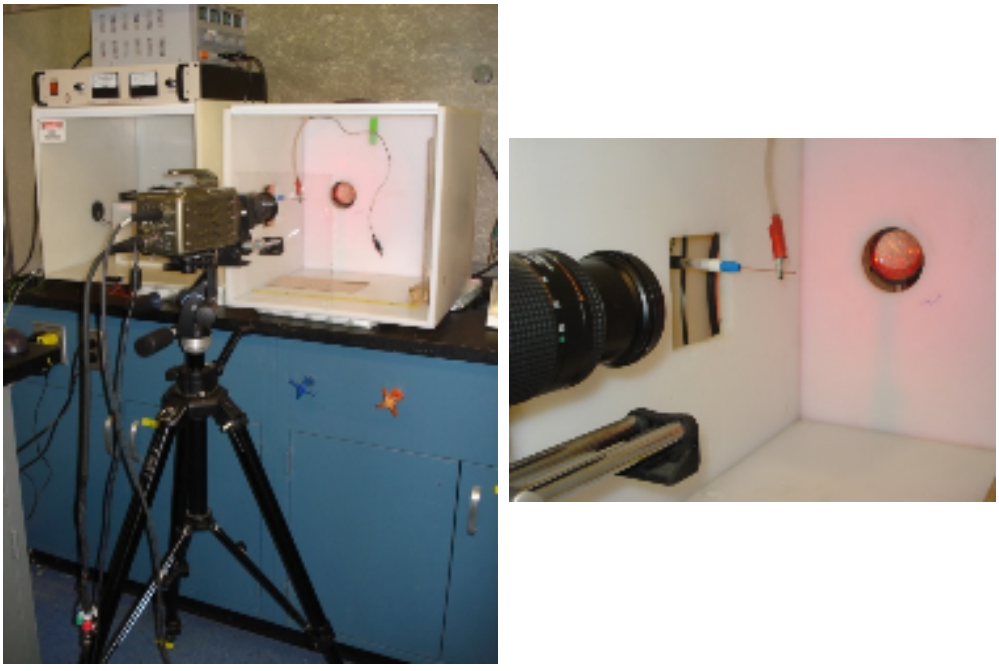

Figure 29. Electrospinning setup employed in this study.

Each solution was electrospun at a flow rate of 0.6, 0.9 and 1.2mL/hr. The applied voltage was varied from 5 to 25kV, in steps of 5kV, at each volumetric flow. This voltage gave us an electric field range of 20-100kV/m (steps of 20kV/m). Furthermore, each combination of flow/voltage was tried with and without the presence of an external magnetic field. A block diagram of the experiments performed with each solution is shown in Figure 30.

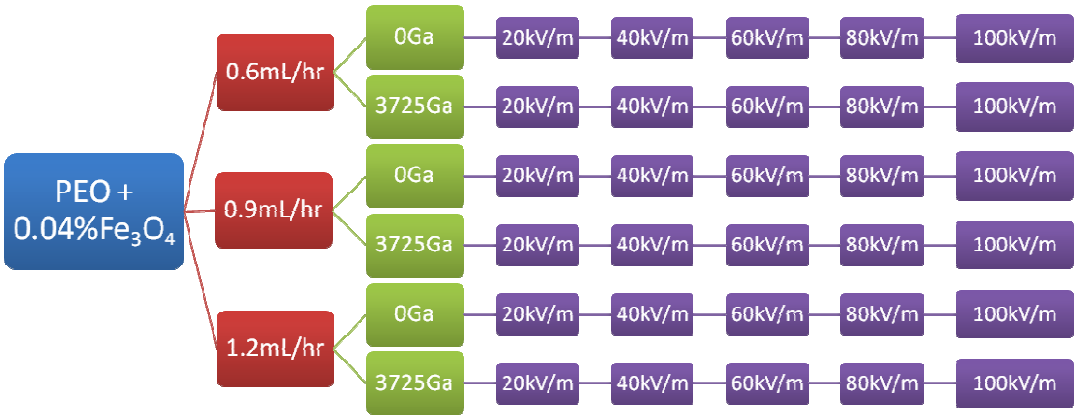

Figure 30. Block diagram showing the experiments performed on each solution.

3.5 High Speed Imaging

The evolution of the electrospun jet at the tip of the capillary was captured using a high speed camera (Phantom V.7.0, Vision Research) equipped with a Nikon AF-Nikkor 105mm lens. Images were acquired at a rate of 6000 frames per second with an exposure time of 20μs. The tip of the capillary was backlit with an LED coupled to a lens. The camera's lens was placed approximately at a distance of 15cm from the capillary in order to avoid disturbing the electric field generated.

After each solution was spinning for about two minutes, approximately 2.3 seconds of video images were recorded. Images were extracted and analyzed using the software Cine Viewer 663 provided by Vision Research.

3.6 Characterization

3.6.1 Surface Tension

Solution Surface tension was measured using a Sigma 701 Tensiometer (KSV Instruments). The experiment consisted in measuring the force required to pull a probe (Wilhemy) out of each solution. Ten repetitions were performed for each solution. The experimental data was analyzed using the KSV Sigma Software.

3.6.2 Conductivity

An IQ170 Scientific Instruments Meter was used for conductivity measurements. For each solution 5 conductivity measurements were averaged.

3.6.3 Viscosity

A TA Instruments AR2000 rheometer was used to perform rheological measurements. Steady state and oscillatory experiments were performed using a double cylinder Couette geometry (couette). A temperature of 20°C was employed for all measurements.

A controlled stress sweep experiment was done in steady flow to determine the shear viscosity of our different solutions. The applied stress was varied from 0.1 to 10Pa for each sample. A frequency-controlled oscillatory test was employed to evaluate the viscoelastic behavior of the different solutions. Data was acquired for all samples in the range of 0.05 – 100 rad/s. This test allowed us to determine the complex viscosity (η^*) and storage modulus (G') of our samples.

3.6.4 Scanning Electron Microscopy (SEM)

A Leica 440 Scanning Electron Microscope (SEM) was employed to study the morphology of the resulting fibers. The electrospun samples were placed on aluminum mount stubs (Electron Microscopy Sciences) and coated with palladium using a Denton Desk II sputter coater. The sputtering time was 30 seconds, giving a 10nm

coating. An accelerating voltage of 5kV and an electron current of 500pA were used for the imaging of all samples.

3.6.5 Field Emission Scanning Electron Microscopy (FESEM)

A LEO 1550 FESEM was employed to study I more detail the surface of the fibers. The electrospun samples were placed on aluminum mount stubs (Electron Microscopy Sciences) and coated with Au-Pd using an Edwards S150A coater. The coating had a thickness around 10nm. An accelerating voltage of 1kV was used for the imaging of all samples.

3.6.6 Transmission Electron Microscopy (TEM)

A FEI Tecnai T12 Transmission Electron Microscope (TEM) was used to study the dispersion of magnetic nanoparticles within the electrospun fiber. A copper grid (Electron Microscopy Sciences) was placed on the aluminum collector, allowing the deposition of fibers onto it. For all measurements, an accelerating voltage of 120kV was employed. A diagram of the collection process is shown in Figure 31.

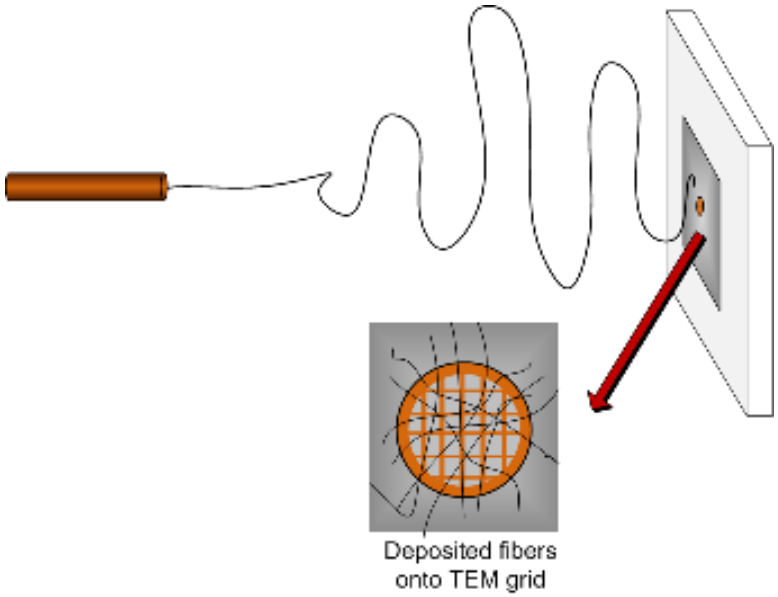

Figure 31. Collection of TEM fibers onto copper grids. A single grid is adhered on the aluminum collector and removed after electrospinning.

3.6.7 Vibrating Sample Magnetometer (VSM)

A Princeton Applied Research VSM Controller (Model 4500) was employed to measure the equilibrium magnetization of the samples. The applied magnetic field was varied from -10,000Oe to 10,000Oe in steps of 400Oe giving a total of 100 points. All experiments were carried at room temperature.

4. RESULTS AND DISCUSSION

4.1 *Effect of Ultrasound Irradiation on the Electrospinning Ability of Polymer solutions*

Magnetite nanoparticles were dissolved in PEO solutions for 22 hours using two different means: mechanical stirring and sonication. When analyzing with SEM a large difference in fiber morphology was observed between the fiber electrospun from a sonicated solution and those electrospun from a solution mechanically stirred (Figure 32).

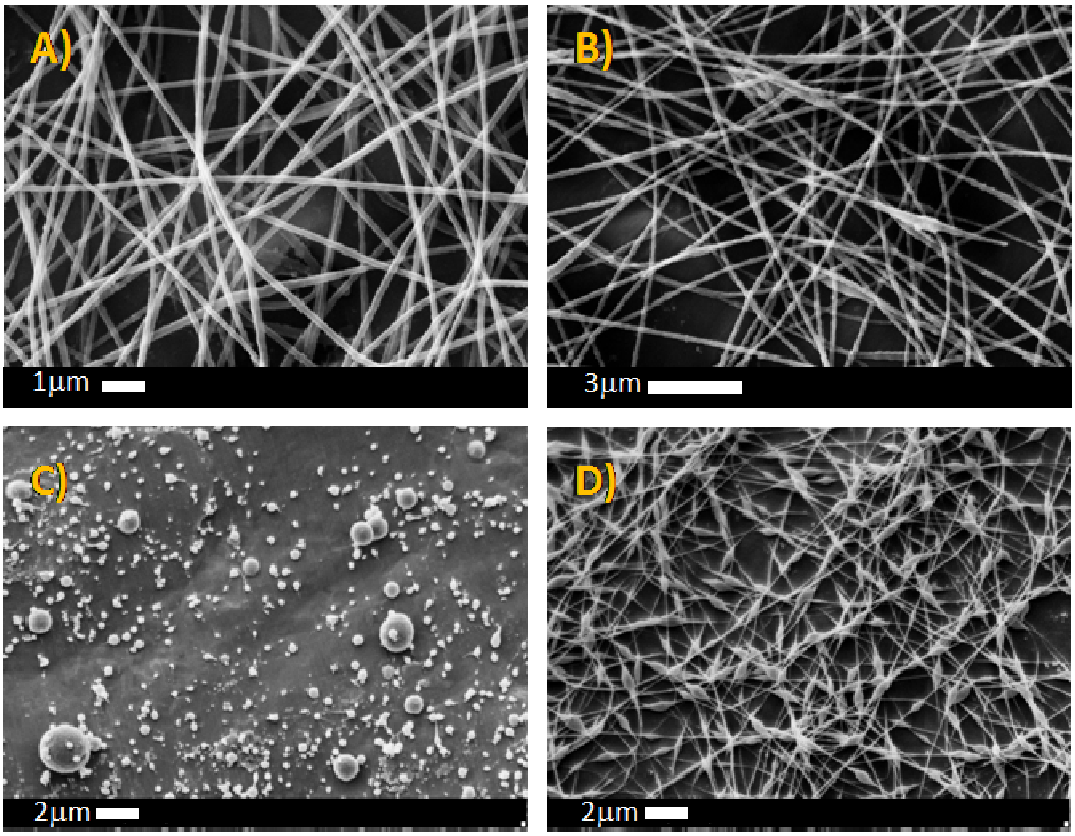

Figure 32. Effect of agitation mechanism on the electrospinning of PEO fibers loaded with magnetite nanoparticles: a) 0.04%Fe_3O_4 mechanically stirred; b) 0.2%Fe_3O_4 mechanically stirred; c) 0.04% Fe_3O_4 sonicated; d) 0.2%Fe_3O_4 sonicated. All solutions were spun at 0.6mL/hr under an electric field of 80kV/m.

The appearance of beads and beaded fibers may be due to a reduction in the amount of chain entanglements. These entanglements have been acknowledged as the primary cause in the formation of fibers [5, 35]. At a fixed polymer concentration the entanglement density can be reduced by decreasing the polymer molecular weight (Mw). A decrease in the polymer's molecular weight can be achieved by sonication [139]. This reduction should also affect the rheological properties of our solutions since viscosity is dependent on Mw. To explore this hypothesis a pure PEO solution was employed as a control. Figure 33 shows the shear viscosity as a function of shear stress for solutions of PEO loaded with different amounts of magnetic nanoparticles dispersed by different means.

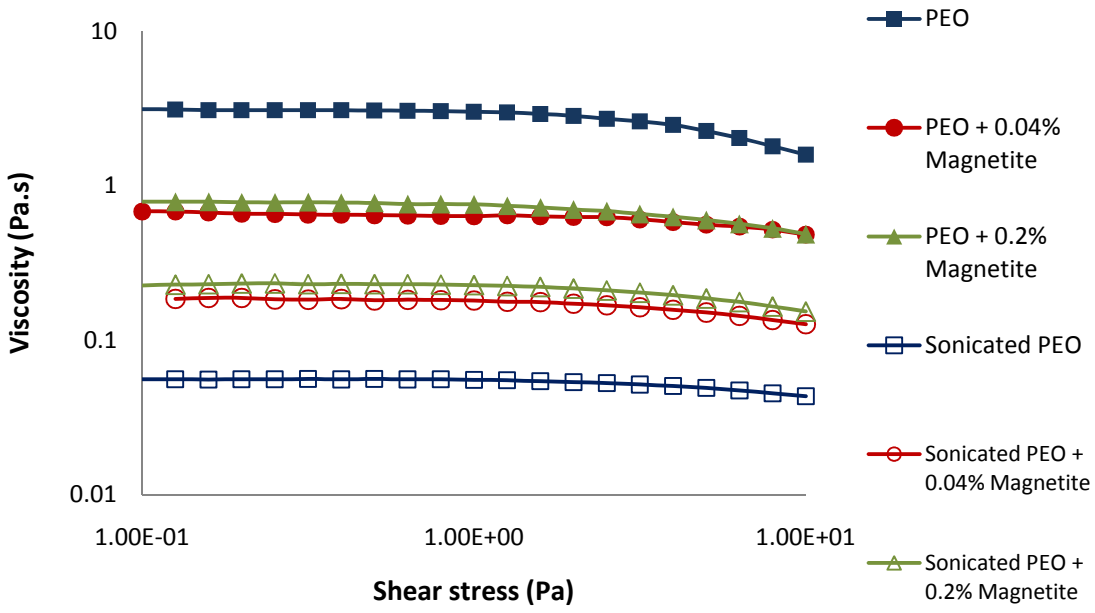

Figure 33. Shear viscosity profiles for the solutions mechanically stirred and sonicated. The addition of nanoparticles appears to reduce the extent at which viscosity decreases after sonication when compared to the pure PEO solution.

According to Figure 33 sonication drastically decreases the terminal viscosity of the pure PEO solution by 98%, from 3.12Pa.s to 0.0561Pa.s. This reduction has been attributed to a decrease in molecular{{}} weight caused by chain scission [139]. During the sonication of polymer solutions degradation can arise from cavitation: the formation, growth, and violent collapse of localized microscopic bubbles generated by ultrasonic irradiation [140]. The wall motion of violently collapsing bubbles causes the movement of neighboring solvent molecules. This movement generates large shear fields responsible for the bond rupture in polymer chains [141]. Bond rupture lowers the molecular weight of the polymer and consequently its viscosity.

Extensive studies on the degradation rate of polymer molecules in solution have been performed. For example, by monitoring the viscosity of a poly(vinyl-pirrolidone) solution as a function of time Taghizadeh *et al.* [142] observed that the largest reduction occurred during the initial period of irradiation. After a given time a constant viscosity value was achieved indicating that no further degradation takes place. A similar result was reported by Kanwal *et al.* [139] when studying the effect of molecular weight during the degradation of PEO and poly (dimethylsiloxane) (PDMS). They observed that the degree of molecular degradation at a given time was proportional to the polymer molar mass. After 200 minutes of irradiation a decrease of 75% in viscosity was observed for the PDMS solution of Mw=300,000 g/mol. No significant change was observed for PEO solutions with molar masses of 10,000 and 30,000 g/mol. These observations are in good agreement with our results, where a high molecular weight PEO solution (2,000,000g/mol) showed a viscosity decrease of 98%.

For solutions loaded with magnetite nanoparticles the decrease in terminal viscosity after sonication was not as marked as that observed in the PEO solution. A reduction of 73% and 70% for the solutions loaded with 0.04% and 0.2% Fe_3O_4 was

observed. It is believed that the addition of particles may hinder polymer degradation by dissipating the shock wave created during sonication [143]. Another possible explanation for the decreased degradation is the absorption of ultrasonic energy by magnetic particle agglomerates. Magnetic nanoparticles tend to agglomerate to reduce their surface energy. This agglomeration is the consequence of their large surface to volume ratio and dipole-dipole interactions [79]. It is possible that during sonication some of the energy released is absorbed by these aggregates leading to particle dispersion.

Shear thinning was observed for both sonicated and mechanically stirred solutions. This behavior is marked by the change in slope of the viscosity against shear stress curve seen in Figure 34.

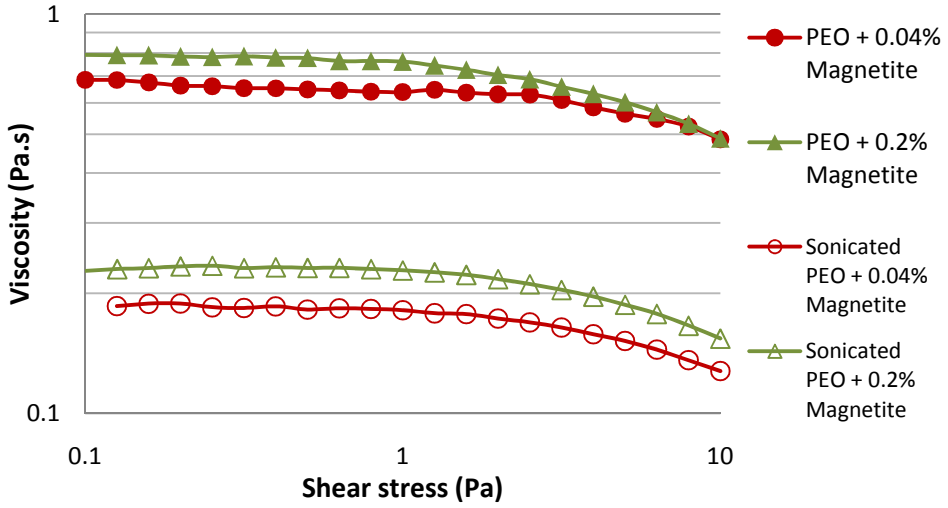

Figure 34. Shear viscosity profiles for the solutions loaded with magnetite subjected to mechanically stirring and sonication. The black arrows indicate the onset for shear thinning, which is lower for the case of sonicated solutions.

The appearance of shear thinning in sonicated solutions accounts for the presence of chain entanglements. It is well know that shear thinning is related to the disentanglement of polymer coils in solution. This effect allows for polymer

molecules to flow past each other more easily and reduces the solution viscosity [144]. Furthermore, these results showed that the shear thinning transition became smooth with sonication (Figure 34). The shape of the transition is determined by the molecular weight of the polymer solution. Abrupt transitions occur with narrow molecular weight distributions (MWD) whereas smooth transitions are related to polydisperse materials [145]. We believe that the broadening of the MWD for the sonicated solutions may be the result from the formation of different chain lengths during chain scission.

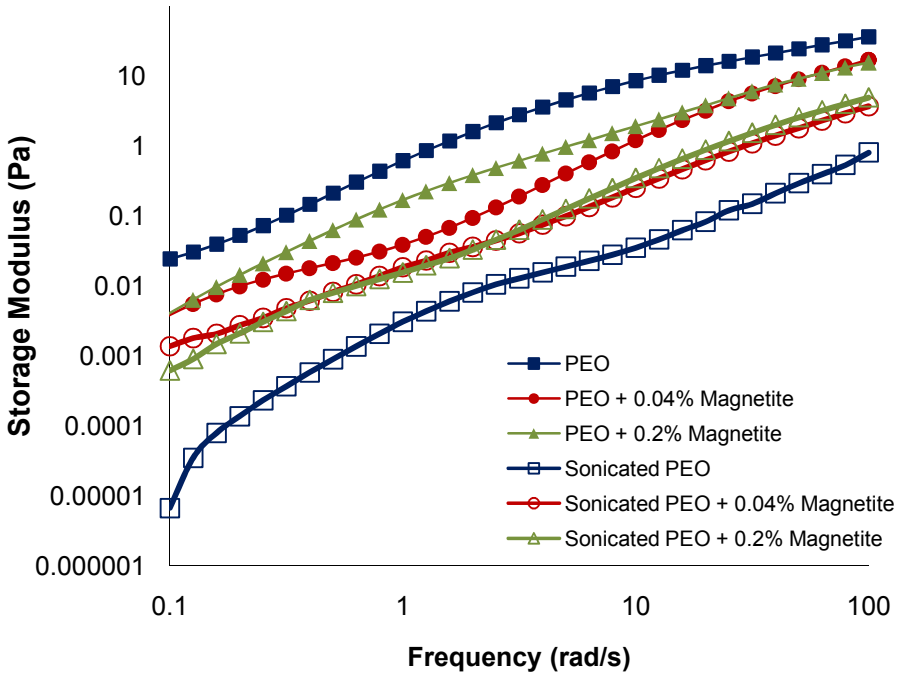

Figure 35. Effect of solution sonication on the storage modulus of the polymer solution. In the absence of magnetic nanoparticles, G' showed a decrease about three orders of magnitude.

From Figure 35 it can be seen that sonication appears to have an important effect in the storage modulus of the solutions. The storage modulus G' represents the instantaneous (elastic) response of a material when being deformed. In other words G' accounts for the solid behavior of the solution. Liquid materials tend to have low G' values since the viscous response is predominant [145]. We believe that an increase in G'

is consistent with a larger amount of chain entanglements. Chain entanglements consist of physical interlockings of chains that hinder the free mobility of individual molecules [35]. These interlockings are responsible for the solid behavior of the polymer solutions. Figure 35 shows a decrease of about three orders of magnitude for the PEO solution after sonication throughout the entire frequency range. In contrast, a small reduction was observed for the solutions loaded with magnetic nanoparticles. This leads us to believe that the reduction in the elastic response is a consequence of a decrease in the amount of chain entanglements caused by chain scission.

For solutions mechanically stirred a large decrease in viscosity was observed with the addition of magnetic particles (Figure 33). The zero shear viscosity of the pure PEO solution decreased from 3.12Pa to 0.68 and 0.79Pa with the addition of 0.04 and 0.2vol% Fe_3O_4 particles. This behavior can be attributed to the particles disrupting the formation of chain entanglements which allowed the polymer chains to flow freely. Mackay *et al*. [146] reported a decrease in complex viscosity of polystyrene (PS) melts loaded with PS nanoparticles caused by an increase in free volume. Tuteja and coworkers [147] showed that for a decrease in viscosity to take place the molecular weight of the sample has to be above a critical weight for entanglement in the confined regime. This confinement occurs when the average half interparticle gap (h) is smaller than the radius of gyration (R_g) of the molecule ($R_g/h>1$). Figure 36 shows a schematic diagram of the confinement effect for a solution in the entangled regime. The molecular configuration of the polymer changes from a random coil to an elongated molecule in order for it to diffuse between the particles.

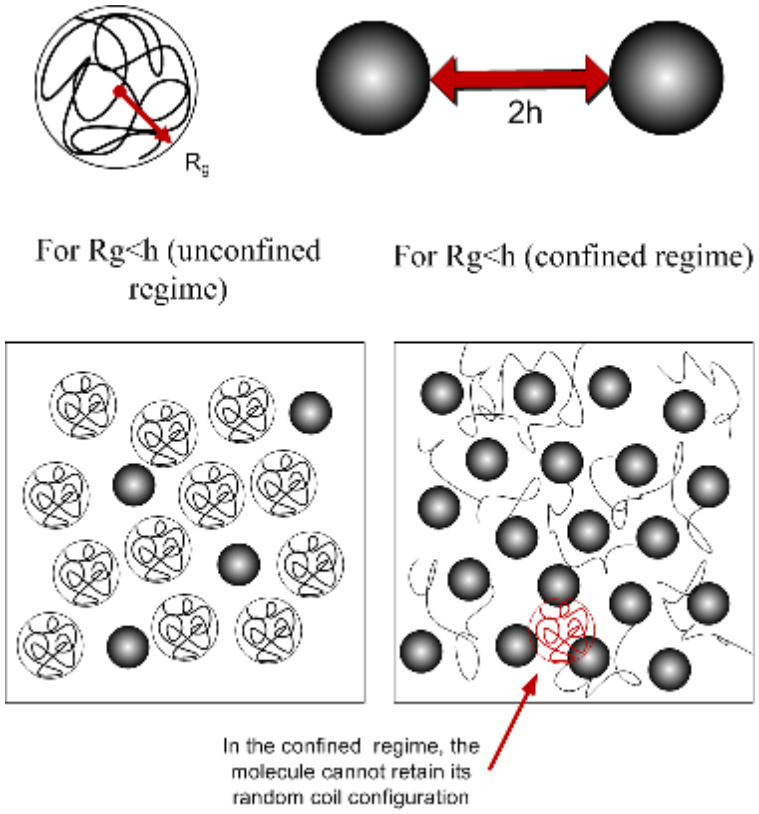

Figure 36. Schematic diagram showing the confinement effect of polymer molecules in the entangled regime. When Rg/h <1 the overlapping of polymer chains is still present. By increasing particle concentration Rg/h increases and becomes greater than one. At this point there is a change in the entanglement structure in order for the polymer molecule to diffuse between the particles.

The half interparticle gap can be calculated by a simple relation: $h/a = [\phi_m/\phi]^{1/3} - 1$ (33), where 'a' is the particle diameter, ϕ is the volumetric fraction, and ϕ_m the maximum random volumetric packing fraction (~0.638). Equation 34 was employed to calculate the critical entanglement concentration c*:

$$c^* = \frac{3M}{4\pi N_{AV} R_g^3} \qquad (34)$$

Where M is the polymer molecular weight (2,000,000g/mol) and N_{AV} the Avogadro number (6.0221418×10^{23} mol^{-1}). Devanand *et al.* [148] obtained an empirical relation for determining the radius of gyration of PEO in aqueous solution: $R_g = 0.215 M_w{}^{0.583}$ Å. A radius of gyration of 101.4nm and a critical concentration for

entanglements of 7.605 x 10^{-4} g/cm^3 where obtained for the PEO employed. The polymer concentration employed in this study was 1.92 x 10^{-2} g/cm^3. This value confirms that our solutions are in the entangled regime.

Figure 37 shows the plot of complex viscosity against frequency for the mechanically stirred solutions. A large drop in viscosity throughout the entire frequency range is observed after the addition of nanoparticles. This reduction suggests a change in the entanglement structure as predicted by Tuteja *et al.* [147]. The average half interparticle size was determined to be 92.94nm (R_g/h=1.09) and 50.74nm (R_g/h=1.99), for the 0.04 and 0.2% Fe_3O_4 solution.

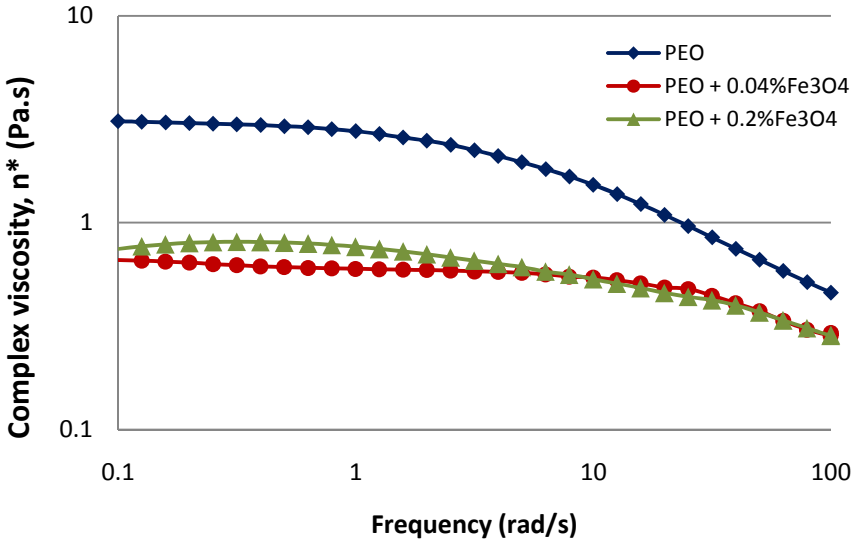

Figure 37. Effect of particle addition on the complex viscosity of a PEO solution. An overall decrease in viscosity throughout the entire frequency range indicates a change in the entanglement structure.

A decrease in terminal viscosity of 79% was achieved with the addition of 1vol% and 5vol% magnetite. Increasing the Rg/h ratio is expected to decrease the solution viscosity as a result of a larger confinement effect. This expected behavior is not observed for the solutions loaded with magnetite. At a 5% Fe_3O_4 loading (R_g/h=1.99) a similar and even higher viscosity was achieved compared to the 1% Fe_3O_4 solution (R_g/h=1.09). A larger viscosity than expected may be the consequence of particle agglomeration which results in a larger half gap than the one estimated.

Tuteja *et al.* [149] studied the rheological properties of polymer melts loaded with fullerenes and magnetite nanoparticles. Particle agglomeration lead to the absence of viscosity reduction while the viscosity decreased with a well dispersed sample. As long as a good dispersion was attained the viscosity of the melt decreased with the addition of particles.

Figure 38 shows a decrease in the elastic modulus of the sample with the addition of nanoparticles. According to Mackay *et al.* [146] confinement of linear molecules is achieved when R_g>h. This confinement results in a decrease in the amount of chain entanglements which allows for the polymer molecules to flow past each other (Figure 36). As a result of this behavior there is a reduction in the elastic response of the material. The increase in G' with increasing amount of magnetite is related to the degree of particle agglomeration.

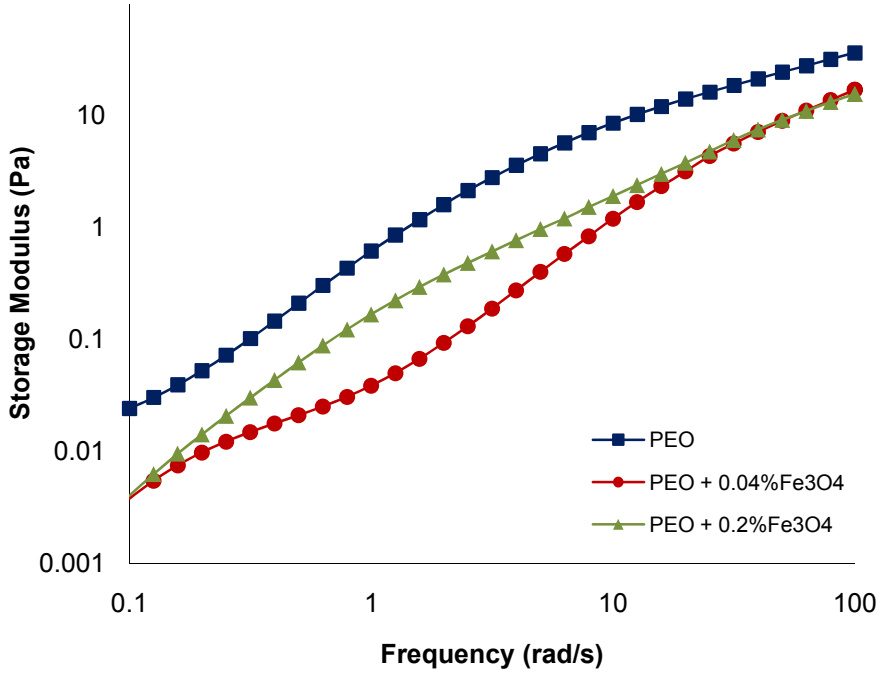

Figure 38. Storage modulus vs. frequency for solutions mechanically stirred. Note how the addition of nanoparticles decrease the G' values. This trend is evidence of disruption in the entanglement structure of the solution.

4.2 Effect of Solution Properties and Processing Parameters on the Electrospinning of Magnetic Nanofibers

4.2.1 Development of the Whipping Instability

High speed imaging was used to observe the evolution of the jet at the exit of the capillary. These images allowed us to make an assessment of the role that solution parameters play in the electrospinning of solutions loaded with magnetic nanoparticles. In addition to both magnetite solutions, a solution composed of 0.04vol% $CoFe_2O_4$ was prepared. A pure PEO solution was employed as a control. All solutions where mechanically stirred to avoid polymer degradation. Figure 39 shows the path of the electrified jet at the exit of the capillary for a set of solutions spun at 0.9mL/hr and 60kV/m.

At a given volumetric flow, the electric field was varied from 20 to 100kV/m in steps of 20kV. For all solutions, at an applied field of 40kV/m a polymer jet emanated from the tip of the capillary. From Figure 39 it is evident that solution properties play an important role in determining the distance for the onset of this transition. The bending instability was clearly observed for the 0.04%Fe_3O_4 solution whereas for the 0.2%Fe_3O_4 solution the jet begins to bend close to the exit of the frame. For both the PEO and $CoFe_2O_4$ solutions the transition occurred outside of the camera vision frame.

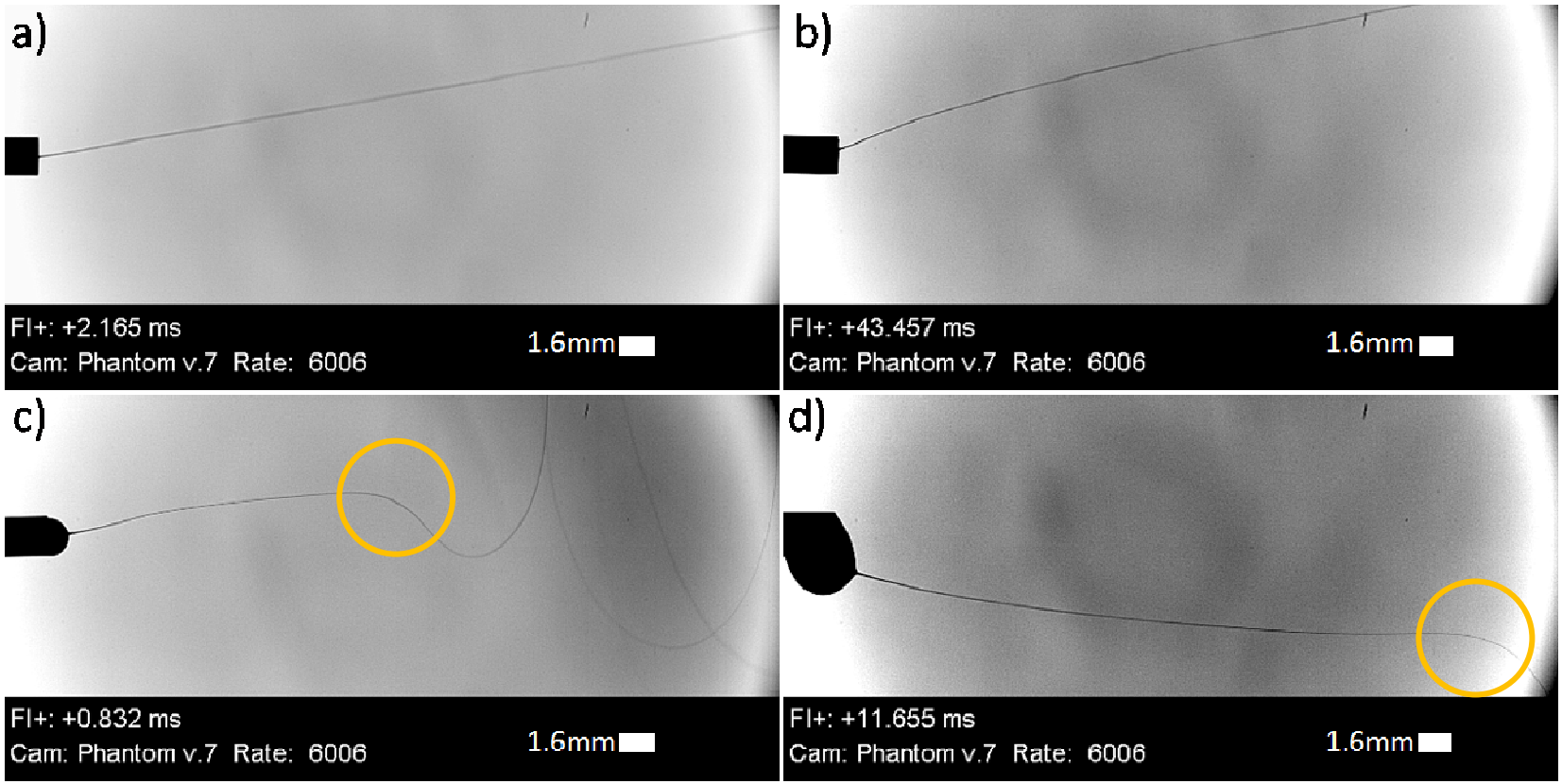

Figure 39. Images of an electrified jet electrospun at 0.9mL/hr and 60kV/m for our different solutions: a) PEO/H_2O, b) PEO + 0.04vol%$CoFe_2O_4$, c) PEO + 0.04vol% Fe_3O_4, d) PEO + 0.2vol% Fe_3O_4. The development of the whipping instability is clear when electrospinning a solution loaded with 0.04%Fe_3O_4.

A theory for the development of the bending instability was initially proposed by Reneker *et al.* [20]. During the flight of an electrified jet the electrical charges can be regarded as a static system interacting by Coulomb's law. This system is known to be unstable according to the Earnshaw's theorem (illustrated in Figure 40). Three charges (A, B, C) of equal magnitude and sign are considered to be in a straight line. If a small perturbation causes B to move of the line by a small distance δ, the interaction with neighboring charges (A, C) will create a net force F_1. This net force will cause B to move further in the direction of the perturbation.

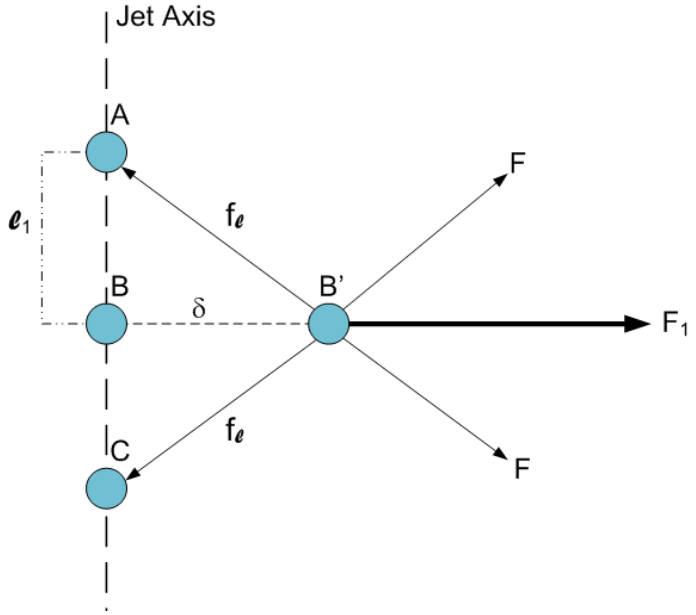

Figure 40. Illustration of the Earnshaw instability leading to bending of an electrified jet. Adapted from (20).

When charges A, B, and C are attached to a liquid viscoelastic forces f_l tend to counteract the development of the instability caused by Coulombic forces. In order for the perturbation to grow, the net force (F) exerted on B must overcome the viscoelastic resistance of the jet. As soon as F overcomes f_l the perturbation begins to grow at a rate decelerated by f_l.

From Figure 39-a and 39-c it is clear that when adding 0.04% Fe_3O_4 to our PEO solution the onset of the whipping instability shifted closer to the tip of the capillary. The transition for the pure PEO solution occurred outside of the camera range of vision preventing us from calculating the exact reduction. From Table 2 it can be observed the effect that the addition of particles had on the conductivity of the solution.

Table 2. Solution Properties.

Magnetic Material	Magnetic Content (vol%)	Zero-Shear Viscosity [Pa.s]	Conductivity [mS/cm]	Surface Tension [mN/m]
PEO	0	3.12	0.068	62.72
$CoFe_2O_4$	0.04%	1.53	0.373	60.65
Fe_3O_4	0.04%	0.68	0.521	60.35
Fe_3O_4	0.2%	0.79	1.966	58.85

The addition of 0.04%Fe_3O_4 to the PEO solution drastically increased its conductivity from 68 to 520μS/cm. It is feasible that at higher conductivities the proximity of charges within the jet may increase. This increase in proximity enhances the force caused by Coulombic repulsion. As a result, the onset of the whipping instability occurs closer to the capillary since the viscoelastic forces are not large enough to counteract the Coulombic force. The effect of conductivity on the development of the whipping instability was also reported by Qin *et al.* [42]. They showed how the straight path of the jet decreased with increasing concentration of LiCl in polyacrilonitrile solutions.

If the distance for the onset of the instability depended only on solution conductivity the smallest elongation should be observed for the solution loaded with 0.2% Fe_3O_4. Instead, for all field/flow combinations, the smallest elongation was

achieved with the solution loaded with 0.04%Fe_3O_4. This behavior demonstrates the role that rheological properties may play in counteracting the development of this instability. Among the four solutions the lowest viscosity was achieved with 0.04%Fe_3O_4. By lowering the solution viscosity the jet's viscoelastic resistance to deformation also decreases. This decrease will result in the development of the onset of the whipping instability closer to the tip of the capillary. When comparing Figure 39-c and 39-d the effect of viscosity on the straight path of the jet can be seen. The stable segment was calculated to be 15.87mm and 26.57mm, respectively.

A similar behavior was reported by Eda *et al.* [44] when studying the effect of rheological properties in the electrospinning of polystyrene solutions. They observed how an increase in molecular weight for a fixed [η]c caused the bending instability to occur further away from the tip of the capillary. An example of their results is shown in Figure 41. The straight path was approximated as 5.18mm and 9.24mm from Figure 41-a and 41-b.

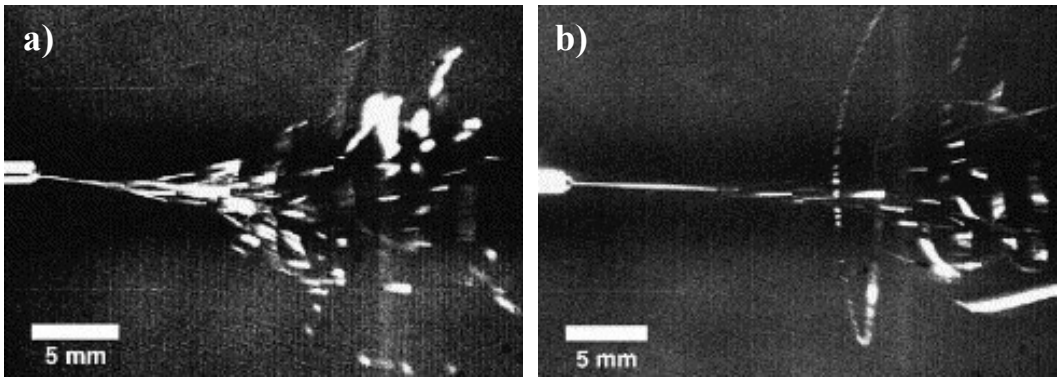

Figure 41. Effect of increasing molecular weight on the onset of the whipping instability. The parameters for each solution were: a) Mw=44,100g/mol, [η]c=9; b) Mw=1,877,000g/mol, [η]c=9. The straight path of the jet was calculated to be a) 5.18mm and b) 9.18mm[44].

Due to our recording setup it was not possible to capture the onset of the whipping instability for both PEO and $CoFe_2O_4$ solutions. For these solutions the whipping instability occurred outside of the camera range of vision. However, this is

consistent with both solutions having higher viscosities and lower conductivities than the both loaded with magnetite. For the solution loaded with 0.2%Fe_3O_4 the whipping instability was visible in Figure 39. With the remaining field/flow combinations, the transition also occurred outside of the camera range of vision. At all times the whipping instability was only visible with the solution loaded with 0.04%Fe_3O_4.

For the solution loaded with 0.04%Fe_3O_4, increasing the electric field at a constant volumetric flow also increased the initial elongation of the jet. This behavior can be seen in the high speed micrographs shown in Figure 42.

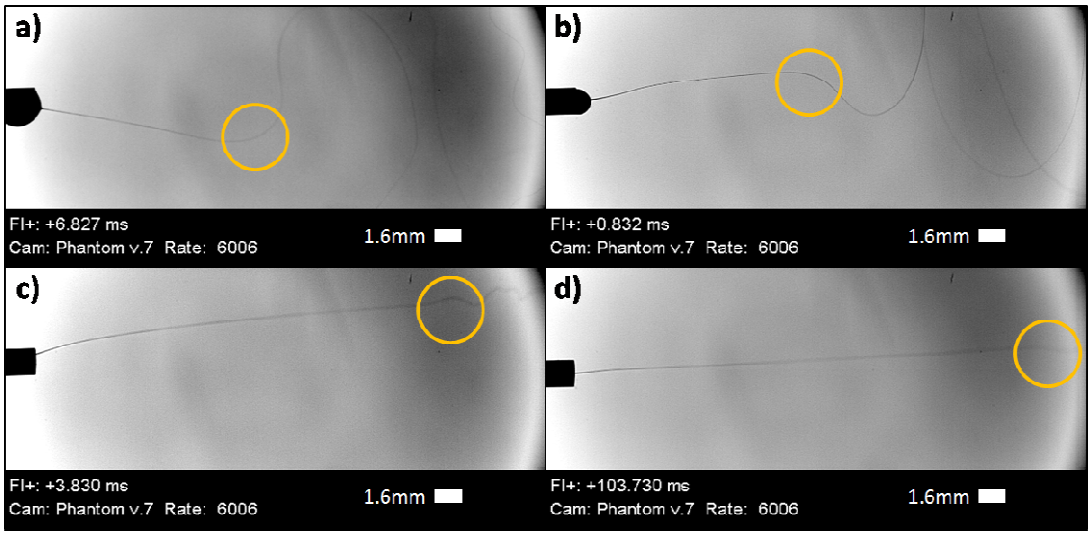

Figure 42. Electrospinning of a 4vol%PEO/H_2O solution loaded with 0.04vol% Fe_3O_4 at 0.9mL/hr under an electric field of a) 40kV/m, b) 60kV/m, c) 80kV/m, d) 100kV/m. The distance for the onset of the whipping instability is a) 11.069mm b) 13.035mm c) 24.503mm d) 28.4mm.

e believe that the change in the onset of the whipping instability is related to the velocity at which the jet is expelled. Charges move within a solution at a speed determined by the drift velocity v_{dx}:

$$v_{dx} = \mu_d E_x \qquad (35)$$

Where μ_d is the drift mobility and E_x the electric field in the direction parallel to the axis of the jet [69]. The mobility of ions in polymer solutions has been estimated to be

10^{-6} m^2/V s [20]. Increasing the electric field increases the velocity at which charges are able to move within the polymer solution, hence the velocity at which the jet is expelled from the tip of the capillary. A larger elongation is obtained with increasing electric fields since the jet has traveled a longer distance before it thins and starts to bend.

The effect of applied voltage and volumetric flow on the distance for the onset of the bending instability is seen in Figure 43 for the solution loaded with 0.04%Fe_3O_4. For the different volumetric flows, the straight path of the jet increases with increasing voltage. This behavior was also predicted by a mathematical model developed by Reneker *et al*. [20]. In this model the bending instability was modeled by a system of beads connected by viscoelastic elements (springs and dashpots). Under an electric field the beads interacted with each other according to Coulomb's law. The springs and dashpots used in the model mimicked Maxwell's viscoelastic resistance to the elongation of the jet. The effect of surface tension and evaporation was also taken into account. Equations of motion in the beads with the external forces acting in combination where used to numerically follow the evolution of the electrified jet. These results were in reasonable agreement with the experimental results reported in the same study.

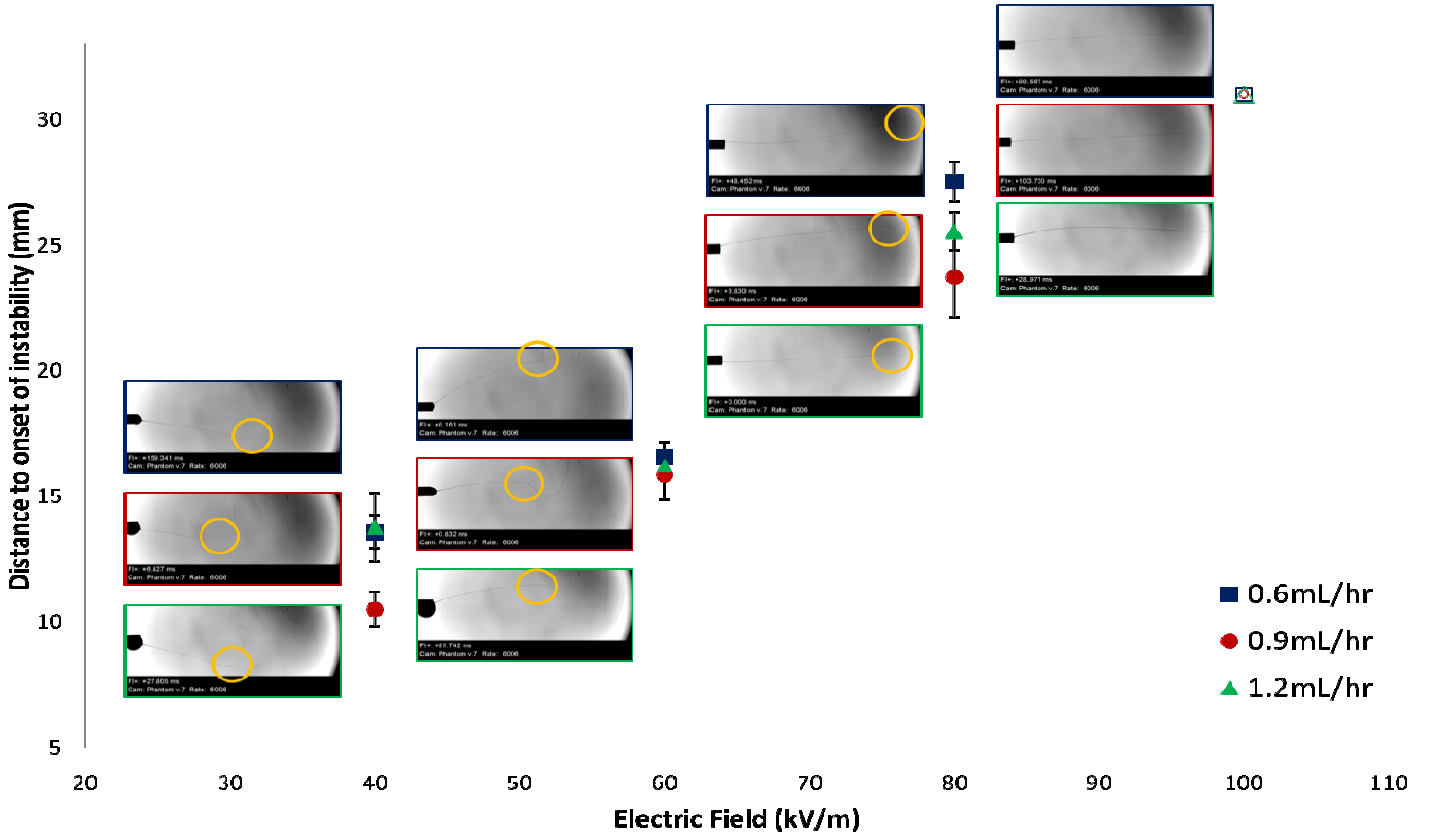

Figure 43. Effect of increasing the electric field on the distance for the onset of the whipping instability. Larger electric fields result in an increase in the initial straight path of the jet. The effect of the volumetric flow cannot be resolved from this image. Next to each data point is its corresponding high speed micrograph. The color of the image frame corresponds to the volumetric flow color indicated in the legend of the figure. The unfilled symbols represent the data points that were outside of the camera range of vision.

4.2.2 Fiber Size and Morphology

SEM and FESEM imaging was used to assess the effect of the solution's properties and processing parameters on the size and morphology of resulting fibers. Figure 44 shows a set of SEM micrographs for the different solutions spun at 1.2mL/hr and 15kV.

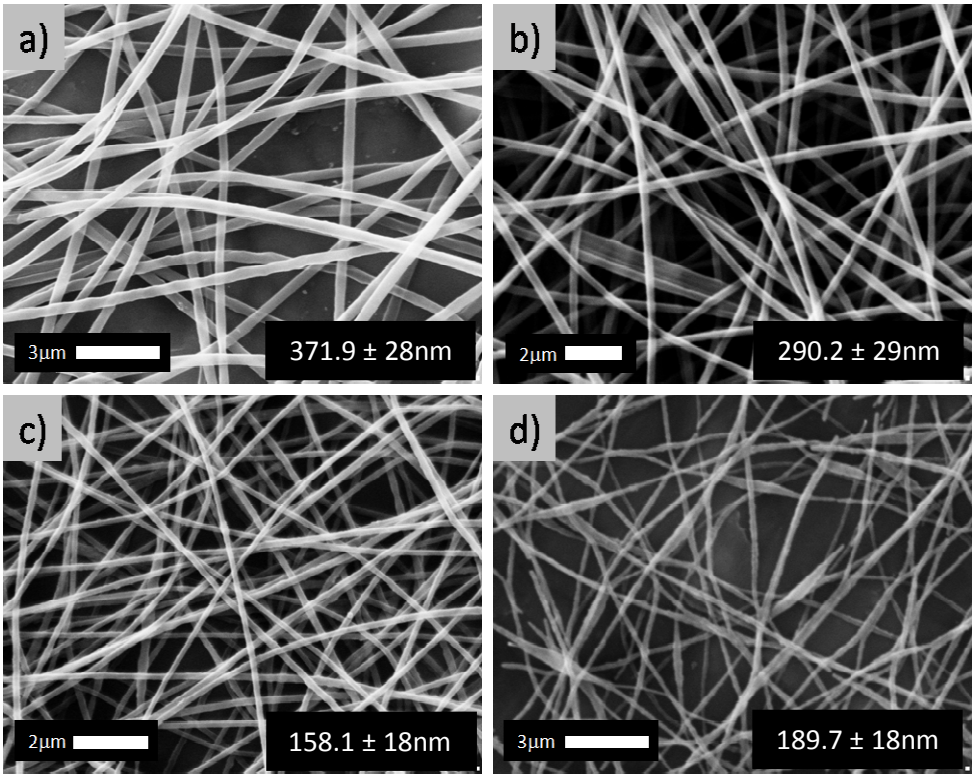

Figure 44. SEM micrographs of electrospun fibers at 1.2mL/hr and 15kV for the different solutions: a) PEO; b) PEO + 0.04%$CoFe_2O_4$; c) PEO + 0.04%Fe_3O_4; d) PEO + 0.2%Fe_3O_4.

As seen in Figure 44 the addition of nanoparticles appears to have an effect on the morphology and size of the electrospun fibers. Smooth, straight fibers where obtained when pure PEO and $CoFe_2O_4$ loaded solutions where electrospun. On the other hand, when electrospinning solutions loaded with magnetite bumps could be seen in the resulting fibers. The resulting fibers were further analyzed with FESEM. This technique allowed us to examine the morphology of the resulting fibers with greater detail (Figure 45).

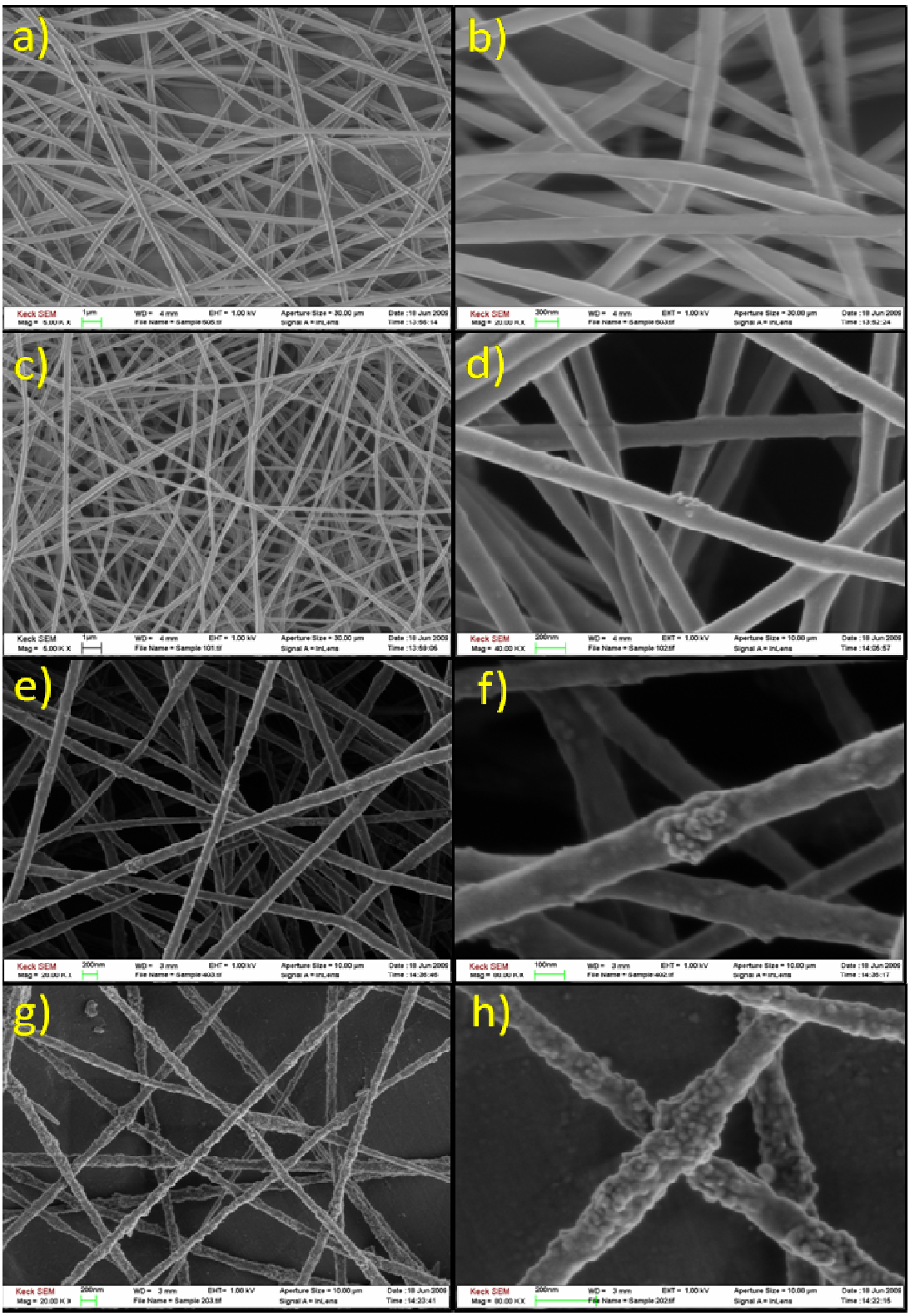

Figure 45. FESEM micrographs showing the effect of particle loading on the morphology of the fibers electrospun from the following solutions: a,b) PEO; c,d) PEO + 0.04%$CoFe_2O_4$; e,f) PEO + 0.04%Fe_3O_4; g,h) PEO + 0.2%Fe_3O_4.

Surface roughness of fibers electrospun from the 0.04%Fe_3O_4 solution was greater than that observed on the fibers obtained from the 0.04%$CoFe_2O_4$ solution. These irregularities increase with increasing magnetite content, which may be the result of particle agglomeration within the polymer matrix. TEM allowed us to assess particle dispersion within the resulting fibers. The resulting micrographs are shown in Figure 46.

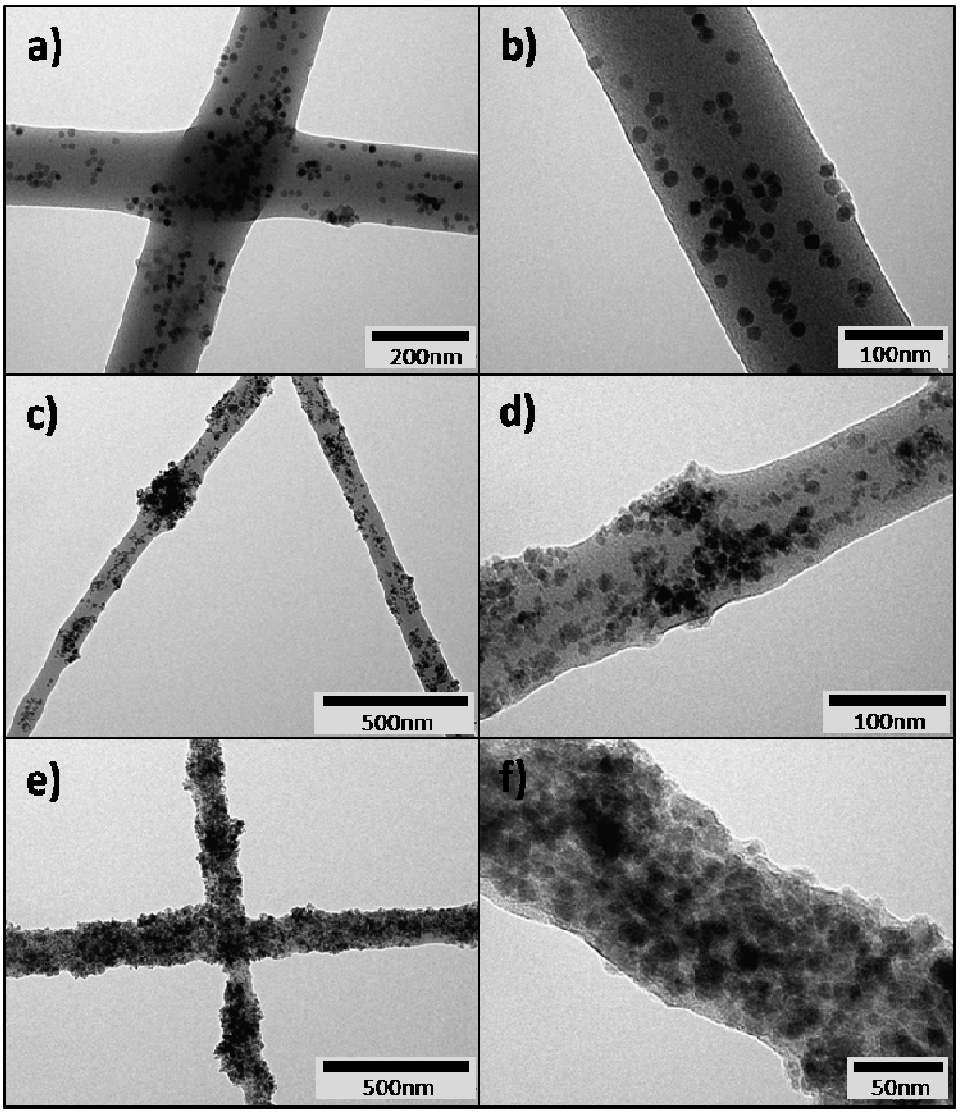

Figure 46. TEM micrographs showing particle dispersion within the polymer matrix. The fibers where electrospun from a PEO solution loaded with: a,b) 0.04%$CoFe_2O_4$; c,d) 0.04%Fe_3O_4; e,f) 0.2%Fe_3O_4. From these images, it is evident that a larger degree of agglomeration is obtained with the magnetite nanoparticles when comparing b) and d).

As seen from Figure 46-A, good particle dispersion was achieved in fibers loaded with cobalt ferrite. A larger degree of agglomeration was observed when electrospinning fibers from magnetite solutions (shown in Figure 46-B and 46-C). These agglomerates may account for the surface roughness seen in the FESEM images.

Particles tend to agglomerate to reduce their surface energy. This agglomeration can be counteracted by capping their surface with a surfactant. Cobalt ferrite nanoparticles where capped with polyethylene glycol (PEG) which allowed for their better dispersion. The poor dispersion of magnetite nanoparticles may be the result of a lack of compatibility between the particle surfactant and the polymer matrix. Fibers spun from a solution loaded with 0.2vol% magnetite appear to be about to reach saturation. Overall, for the solution containing 0.2%Fe_3O_4 continuous fibers were produced with minor fiber breakage (Figure 44-d).

Solution properties play a significant role during electrospinning. It has been reported that solutions with high conductivity and low viscosities promote the formation of small diameter fibers [29, 30, 34, 38]. Figure 47 shows the effect of solution viscosity on the resulting average fiber diameter.

Table 3. Solution Properties.

Solution	Viscosity [Pa.s]	Conductivity [mS/cm]
PEO + 0.04%Fe_3O_4	0.68	0.521
PEO + 0.2%Fe_3O_4	0.79	1.966
PEO + 0.04%CoFe2O4	1.53	0.373
PEO	3.12	0.068

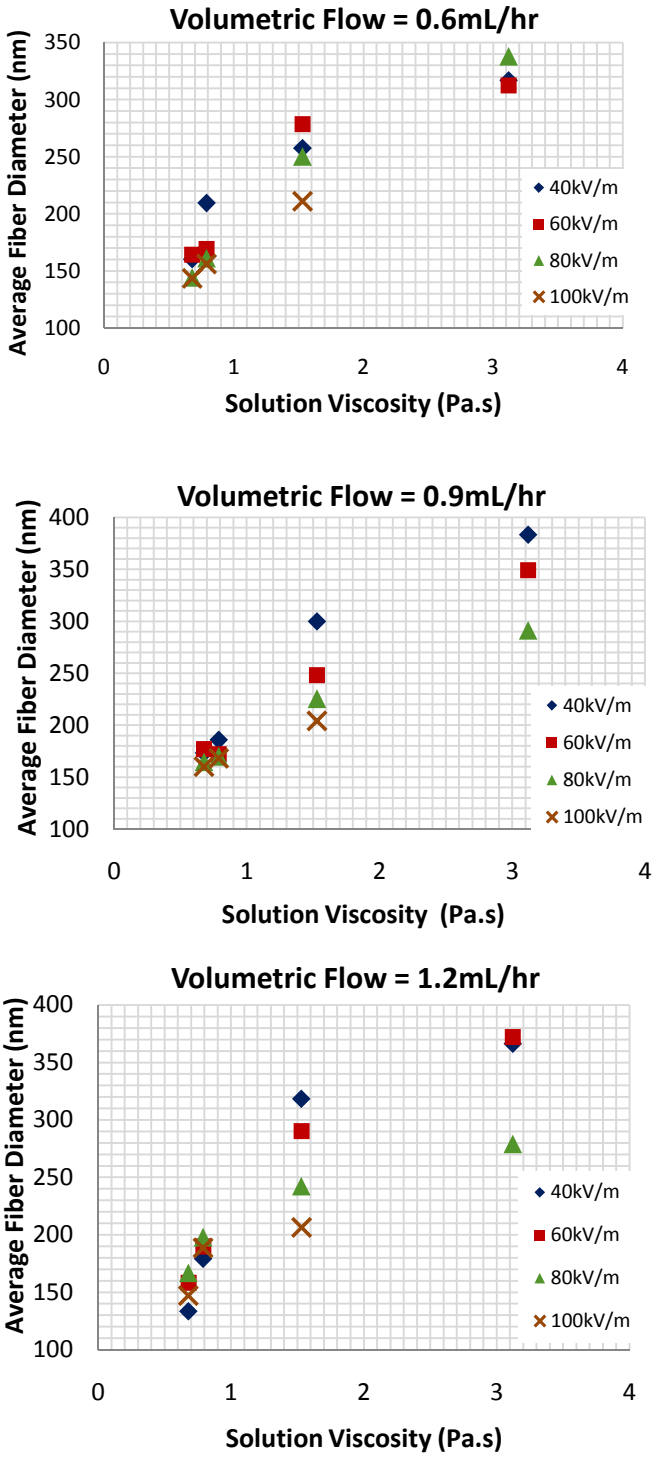

Figure 47 Effect of solution viscosity in the resulting fiber diameter. The viscosity of the different solutions is 3.12Pa.s for pure PEO, 1.53Pa.s for 0.04%$CoFe_2O_4$, 0.79 Pa.s for 0.04%Fe_3O_4, and 0.68Pa.s for 0.2%Fe_3O_4. Increasing diameter with increasing viscosity appears to be the general trend of this graph.

Figure 47 shows a trend where increasing solution viscosity results in larger diameter fibers. The smallest fiber diameters were obtained with the solution loaded with 0.04% Fe_3O_4. This solution had the lowest viscosity and showed the smallest initial elongation at each field/flow combination. We believe that the effect of solution viscosity on the final fiber diameter may be related to two main reasons. Increasing the solution viscosity increases both the viscoelastic resistance and the straight path of the jet. By increasing the straight path the amount of time the jet whips while travelling towards the collector decreases. A reduction in the whipping time results in larger fiber diameters due to a decrease in the jet draw ratio. The second reason is related to the amplitude of the bending perturbation. This amplitude is counteracted by increasing the viscoelastic resistance which in turn decreases the draw ratio of the jet [20].

These results are in good agreement with those reported by Uyar *et al.* [150]. In their work the smallest fiber diameters where obtained when electrospinning PS solutions with low viscosity. The same trend between viscosity and the resulting fiber diameter has been reported by several authors [5, 34, 35]. Further experiments need to be performed with a wider camera range of vision in order to determine the onset of the whipping instability for the remaining solutions.

The effect that conductivity plays on the resulting fiber diameter could not be fully understood from these results. Wang *et al.* [31] and You *et al.* [19] reported a decrease in the final fiber diameter when increasing solution conductivity. This increase can be attributed to an increase in charge density as the solvent evaporates which enhances the charge repulsion within the jet [39]. In this study the solution with the largest conductivity (0.2%Fe_3O_4) did not show the smallest fiber diameter; the one with the lowest viscosity did. This observation further confirms the key role that viscosity has on the resulting fiber diameter, which has also been corroborated by Wang *et al.* [31].

A clear relationship between the applied voltage, volumetric flow, and resulting fiber diameter, could not be resolved from the previous graphs. In order to see if there is a significant effect of these parameters, a statistical analysis was performed to our data.

4.2.2.1 Statistical Analysis

The significance of processing parameters and solution properties on the average diameter of the resulting nanofibers were investigated using statistical analysis. Statistical regression analyses with different predictor combinations were performed until the best fit was obtained. The goodness of fit is given by R^2 for which a value of unity indicates a perfect fit. A p-value threshold of 0.05 was used to assess the significance of the results. This value indicates that the probability of falsely accepting the estimated coefficients to be different than zero will be less than 5%. P-values lower than 0.05 indicate significant factors where the lower this value the greater the predictor significance. The statistical analysis was performed using the JMP statistical software.

During the initial screening four numerical predictors were employed: volumetric flow (X_1), electric field (X_2), conductivity (X_3), and viscosity (X_4). The relation between the average fiber diameter (Y) and the four predictors was approximated by a first order polynomial equation as follows:

$$Y = \beta_0 + \beta_1 X_1 + \beta_2 X_2 + \beta_3 X_3 + \beta_4 X_4 + \beta_5 X_5 \qquad (36)$$

Where the unknown coefficients were calculated using the least squares method with JMP.

Table 4. Statistics for initial fit.

Term	Estimate	p-value
Intercept	β_0= 160.28±50.81	1.40E-07
X_1 - Volumetric Flow (mL/hr)	β_1= 15.62±34.85	0.370513
X_2 – Electric Field (kV/m)	β_2= -0.67±0.40	2.49E-14
X_3 - Conductivity (mS/cm)	β_3= -0.97±14.55	0.893572
X_4 – Viscosity (Pa.s)	β_4= 67.66±11.83	1.66E-03

$R^2 = 0.860$

Table 4 summarizes the statistics obtained in the first fit. The second column shows the value of the unknown coefficients in the polynomial equation. An R^2 value of 0.860 was obtained indicating that the model explains 86% of the variability in the response. From the obtained p-values, volumetric flow and solution conductivity (p-value > 0.05) do not have a significant effect on the resulting fiber diameters. The following equation is obtained when considering only the significant parameters:

$$F.Diameter(nm) = 172.88 - 0.67\,[E.Field\ (kV/m)] - 68.13[Viscosity\ (Pa.s)] \quad (37)$$

This model indicates how a unit increase in viscosity at a constant voltage increases the final fiber diameter by 68 units. The negative sign in the slope of the electric field predictor indicates that a unit increase in the electric field decreases the final diameter by 0.67 units. These results are in close agreement with those reported by Wang *et al*. [31] where an increase in the electric field slightly decreased the final diameter of the fibers. Wang and coworkers attributed this behavior to an increase of charges in the jet surface which induced a greater repulsive force during the bending instability. Ojha *et al*. [12] reported an increase in the final fiber diameter of Nylon6 with increasing voltage as a consequence of more solution drawn from the capillary.

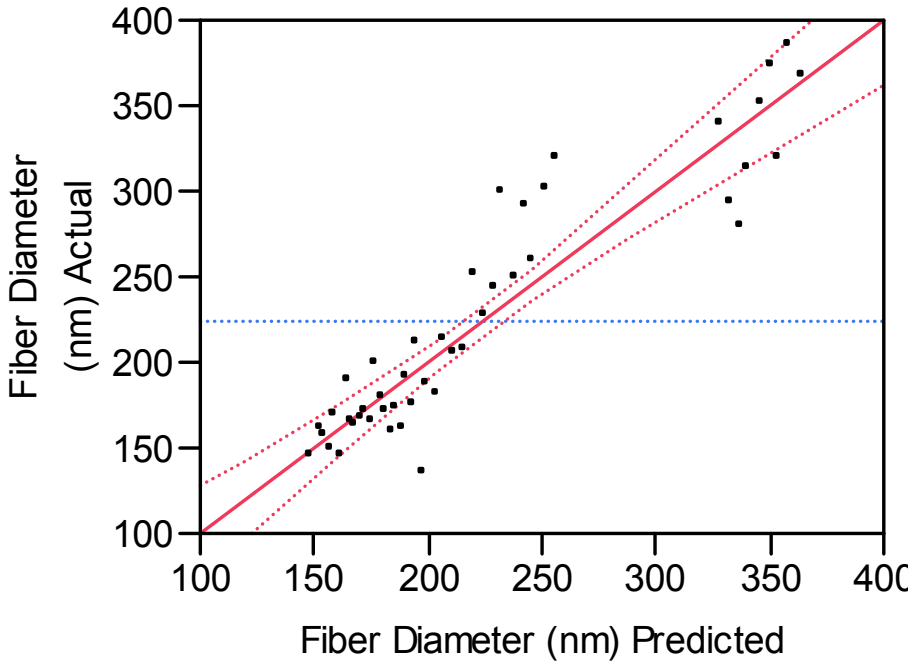

Figure 48. Actual diameter data against predicted values from the following model: *F.Diameter(nm) = 160.28 – 0.67[E.Field(kV/m)] + 68.13[Viscosity(Pa.s)]*. The R^2 value for this model was 0.857.

Figure 48 shows the measured diameter data against the values predicted by Equation 37. The majority of points lay within the 95% confidence interval given by the dashed red lines.

To improve the R^2 value we fitted a different model taking into account interaction parameters. Possible interactions during the electrospinning include: ElecField-Conductivity, ElecField-Volumetric Flow, Volumetric Flow-Viscosity, ElecField-Viscosity, and ElecField-Volumetric Flow-Viscosity. Following the same nomenclature as before, the proposed model is given by the following equation:

$$Y = \beta_0 + \beta_1 X_1 + \beta_2 X_2 + \beta_3 X_3 + \beta_4 X_4 + \beta_5 X_1 X_2 + \beta_6 X_1 X_4 + \beta_7 X_2 X_3 + \beta_8 X_2 X_4 + \beta_9 X_1 X_2 X_3 + \beta_{10} X_1 X_2 X_4 + \beta_{11} X_1 X_2 X_3 X_4 \qquad (38)$$

Table 5. Statistics for fit taking into account interaction terms.

Term	Estimate	p-value
Intercept	174.701	4.36e-8
X_1 - Volumetric Flow (mL/hr)	8.1222	0.6354
X_2 - Electric Field (kV/m)	-0.7358	0.0006
X_3 - Conductivity (mS/cm)	-1.8003	0.7967
X_4 - Viscosity (Pa.s)	64.9998	9.04e-13
$(X_1-0.9)*(X_2-68)$	-1.6562	0.5779
$(X_1-0.9)*(X_4-1.424)$	-5.2985	0.7880
$(X_2-68)*(X_3-0.776)$	0.1711	0.5840
$(X_2-68)*(X_4-1.424)$	-0.3379	0.2549
$(X_1-0.9)*(X_2-68)*(X_3-0.776)$	-0.9109	0.8571
$(X_1-0.9)*(X_2-68)*(X_4-1.424)$	-3.8642	0.4533
$(X_1-0.9)*(X_2-68)*(X_3-0.776)*(X_4-1.424)$	-2.7037	0.7127

$R^2 = 0.894$

The different predictors are centered by their mean when they are crossed with other factors to create an interaction term. The R^2 value for this model increased by 3% from the one with no interaction terms. However, none of the interaction parameters have a significant effect on the resulting fiber diameter. We can conclude that Equation 37 is the best option to describe the behavior of our system. The parameter with the largest influence in determining the size of the resulting fibers is solution viscosity. Similar results were reported by Cui *et al.* [11] when performing an orthogonal analysis to the electrospinning of PLA. Cuo and coworkers found that solution concentration and polymer molecular weight were the most significant factors that influenced the fiber diameter.

4.2.3 Magnetic Properties of Composite Fibers and their Precursor Solution

Table 6 shows the magnetization of the three different solutions and a bundle of fibers electrospun from each.

Table 6. Room temperature equilibrium magnetization of a bundle of PEO fibers and their precursor solution.

	Precursor solution	Bundle of fibers
0.04%Fe_3O_4	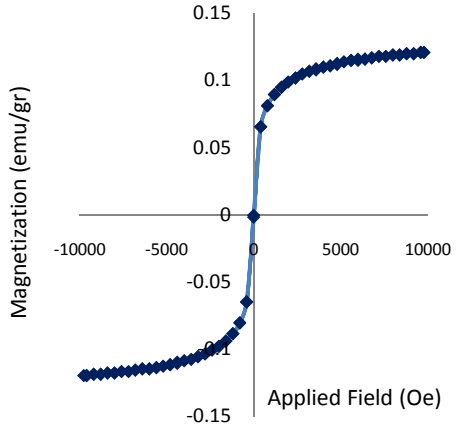	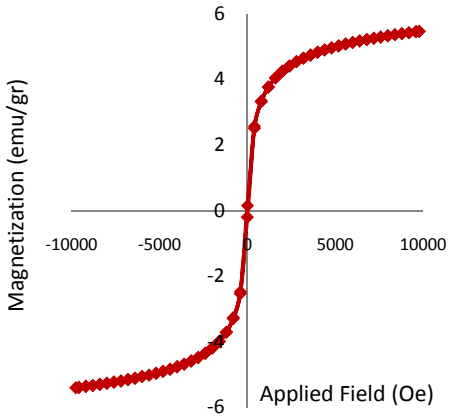
0.2%Fe_3O_4	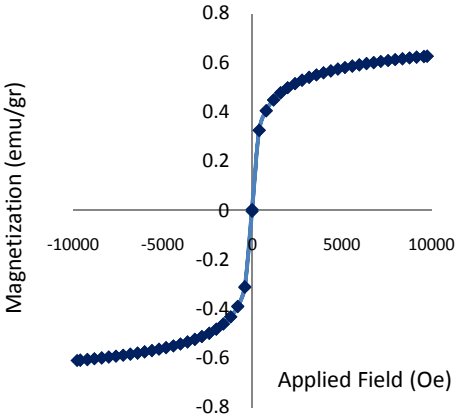	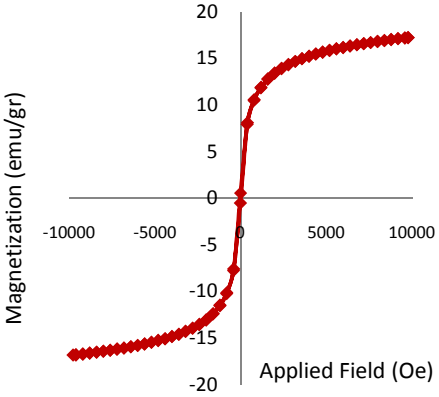
0.04%$CoFe_2O_4$	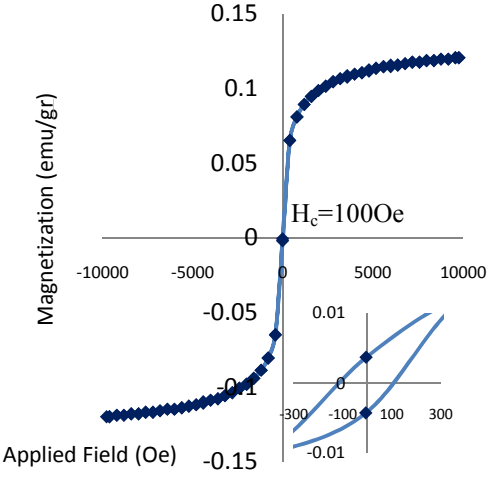	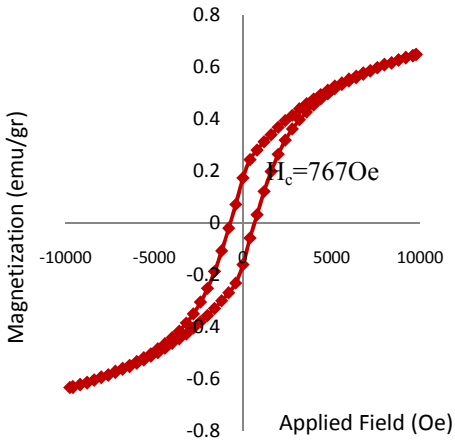

From Table 6 we can see that the resulting fibers show the same magnetic behavior as their precursor solution. A superparamagnetic behavior was seen in fibers electrospun from 0.04 and 0.2% Fe_3O_4 solution. These solutions showed the same superparamagnetic behavior as the fibers. This behavior is characterized by a zero remanescence and coercive field. With a Langevin analysis we can corroborate the particle diameters obtained with TEM. From the lowest applied field values, the initial susceptibility was calculated. This value allowed us to calculate the upper range in particle size (Equation 39). The lower value for the diameter range was obtained from the asymptotic solution of the Langevin equation (Equation 40). The asymptotic solution also permitted us to verify the volumetric fraction of particles in solution. These two values were obtained by graphing **M** against **1/H**. The intercept corresponds to ϕM_d while the slope equals: $6\phi kT/\pi\mu_0 d^3$. This analysis could not be performed to the cobalt ferrite solution since it requires solutions with superparamagnetic behavior. Table 7 summarizes the results of the Langevin analysis.

$$M = \chi_i H; \qquad \chi_i = \frac{\pi}{18}\phi\mu_0\frac{M_d^2 d^3}{kT} \qquad (39)$$

$$M = \phi M_d\left(1 - \frac{6}{\pi}\frac{kT}{\mu_0 M_d H d^3}\right) \qquad (40)$$

Table 7. Results of the Langevin analysis on the PEO solutions loaded with 0.04 and 0.2%Fe_3O_4.

Solution	Volumetric fraction (theoretical)	Domain Magnetization M_d (kA/m)	Volumetric fraction (VSM)	Initial Susceptibility χ_i
0.04%Fe_3O_4	0.0004	446	0.00029	0.002
0.2%Fe_3O_4	0.002	446	0.0015	0.01

Solution	Diameter from χ_i (nm)	Slope asymptotic solution	Diameter from asymptotic solution (nm)
0.04%Fe_3O_4	8.66	$6x10^6$	6.71
0.2%Fe_3O_4	8.56	$4x10^7$	6.17

	Diameter range measured with TEM	Diameter range calculated from a Langevin analysis
Fe_3O_4	4nm – 16nm	6.44nm – 8.61nm

The volume fraction of particles calculated from the Langevin analysis is slightly lower than the one calculated theoretically. This discrepancy could be related to particle settlement prior to their dispersion in the polymer matrix. There is a notorious difference in the particle size range between the one measured with TEM and the one calculated with the Langevin analysis. A lower value in the upper size range was obtained from the Langevin calculation. This decrease may be related to the particle dead layer and surfactant coating since this analysis calculates the magnetic diameter. On the other hand, a larger size for the lower range was obtained with the Langevin analysis. This increase may be the consequence of poor dispersion and agglomeration of particles in the polymer solution [4].

The saturation magnetization of the 0.04%Fe3O4 solution and resulting fibers was 0.121 and 5.47emu/cm^3 whereas for both the 0.2%Fe_3O_4 solution and electrospun fibers was 0.63 and 17.2emu/cm^3. These values depend on the concentration of particles in the sample which was larger for the composite nanofibers due to evaporation. The production of magnetite fiber composites has been previously reported by several authors [4, 37] and the same superparamagnetic behavior was observed.

Both the solution and the electrospun fibers loaded with cobalt ferrite exhibited a ferromagnetic behavior. A low coercive field was observed for the cobalt ferrite solution. This reduction is related to the particles being suspended in a liquid carrier during the magnetic measurements. Since the particles are not fixed in a solid matrix they are able to rotate for them to align their magnetic moments with their external field. In the experiments carried by McTague [7] the cobalt ferrite nanoparticles were suspended in water. This resulted in a superparamagnetic solution, for which the Langevin analysis could be applied.

4.3 Magnetoviscous Effect during the Electrospinning Process

When applying a static magnetic field during the flow of solutions loaded with magnetic particles an increase in the fluid's viscosity is expected. This field was applied to the capillary just before the exit of the electrospun jet. Based on the work by

McTague [7], the magnetic field was placed parallel to the direction of flow to achieve a larger effect.

To calculate the theoretical increase in viscosity we must first calculate the magnitude of the Langevin parameter ξ. This parameter can be obtained from the VSM results using the asymptotic solution of the Langevin equation:

$$\xi = \frac{1}{1-{}^{M}/_{\phi M_d}} \qquad (41)$$

The Langevin equation was initially derived for dilute superparamagnetic ferrofluids where particle interaction may be neglected. Both of these requirements are achieved with our magnetite solutions (Table 6). From the VSM results the magnetization value at an applied field of 3725Oe was obtained. This value corresponds to $1.08x10^{-1}$ and $5.51x10^{-1}$emu/cm^3 (108 and 551 A/m) for the solution loaded with 0.04 and 0.2% Fe_3O_4. The Langevin parameter was estimated to be 6.06 and 5.67, respectively. This value was calculated using the volumetric fractions calculated from the VSM measurements. This analysis cannot be performed to the $CoFe_2O_4$ solution since it deviates from the theoretical assumptions. Table 8 summarizes these results.

Table 8. Magnetic properties of the different solutions.

Solution	Domain Magnetization (kA/m)	Magnetization at 3725Ga (A/m)	Langevin Parameter, ξ
0.04%Fe_3O_4	446	108	6.06
0.2%Fe_3O_4	446	551	5.67

The Langevin parameter is larger than unity for both solutions. With these results the increase in viscosity was calculated using the following equation [8]:

$$\Delta\eta = \frac{3}{2}\eta\varphi \qquad (42)$$

Where $\Delta\eta$ is the increase in viscosity, η the terminal viscosity of the fluid, and φ the volume fraction of particles in solution. Equation 42 predicts a $\Delta\eta$ of 0.0003Pa.s and 0.002Pa.s (0.044 and 0.253%) for the solutions loaded with 0.04 and 0.2% Fe_3O_4. From these results there appears to be a small effect on the viscosity of the solutions when applying a static field. Even though this theory was intended for diluted ferrofluids, the concentration employed in the solutions is not high enough to have a significant increase.

This theory has been corroborated experimentally by several authors. McTague reported an increase of 4.81% in the viscosity of a suspension of 6.6vol% $CoFe_2O_4$ with an applied field of 1,100Ga. The same dependence was observed for a commercial ferrofluid composed of 7.2vol% magnetite particles [131].

High speed imaging was employed to study the behavior of the jet at the exit of the capillary under the influence of a static magnetic field. Figure 49 shows a set of images of the electrified jet electrospun from a solution loaded with 0.2%Fe_3O_4 with and without the presence of a magnetic field.

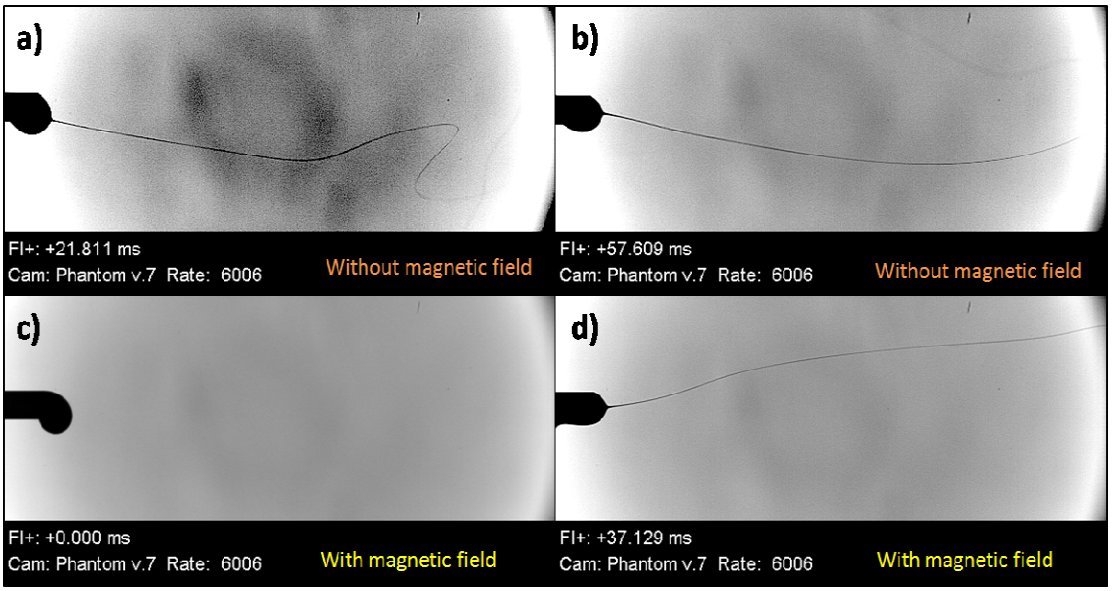

Figure 49. Images of an electrified jet from a 5%Fe_3O_4 in a 4%PEO/H_2O solution showing the effect of a static magnetic field in the development of the whipping instability: a) 1.2mL/hr, 140kV/m, 0Ga; b) 1.2mL/hr, 60kV/m, 0Ga; c) 1.2mL/hr, 40kV/m, 3725Ga; d) 1.2mL/hr, 60kV/m, 3725Ga.

Figure 49 shows how when applying a magnetic field during the electrospinning of magnetic solutions a larger electric field is required for the jet to initiate. A graph showing this behavior for the different solutions at the different volumetric flows is shown in Figure 50. The points in the graph represent the electric field threshold at which the electrospun jet was generated with and without a magnetic field. Below this value, solution dripping was observed.

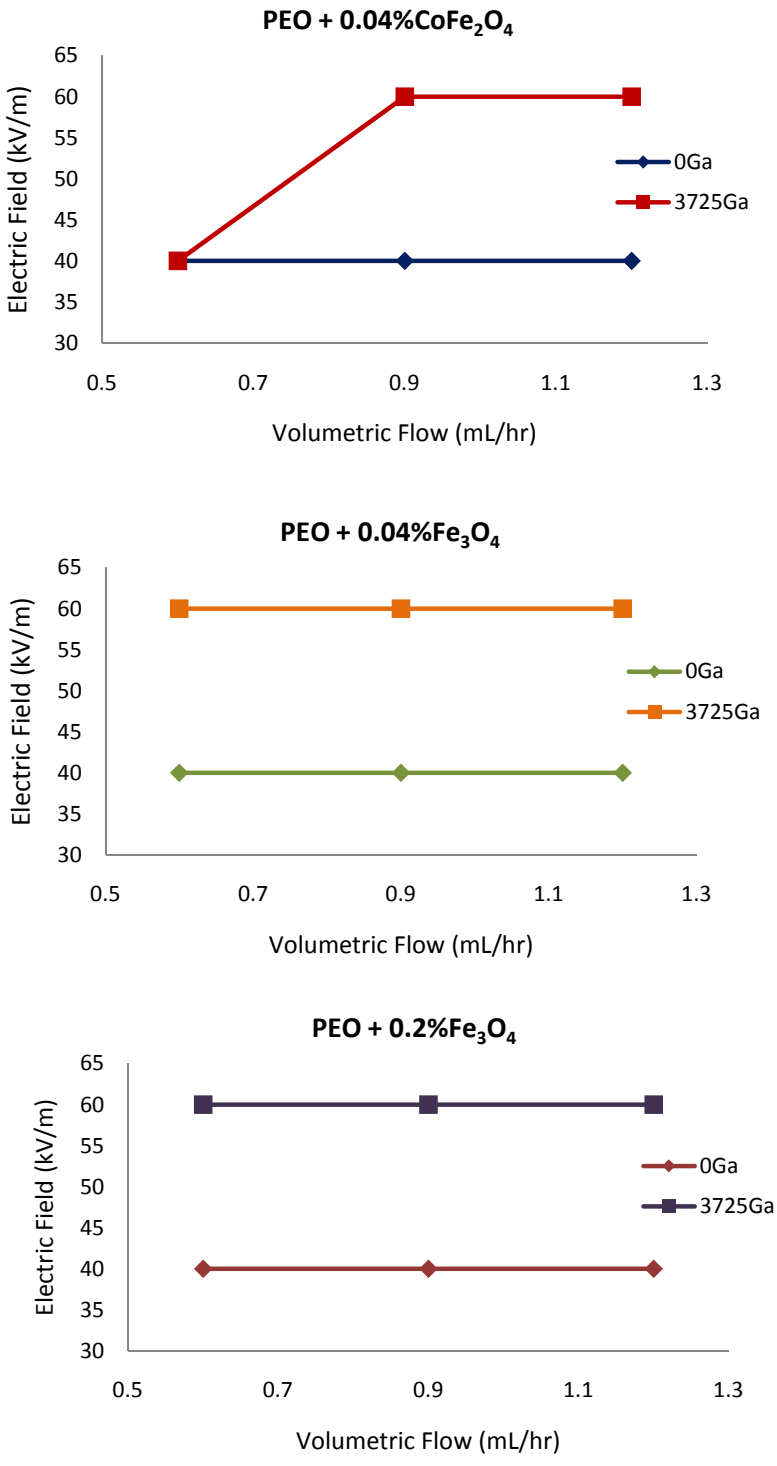

Figure 50 Effect of a static magnetic field in the development of the electrified jet when electrospinnig solutions loaded with magnetic nanoparticles.

Overall, an additional 20kV/m is needed for the jet to be expelled when applying a static magnetic field during electrospinning. We believe this extra energy is related to the magnetic force created between the applied field and the magnetic moment of the particle, given by {Rosenweig, 1985}:

$$\boldsymbol{F}_m = \mu_0(\boldsymbol{M} \cdot \nabla)\boldsymbol{H}_0 \qquad (43)$$

This equation states that under the presence of a static magnetic field a magnetic fluid will move in the direction of increasing field strength [66]. When the magnetic particles flow past the magnet, their magnetic moments align in the direction of the field. This alignment generates a magnetic force that drives them towards the center of the magnet. The additional electric field required for the onset of electrospinning accounts for the extra energy needed to overcome the magnetic force. This behavior is illustrated in Figure 51.

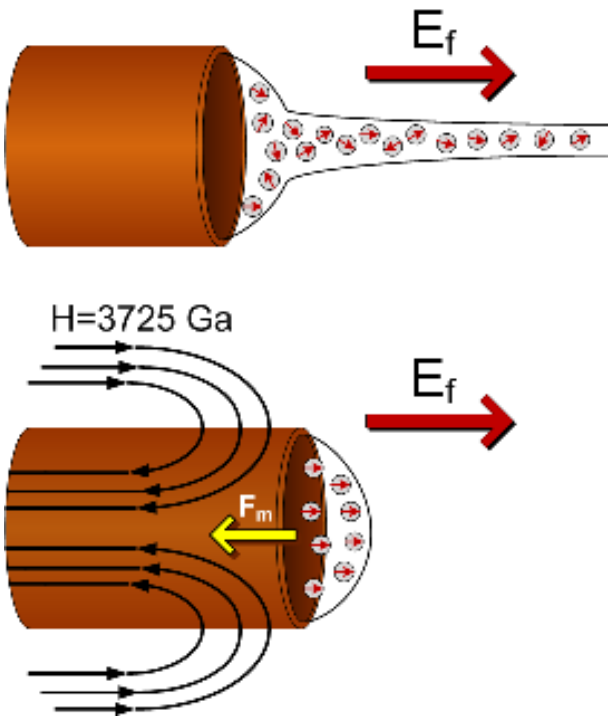

Figure 51 Effect of applying a static magnetic field on the development of the electrified jet. A magnetic force is created between the field and the magnetic fluid, which prevents the jet from being expelled.

For the solution loaded with cobalt ferrite no change was observed in the electric field threshold at the lowest volumetric flow (Figure 50). At lower volumetric flows the amount of mass ejected is less which results in a lower solution magnetization **M**. As a consequence, this decrease creates a lower attraction force which was easily surpassed by the same electric field when no magnet was present.

An increase in the straight path of the jet was observed at the lowest electric field when applying a magnetic field. This phenomenon was only visible for the 0.04%Fe_3O_4 solution where the transition occurred within the camera range of vision. This behavior can be seen from a set of high speed images in Figure 52. Figure 53 shows the measured distance for the different field/flow/magnet combinations.

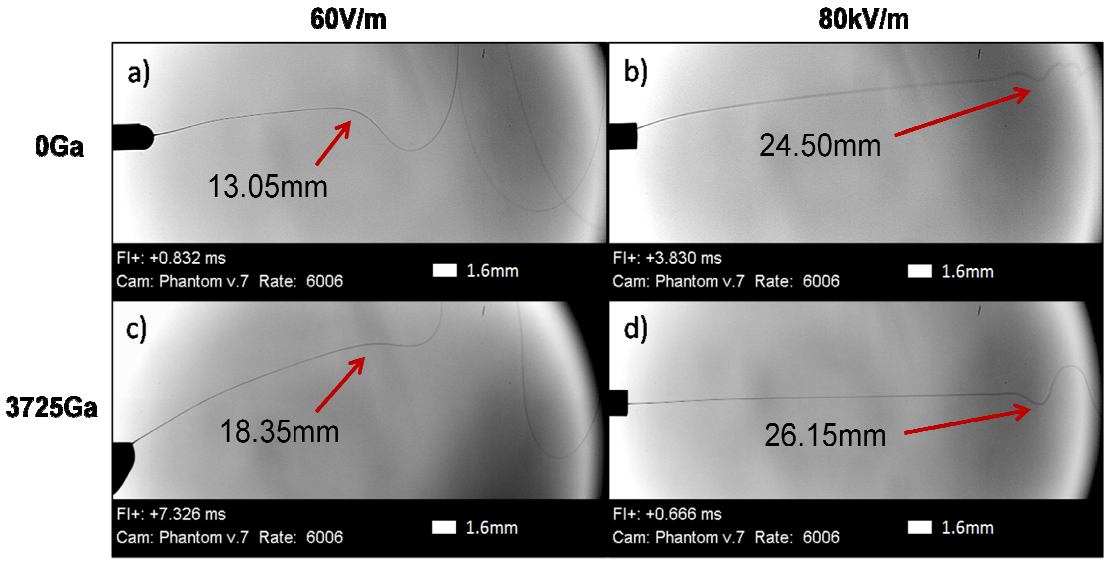

Figure 52. Effect of applying a static magnetic field on the onset of the whipping instability for the solution loaded with 0.04%Fe3O4 pumped at a volumetric flow of 0.9mL/hr. a) 60kV/m and 0Ga; b) 80kV/m and 0Ga; c) 60kV/m and 0Ga; d) 80kV/m and 3725Ga. It is clearly seen that the magnetic field increases the distance for the onset of the whipping instability.

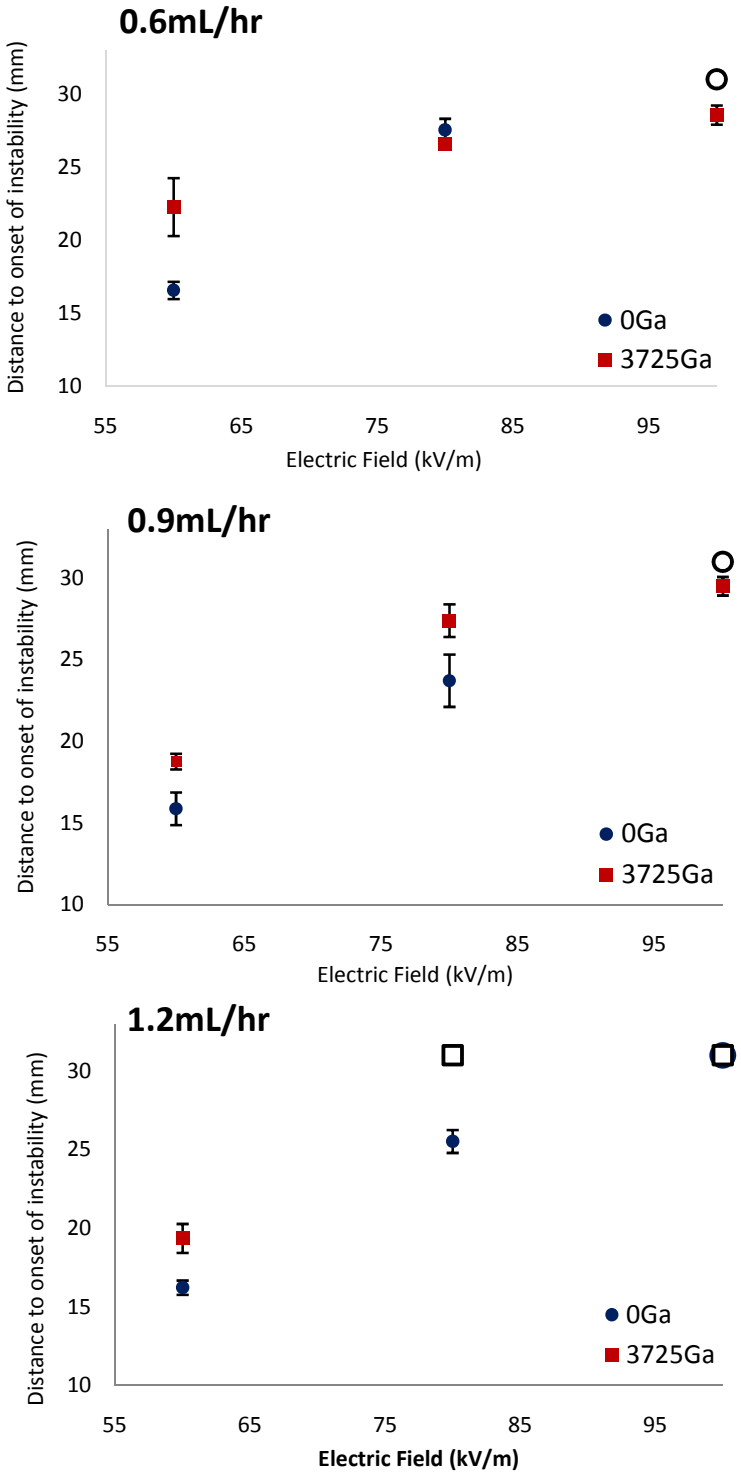

Figure 53. Effect of a static magnetic field on the length of the straight path before the onset of the whipping instability. The unfilled symbols represent that the transition occurred outside of the camera range of vision.

Figure 53 shows an increase in the straight path of the jet when applying a magnetic field. This effect was apparent at electric fields of 60 and 80kV/m and volumetric flows of 0.9 and 1.2mL/hr. Table 9 summarizes the percentage change values observed in Figure 53.

Table 9. Percentage change in the distance for the onset of the whipping instability for a solution loaded with 0.04%Fe_3O_4 when applying a static magnetic field. N/A corresponds to the values that could not be calculated because one or both of the data points lay outside of the visible range.

Volumetric flow (mL/hr)	Electric field (kV/m)	% Change in distance for onset of whipping instability
0.6	60	34.40%
0.6	80	-3.60%
0.6	100	N/A
0.9	60	18.21%
0.9	80	15.52%
0.9	100	N/A
1.2	60	19.28%
1.2	80	N/A
1.2	100	N/A

The increase in the straight path of the jet when applying a magnetic field is likely due to an increased resistance caused by a rise in viscosity. This behavior may be the result of an arrangement of magnetic moments prior to the expulsion of the jet. At the tip of the capillary the particle's magnetic dipoles align with the field. Following the jet expulsion a partial dipole arrangement remains due to both the magnet and neighboring dipoles. This arrangement enhances the resistance of the jet at low electric fields. The larger resistance is strong enough to counteract the developing perturbation caused by Coulombic interactions. As a result, the jet must travel a longer distance to overcome the interaction with the magnetic field in order for the whipping instability to take place. This behavior is consistent with previous observations where

an increase in the viscosity of the jet increases the onset of the whipping instability [20, 44].

Results deviate from those expected under an electric field of 100kV/m at 0.6 and 0.9mL/hr. With these parameters a decrease in the distance for the onset was observed when applying a magnetic field. It is not possible to assess the cause of this discrepancy since the magnetic field dies off before the distance at which these points were observed. Figure 54 shows the measured field strength of the magnet with increasing distance. At an approximate distance of 24mm the strength of the magnet is zero.

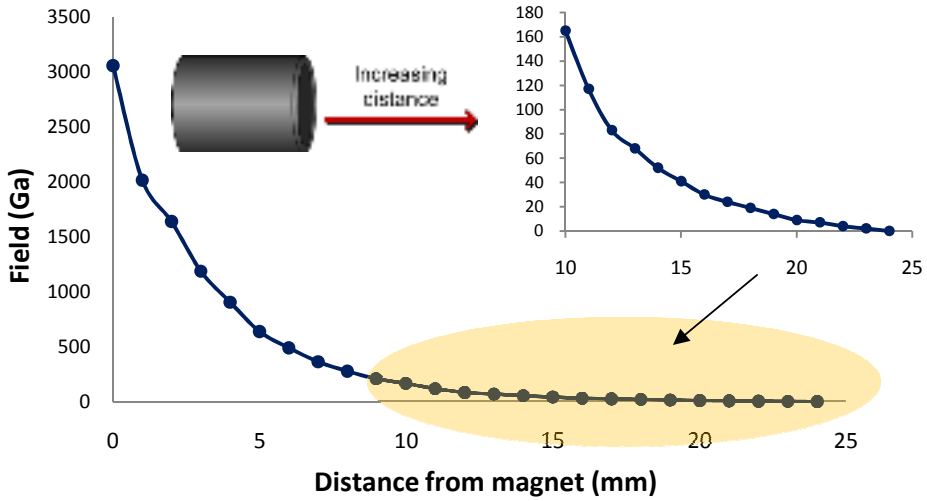

Figure 54. Experimental measurements showing the decrease in the magnetic field strength with increasing distance from the surface of the capillary. The field disappears at a distance of 24mm.

4.3.1 Statistical Analysis

Statistical analysis was carried to study the significance of an external magnetic field on the final diameter of the fibers. Both sets of fibers electrospun with and without a static magnetic field were analyzed. An initial model given by the following equation was fitted to the experimental data:

$$Y = \beta_0 + \beta_1 X_1 + \beta_2 X_2 + \beta_3 X_3 + \beta_4 X_4 + \beta_5 X_5 \qquad (44)$$

Where Y= fiber diameter (nm), X_1= volumetric flow (mL/hr), X_2= electric field (kV/m), X_3= magnetic content (vol% in resulting fibers), X_4= magnetic material (X_4=1 for $CoFe_2O_4$; 0 for Fe_3O_4), and X_5= magnetic field (Ga). X_4 was modeled as a categorical variable capable of predicting the influence of the type of magnetic material. This variable can only take 2 values: 1 if the solution is loaded with $CoFe_2O_4$ and 0 if it's loaded with Fe_3O_4. X4 was added to the model to see if a single equation capable of accounting for different magnetic materials could be fitted to our data. The same variable type was employed for the magnetic field. In this situation X_5 can only be 1 is the field is present or zero otherwise. An R^2 value of 0.852 was obtained from this fit. Table 10 shows the slope estimates as well as the p-values for the different predictors.

Table 10. Statistics for initial fit.

Predictor	Estimate	p-value
Intercept	$\beta_0 = 244.72 \pm 28.00$	3.66E-24
X_1 - Volumetric Flow (mL/hr)	$\beta_1 = -2.36 \pm 16.33$	0.822924
X_2 - Electric Field (kV/m)	$\beta_2 = -0.55 \pm 0.25$	4.67E-05
X_3 - Magnetic Content (% in fiber)	$\beta_3 = 4.28 \pm 3.19$	0.009436
X_4 - Magnetic Material	$\beta_4 = 50.45 \pm 6.23$	5.12E-23
X_5 - Magnetic Field (Ga)	$\beta_5 = -7.63e^{-5} \pm 2.71e^{-3}$	0.95765

R2=0.852

From the p-values of Table 6 we can see that neither magnetic field nor volumetric flow had a significant effect on the fiber diameter. This indicates that the effect of the static magnetic field is localized. The field does have an effect on the development of the electrospun jet and the whipping instability. However, this field does not alter the rheological properties of the polymer solution. Once the jet is no longer under the influence of the magnetic field, the rheological properties of the

solution come into effect. Taking away the non significant predictors we obtain the following equation for the final fiber diameter:

$$F.Diameter\ (nm) = 252.62 - 0.55[E.Field\ (kV/m)] + 4.27[Conc.Part.\ in\ Fibers\ (vol\%)] + 50.43[Magnetic\ Material]; \qquad R^2 = 0.852 \qquad (45)$$

Equation 45 is in agreement with the one derived when no magnetic field was employed. A unit increase in the electric field results in a reduction of the average fiber diameter. Furthermore, this equation predicts an increase of 50.43 in the resulting fiber diameter when electrospinning cobalt ferrite solutions. This behavior is consistent with the high viscosity and lower conductivity shown by the cobalt ferrite solution.

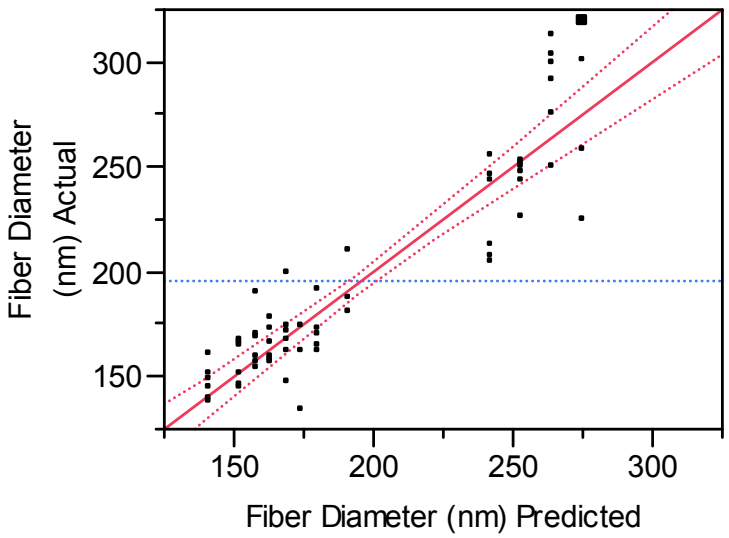

Figure 55. Actual against predicted diameters from the following model: *F.Diameter (nm) = 252.62 – 0.55[E.Field (kV/m)] + 4.27[Conc.Part. in Fibers (vol%)] + 50.43[Magnetic Material]*. The R^2 value for this model was 0.852.

Different models taking accounting for interaction terms where fitted to the experimental data. None of these resulted in a significant increase in the R^2 value. As a result, Equation 45 is the best option for modeling the experimental data. The actual data against predicted graph is shown in Figure 55 for the model obtained with Equation 45.

5. CONCLUSIONS

We have demonstrated the feasibility of manipulating the electrospinning process by employing a magnetic field when processing polymer solutions embedded with magnetic nanoparticles. A larger electric field was required to initiate the electrospinning process when applying a static magnetic field. This was the results of a magnetic force created between the magnetic field and the particles within the magnetic fluid.

At low electric fields the distance for the onset of the whipping instability was increased by applying a static magnetic field. This behavior was attributed to an increase in the viscoelastic resistance of the jet caused by the magnetoviscous effect. Statistical analysis showed that the magnetic field had no significant effect on the resulting fiber diameters. This indicated that the increase in viscosity was a localized effect. Once the jet has overcome the influence of the magnet, the rheological properties of the polymer solution come into play.

Electrospinning proved to be a simple method for producing nanofibers with distinctive magnetic properties. Depending on the magnetic filler, fibers with either ferromagnetic or superparamagnetic properties were created. The magnetic properties of these fibers were intensified when compared to those of the precursor solutions. Still, both the fibers and precursor solutions showed the same magnetic behavior.

Solution viscosity is the most significant parameter during the electrospinning process. This parameter had an effect on both the resulting fiber diameter and the distance for the onset of the whipping instability. These two are related to the viscoelastic resistance of the jet. This resistance determines the length of the initial straight path as well as the perturbation amplitude, both of which determine the final fiber diameter.

The viscoelastic properties of the precursor solutions were modified with the addition of particles. This behavior resulted from a change in the entanglement structure of the polymer molecules. Solution sonication also generated a drastic decrease in solution viscosity. This decrease was the consequence of chain scission created by cavitation. The addition of particles dissipated the energy released during cavitation, which in turn decreased the rate of degradation of polymer chains.

6. FUTURE WORK

6.1 Effect of Particle Loading on the Rheology of Polymer Solutions

In this work we were able to see that magnetic nanoparticle addition to a PEO solution results in a decrease in the solution viscosity. This behavior has been observed in polymer melts and it was attributed to a chain confinement effect[149]. Although we worked with polymer solutions, the same confinement principle should hold since chain entanglements may exist in both polymer melts and solutions.

A complete rheological study employing solutions with different polymer concentration, particle size, and particle loading should be performed. The objective of this study will be to validate the hypothesis proposed by Tuteja *et al*.[149] for polymer solutions. Solutions with different polymer concentration should be prepared. The concentration of these solutions should be below the critical entanglement concentration, near the critical entanglement concentration, and above the critical entanglement concentration. This critical entanglement concentration is calculated with Equation 34 and it will depend on the molecular weight and radius of gyration of the polymer selected.

According to the work done by Tuteja *et al.*, below the critical polymer concentration an increase in the viscosity should result with the addition of particles. Near the critical entanglement concentration no significant change in the viscosity of the polymer solution will be expected. A decrease in viscosity should be observed with solutions in the entangled regime. These solutions have polymer concentrations above the critical entanglement concentration. Solutions with different particle loadings should be prepared varying the R_g/h ratio. R_g corresponds to the radius of gyration of the polymer, which is given by $R_g = 0.215{M_w}^{0.583}$ Å for PEO in water. h is the average interparticle distance obtained with Equation 33. It is expected that with an R_g/h lower than 1 an increase in the viscosity of the polymer solution should be

obtained. However, when Rg/h>1 the viscosity of the polymer solution should decrease as a result of chain confinement.

6.2 Effect of Solution Properties and Processing Parameters during Electrospinning

High speed camera imaging of the electrospinning process should be performed with a wider range of vision. A wider range of vision will let us visualize the onset of the whipping instability at distances larger than 31mm. With these experiments, a better understanding of the effect of solution viscosity on the development of the whipping instability should be obtained. It is expected that the solution with the highest viscosity should show the onset of the whipping instability further away than that seen for the low viscosity solutions.

In this study aqueous solutions of PEO with different particle loadings were studied. The distance between the tip of the capillary and the grounded collector was kept constant at 25cm. This distance was required to allow for the complete evaporation of water. With our camera setup we were only able to capture the first 3cm of the flight path of the jet. To solve this issue either a slower frame rate or a different lighting setup should be employed. In this work, an LED was employed as the light source due to our high frame rate. The problem with this setup is the small focus area that is obtained. If the frame rate is decreased (3000fps) a gooseneck or a slide projector can be employed. Additionally, a different polymer/solvent system can be employed. By choosing a volatile solvent, the distance between the capillary and the grounded collector can be decreased.

6.3 Negative Viscosity Effect on the Electrospinning Process

An apparatus capable of producing an alternating magnetic field has been built. With this equipment the negative viscosity effect on the electrospinning process will be studied. An AC current will be generated using an AC signal generator connected

to a current amplifier capable of delivering 5A. The AC current will be circulated through a solenoid wounded around a manganese-zinc (MnZn) ferrite tubing. The ferrite tubing will be placed around the tip of the capillary. Figure 56 shows a schematic diagram of this setup.

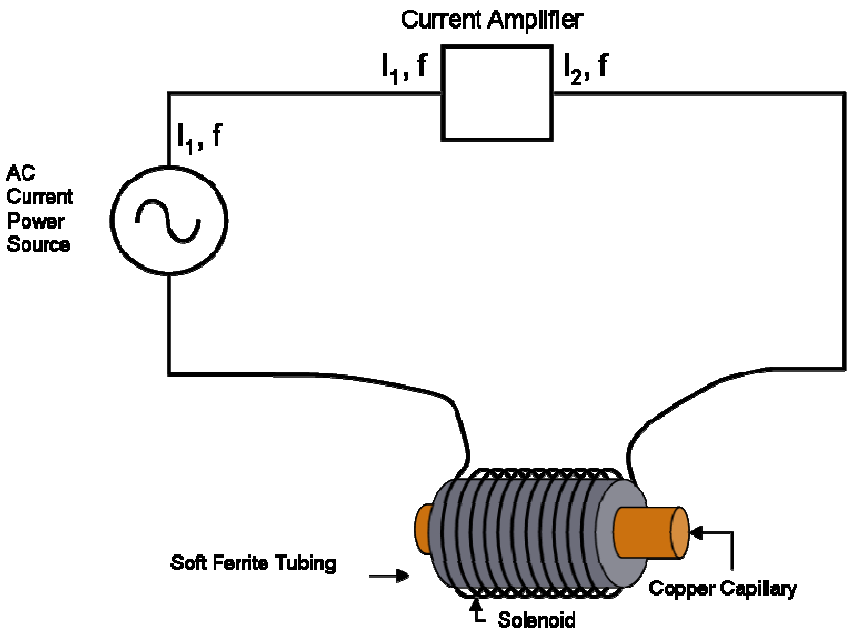

Figure 56. Schematic diagram of the apparatus capable of delivering an alternating field to the tip of the capillary.

The purpose of the ferrite tubing is to enhance the magnetic field within the capillary. The ferrite has a saturation magnetization value of 3800Ga at 1000Oe and a relative initial permeability of 900. This material also has a large resistivity (~0.2Ωm; Cu = $1.72e^{-8}$Ωm), which should avoid any electrical interaction between the charged capillary and the electrified coil. To achieve a field strength of 3800Ga within the tubing, an applied field of 15,000A/m (189Oe) must be generated with the solenoid. This value takes into account the demagnetizing field given by $H_{dem}=N_dM_{sat}$. N_d is the demagnetizing factor which is 0.043 for the ferrite tubing employed. Two solenoids with 90 and 70 turns have been built. These two solenoids are capable of generating a

magnetic field of about 15,000A/m (190Oe) and 12,000A/m (150Oe), respectively, using a current of 3A. A set of images of one solenoid is shown in Figure 57.

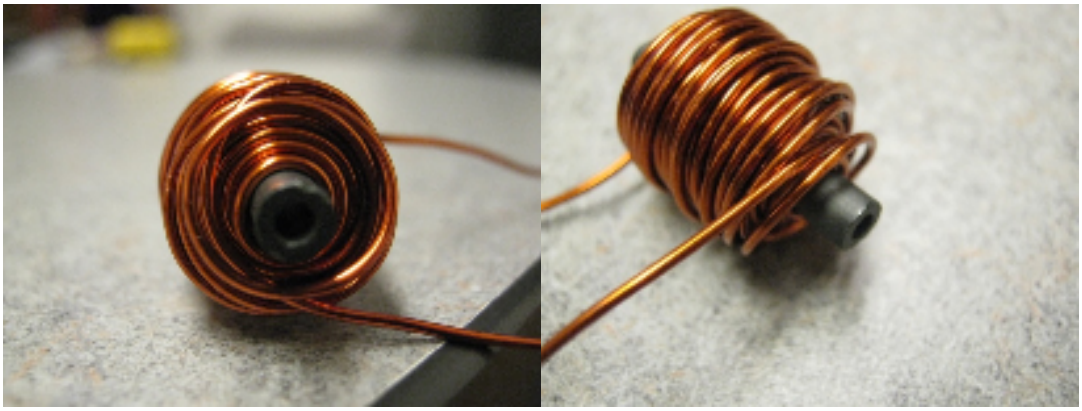

Figure 57. Images of a solenoid wound around a MnZn ferrite tubing with 90 turns. This solenoid is capable of creating a field of 15,000A/m within the ferrite tubing.

Using these solenoids the negative viscosity effect on the electrospinning process will be studied. First, an apparatus capable of measuring the pressure difference in the capillary between the inlet and the outlet of the solenoid will be built. Within this capillary a polymer solution loaded with magnetic nanoparticles will be pumped. The pressure difference will allow us to calculate the viscosity of the fluid under an influence of the magnetic field. This value will be calculated using Poiseuille's equation:

$$\mu = \frac{\Delta P \pi r^4}{VL8}$$

Where μ is the fluids viscosity, ΔP the pressure difference between the inlet and the outlet of the solenoid, r the radius of the capillary, *V* the volumetric flow, and *L* the length of the capillary between both pressure measurements.

The negative viscosity equation proposed by Shliomis was derived for magnetic particles in aqueous or oil carriers. This equation should be corrected to account for polymer solutions since the particles will not be able to rotate as freely as

in aqueous solvents due to interactions with neighboring polymer chains. The shear rate at which the solution is being pumped through the capillary should also be considered. This consideration comes from the fact shear rate influences the conformation of polymer chains in solution.

Once the negative viscosity effect has been confirmed for polymer solutions a solenoid will be placed on the tip of the capillary during electrospinning. From the induced decrease in viscosity we expect the onset of the whipping instability to occur closer to the tip of the capillary. This should result in smaller diameter fibers than those obtained without an external magnetic field.

APPENDIX I

High speed images of an electrified jet electrospun from a solution loaded with 0.04vol% Fe_3O_4. Four frames at different electrospinning times are shown in each Figure. The electrospinning conditions as well as the distance for the onset of the whipping instability and its average of the four images are given in the caption of each figure.

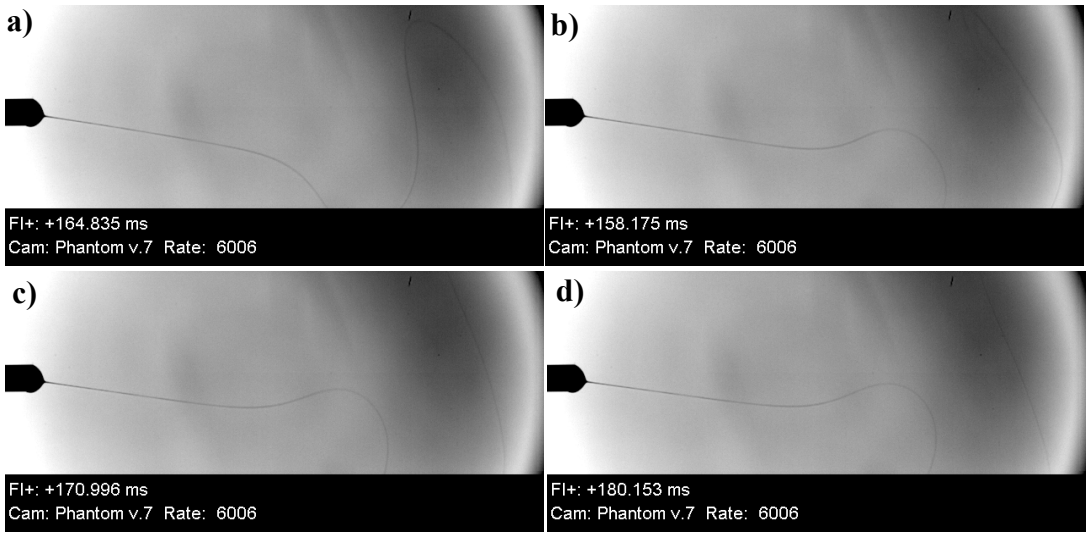

Figure 58. Images of an electrified jet at different times electrospun at 0.6mL/hr, 40kV/m and 0Ga. The distance for the onset of the whipping instability is a)14.18mm; b) 14.10mm; c) 13.16mm; d) 12.84mm. The average distance is 13.57±0.67mm.

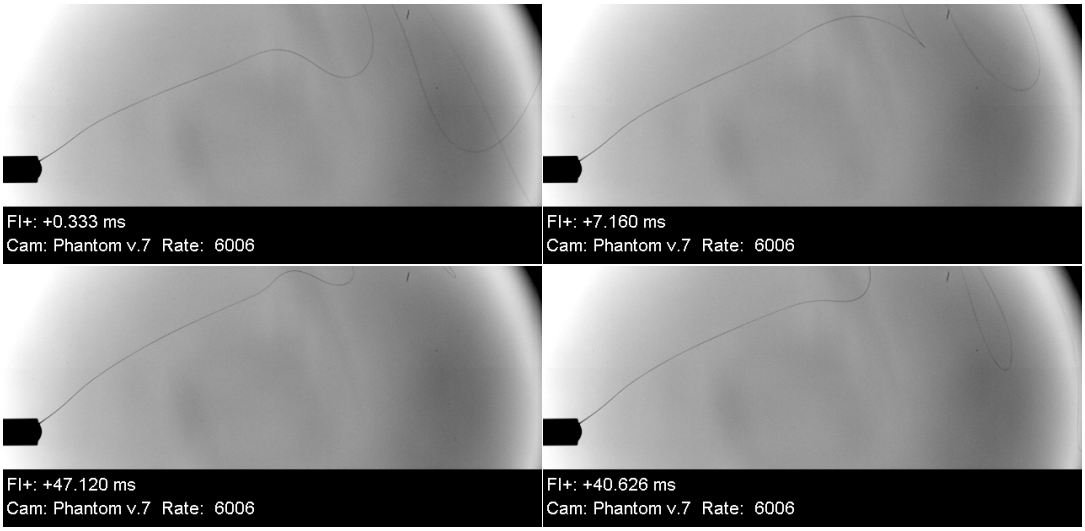

Figure 59. Images of an electrified jet at different times electrospun at 0.6mL/hr, 60kV/m and 0Ga. The distance for the onset of the whipping instability is a) 16.24mm; b) 17.38mm; c) 16.66mm; d) 16.13mm. The average distance is 16.57±0.59mm.

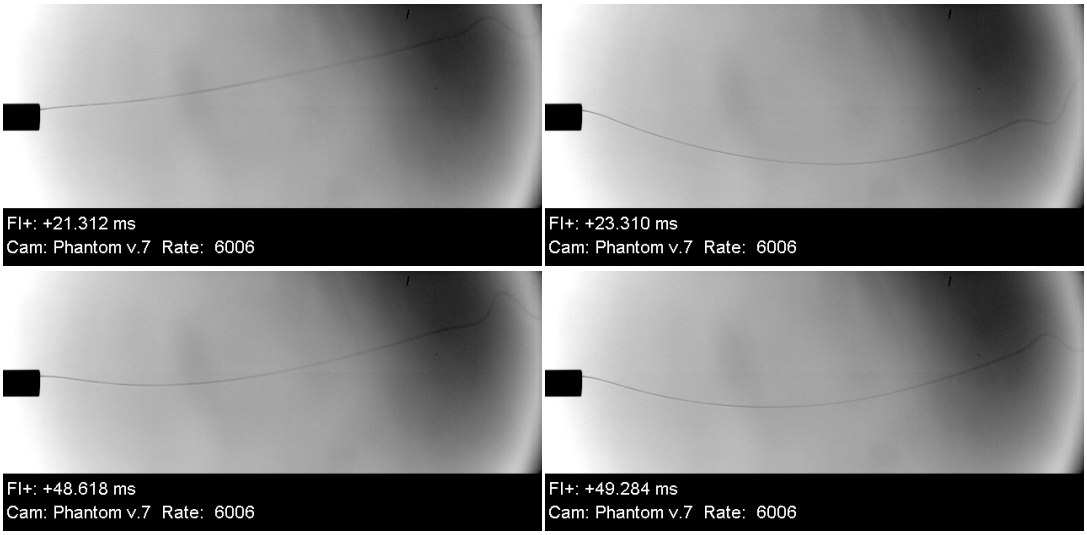

Figure 60. Images of an electrified jet at different times electrospun at 0.6mL/hr, 80kV/m and 0Ga. The distance for the onset of the whipping instability is a) 26.43mm; b) 27.79mm; c) 27.61mm; d) 28.27mm. The average distance is 27.53±0.78mm.

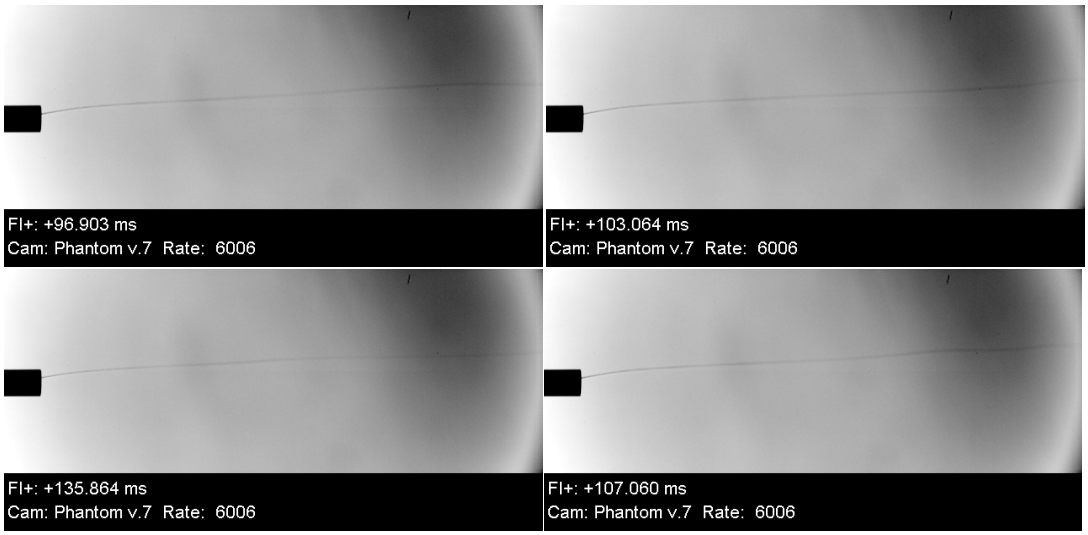

Figure 61. Images of an electrified jet at different times electrospun at 0.6mL/hr, 100kV/m and 0Ga. The distance for the onset of the whipping instability is a) >31mm; b) >31mm; c) >31mm; d) >31mm. The average distance is >31mm.

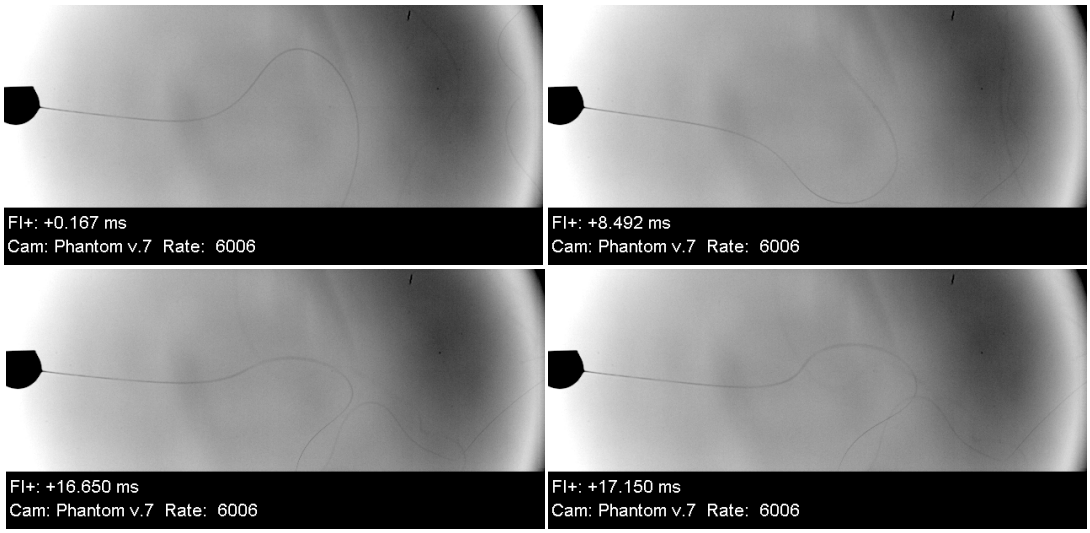

Figure 62. Images of an electrified jet at different times electrospun at 0.9mL/hr, 40kV/m and 0Ga. The distance for the onset of the whipping instability is a) 10.02mm; b) 10.97mm; c) 10.62mm; d) 11.57mm. The average distance is 10.49±0.68mm.

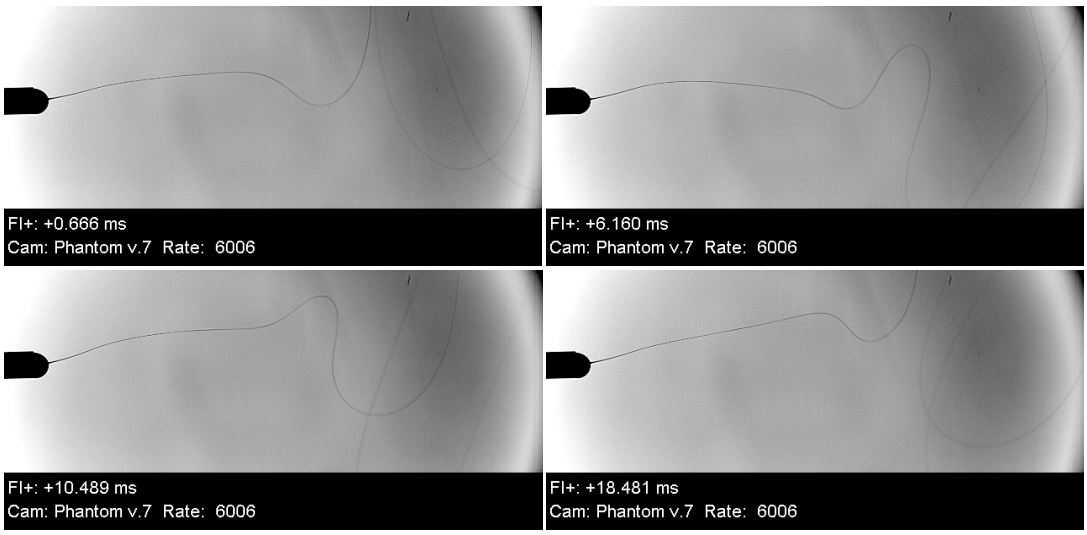

Figure 61. Images of an electrified jet at different times electrospun at 0.9mL/hr, 60kV/m and 0Ga. The distance for the onset of the whipping instability is a) 13.57mm; b) 15.87mm; c) 14.02mm; d) 14.74mm. The average distance is 14.55±0.68mm.

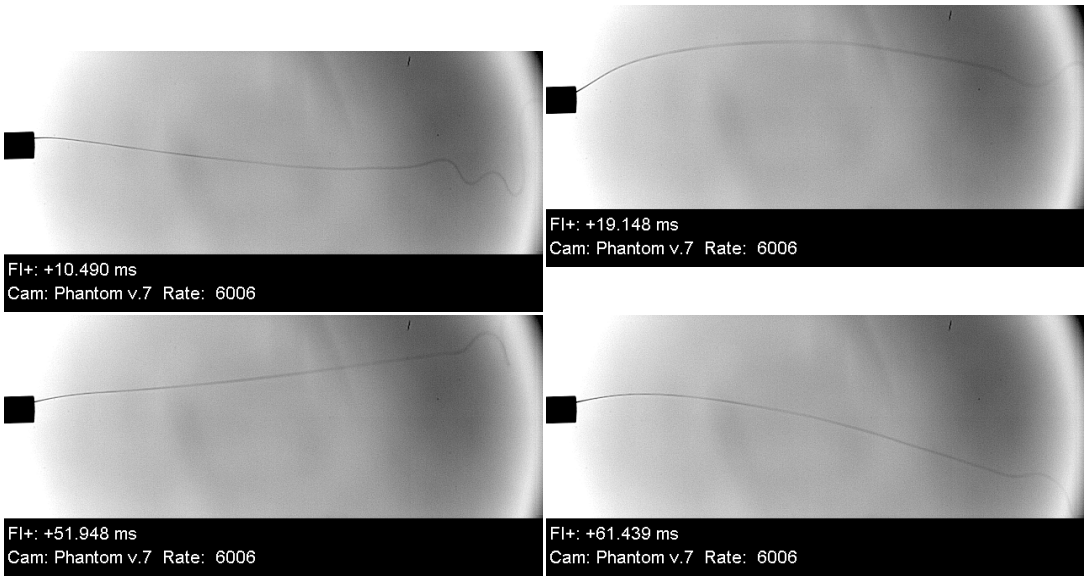

Figure 62. Images of an electrified jet at different times electrospun at 0.9mL/hr, 80kV/m and 0Ga. The distance for the onset of the whipping instability is a) 23.71mm; b) 26.39mm; c) 25.25mm; d) 27.50mm. The average distance is 25.96±1.60mm.

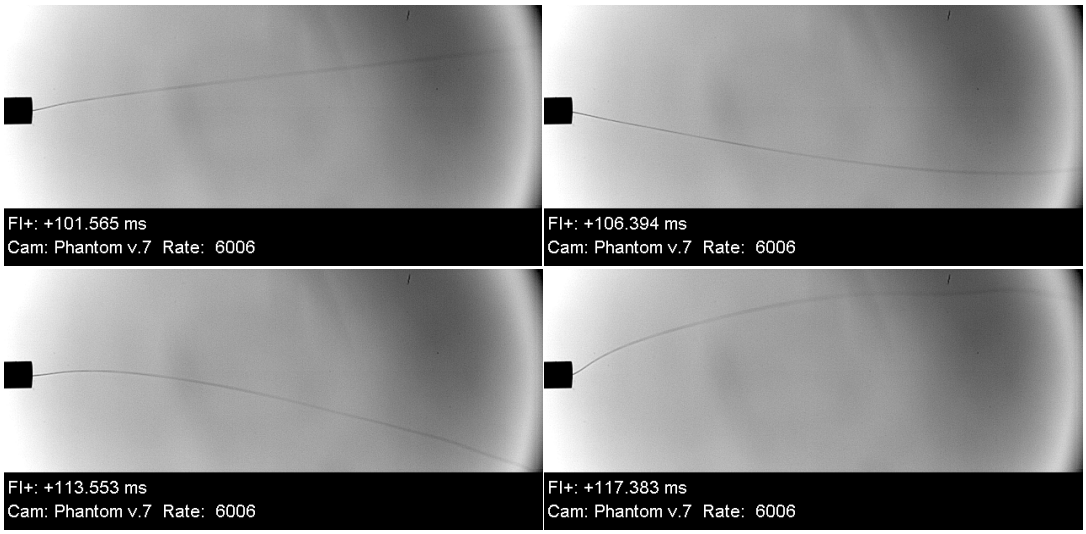

Figure 63. Images of an electrified jet at different times electrospun at 0.6mL/hr, 100kV/m and 0Ga. The distance for the onset of the whipping instability is a) >31mm; b) >31mm; c) >31mm; d) >31mm. The average distance is >31mm.

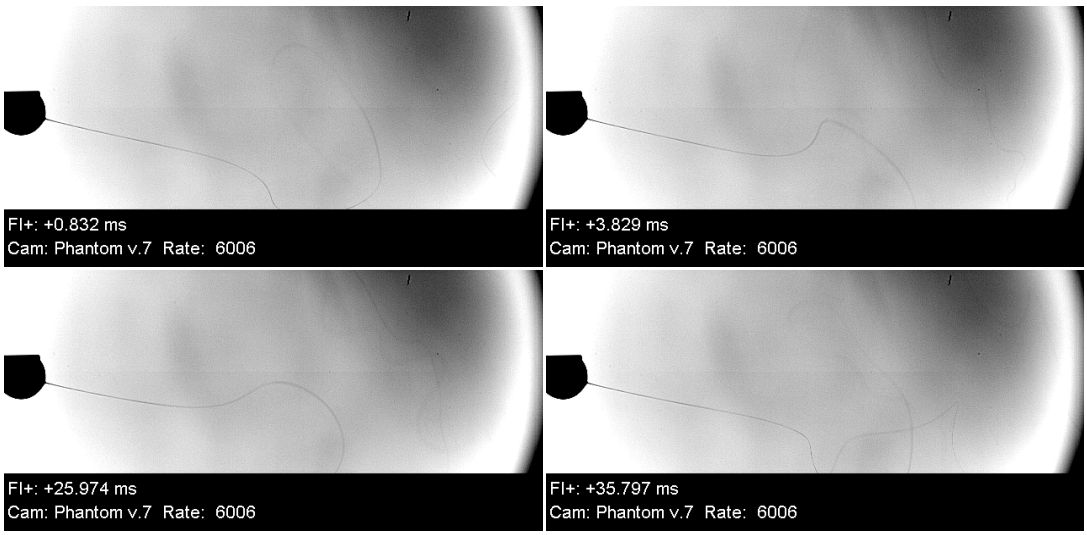

Figure 64. Images of an electrified jet at different times electrospun at 1.2mL/hr, 40kV/m and 0Ga. The distance for the onset of the whipping instability is a) 13.78mm; b) 12.22mm; c) 11.09mm; d) 14.02mm. The average distance is 13.78±1.35mm.

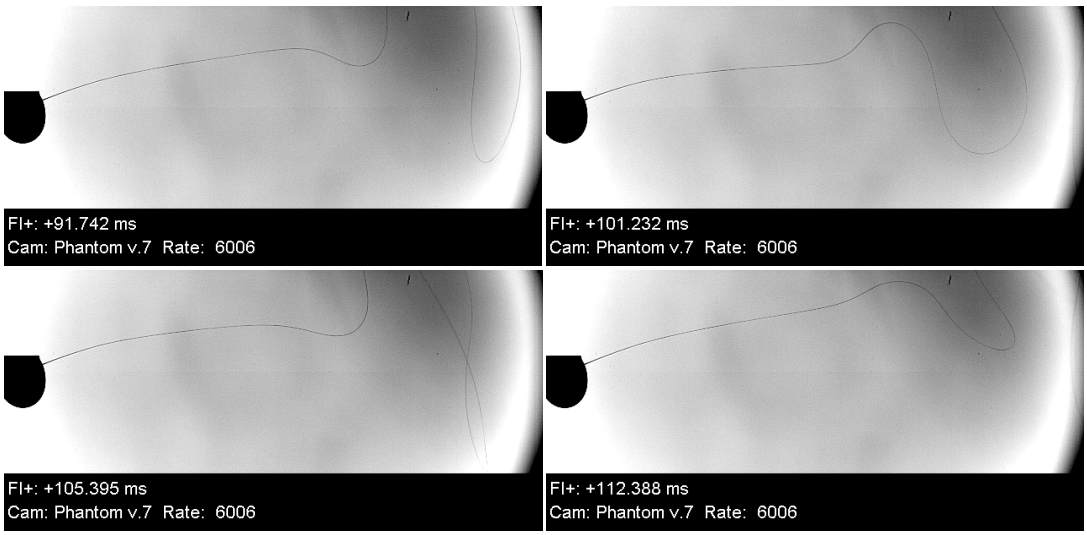

Figure 65. Images of an electrified jet at different times electrospun at 1.2mL/hr, 60kV/m and 0Ga. The distance for the onset of the whipping instability is a) 16.47mm; b) 16.06mm; c) 15.70mm; d) 16.71mm. The average distance is 16.23±0.45mm.

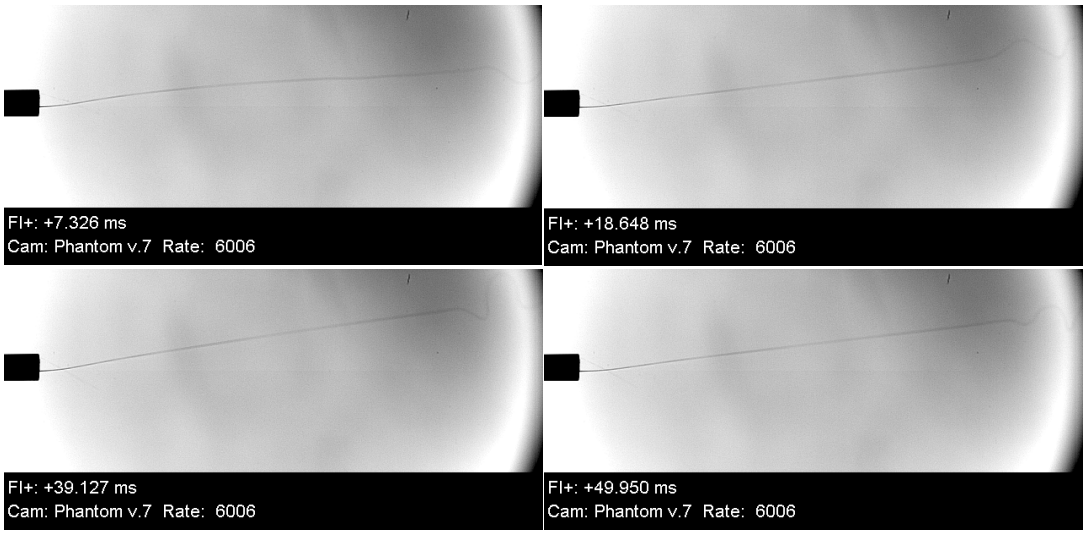

Figure 66. Images of an electrified jet at different times electrospun at 1.2mL/hr, 80kV/m and 0Ga. The distance for the onset of the whipping instability is a) 27.57mm; b) 25.94mm; c) 26.10mm; d) 26.51mm. The average distance is 25.53±0.73mm.

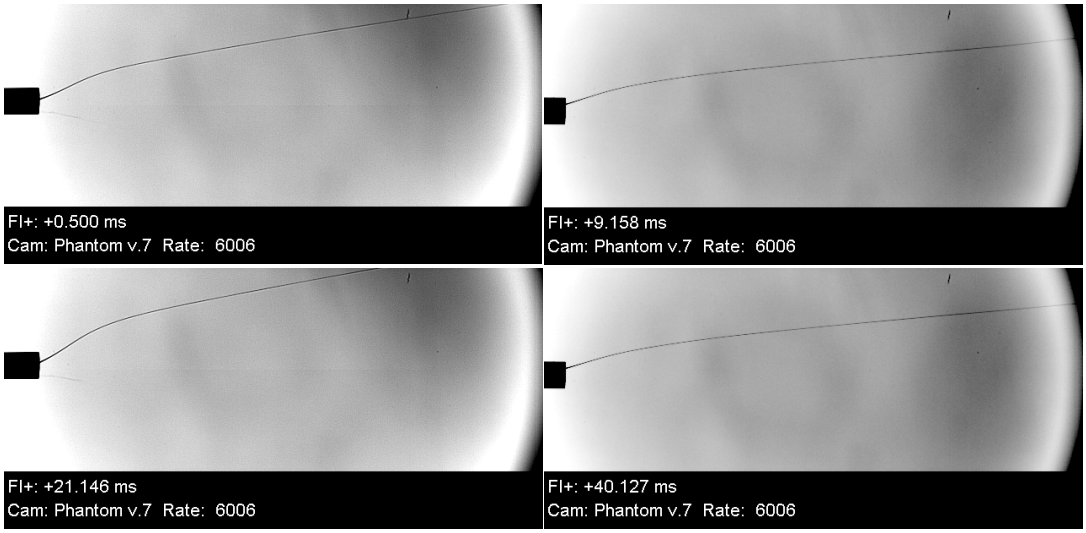

Figure 67. Images of an electrified jet at different times electrospun at 1.2mL/hr, 100kV/m and 0Ga. The distance for the onset of the whipping instability is a) >31mm; b) >31mm; c) >31mm; d) >31mm. The average distance is >31mm.

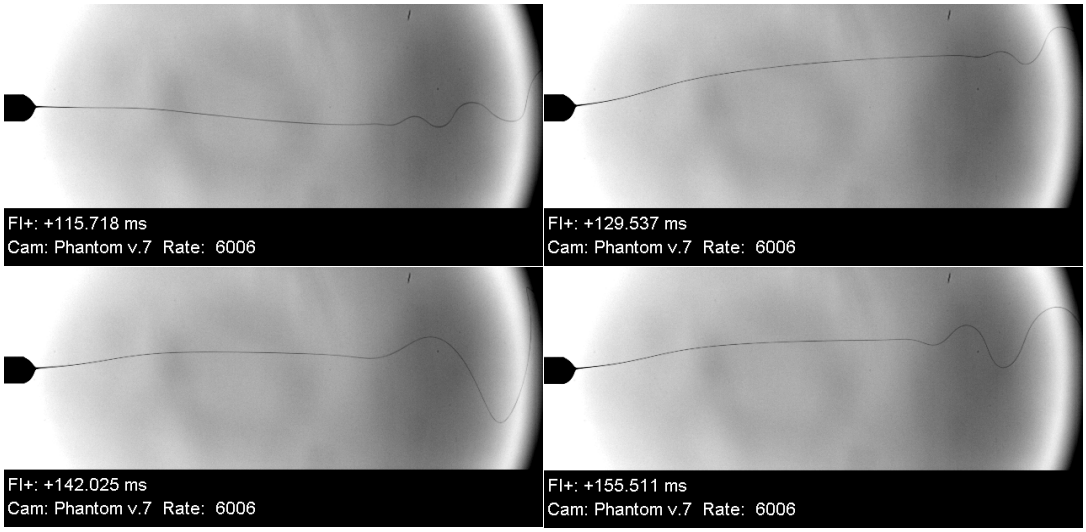

Figure 68. Images of an electrified jet at different times electrospun at 0.6mL/hr, 60kV/m and 3725Ga. The distance for the onset of the whipping instability is a) 22.18mm; b) 25.09mm; c) 20.97mm; d) 20.82mm. The average distance is 22.27±1.98mm.

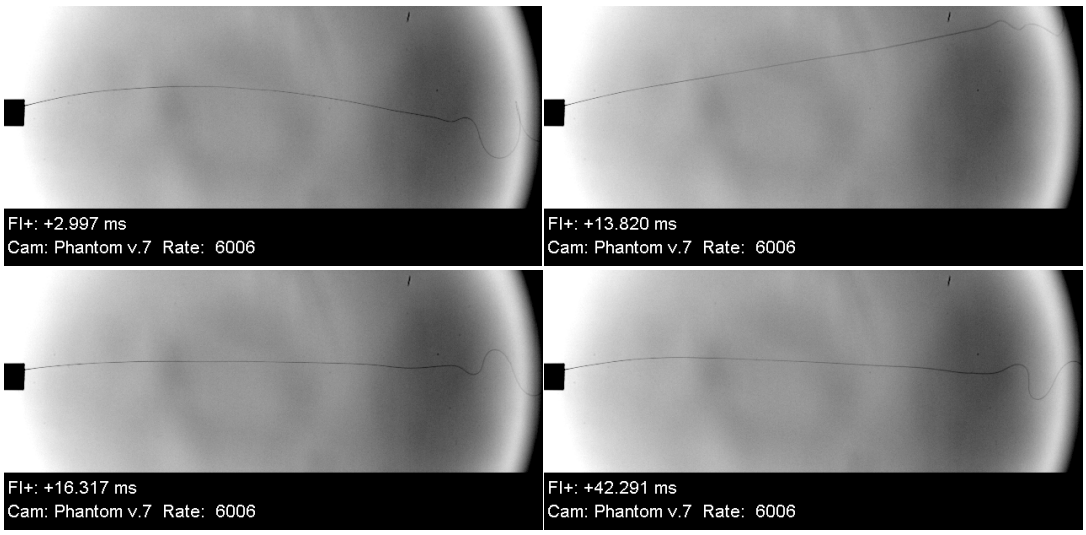

Figure 69. Images of an electrified jet at different times electrospun at 0.6mL/hr, 80kV/m and 3725Ga. The distance for the onset of the whipping instability is a) 26.60mm; b) 26.45mm; c) 26.25mm; d) 26.87mm. The average distance is 26.54±0.26mm.

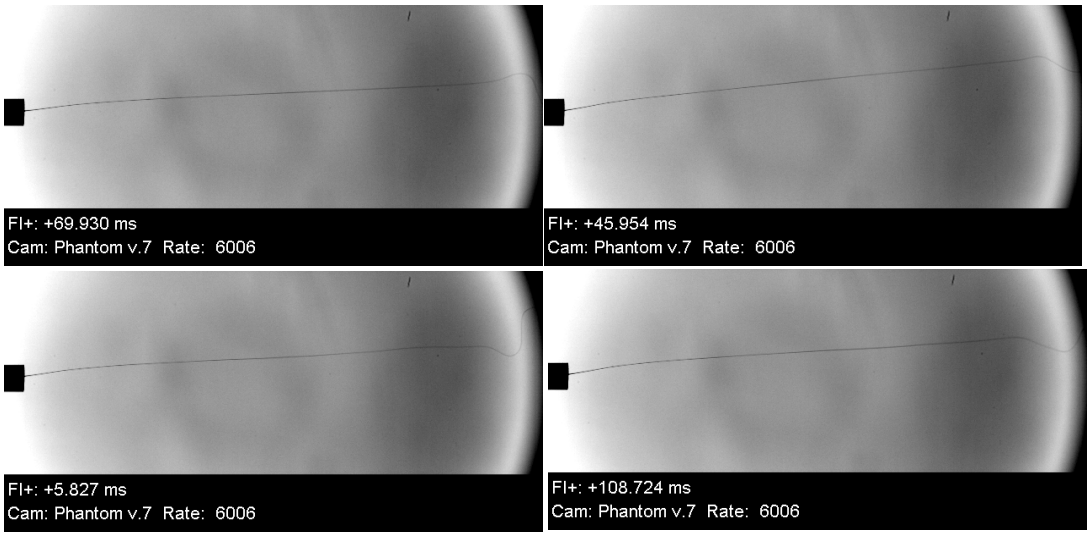

Figure 70. Images of an electrified jet at different times electrospun at 0.6mL/hr, 100kV/m and 3725Ga. The distance for the onset of the whipping instability is a) 28.56mm; b) 29.16mm; c) 28.86mm; d) 27.66mm. The average distance is 28.56±0.65mm.

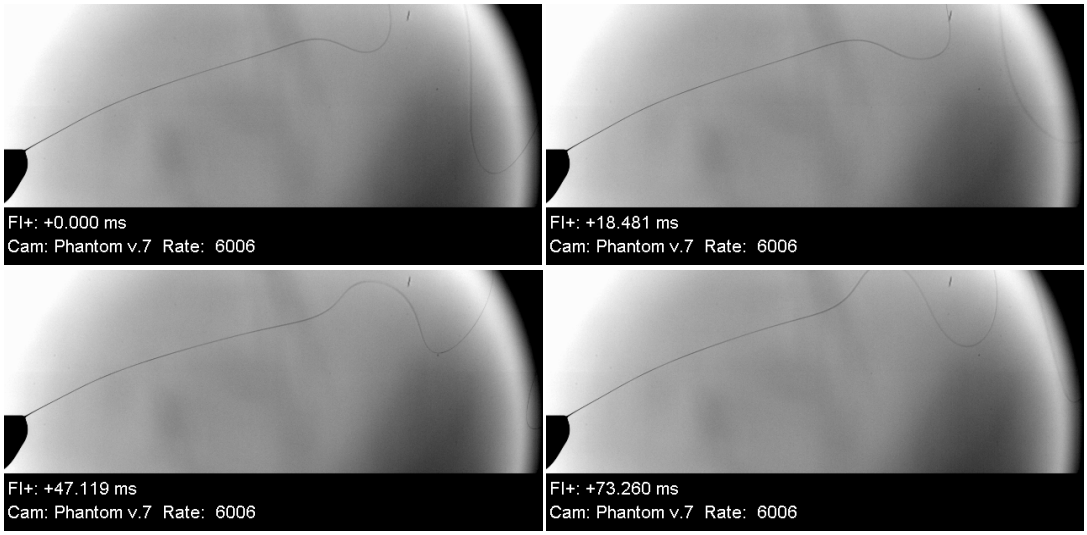

Figure 71. Images of an electrified jet at different times electrospun at 0.9mL/hr, 60kV/m and 3725Ga. The distance for the onset of the whipping instability is a) 18.96mm; b) 18.80mm; c) 19.19mm; d) 18.08mm. The average distance is 18.76±0.48mm.

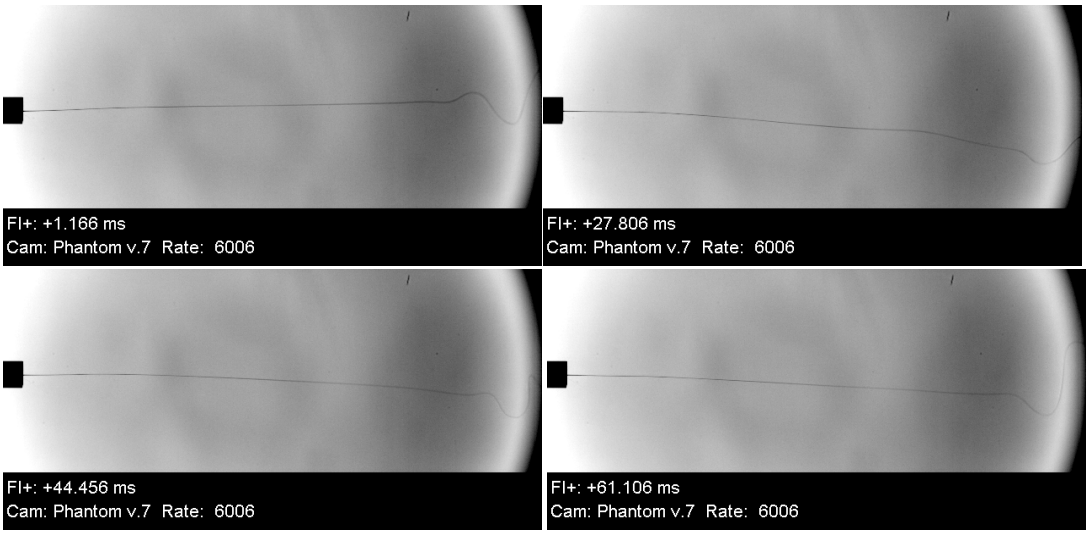

Figure 72. Images of an electrified jet at different times electrospun at 0.9mL/hr, 80kV/m and 3725Ga. The distance for the onset of the whipping instability is a) 26.17mm; b) 28.35mm; c) 27.72mm; d) 27.33mm. The average distance is 27.39±0.92mm.

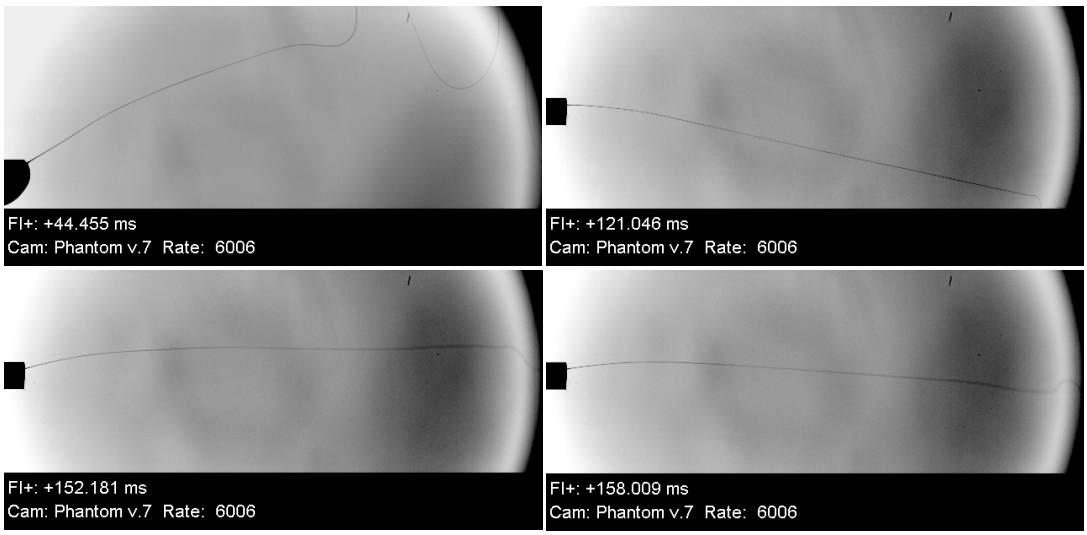

Figure 73. Images of an electrified jet at different times electrospun at 0.9mL/hr, 100kV/m and 3725Ga. The distance for the onset of the whipping instability is a) 29.12mm; b) 28.90mm; c) 29.93mm; d) 30.05mm. The average distance is 27.39±0.92mm.

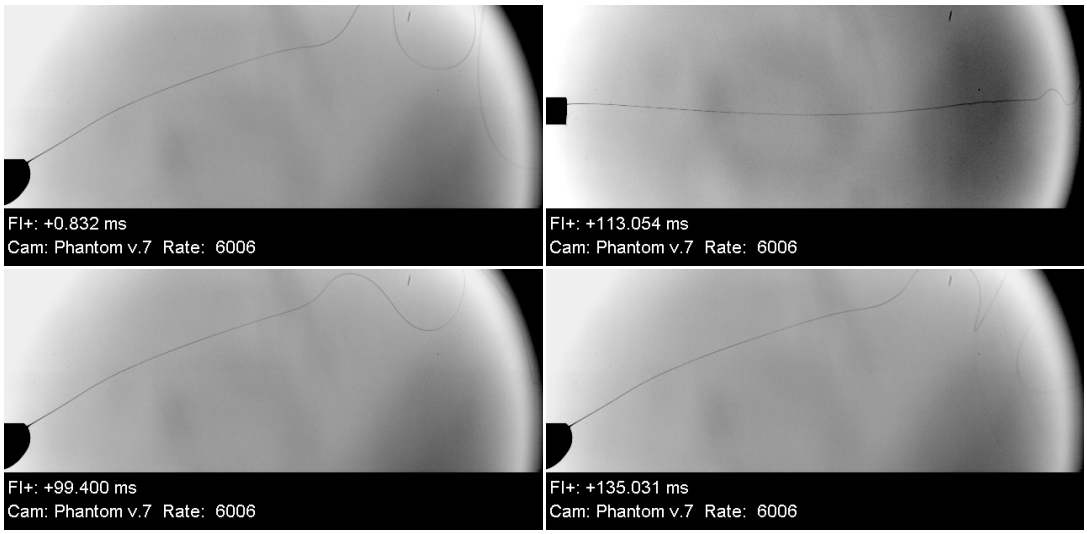

Figure 74. Images of an electrified jet at different times electrospun at 1.2mL/hr, 60kV/m and 3725Ga. The distance for the onset of the whipping instability is a) 19.10mm; b) 18.44mm; c) 19.28mm; d) 20.63mm. The average distance is 19.36±0.92mm.

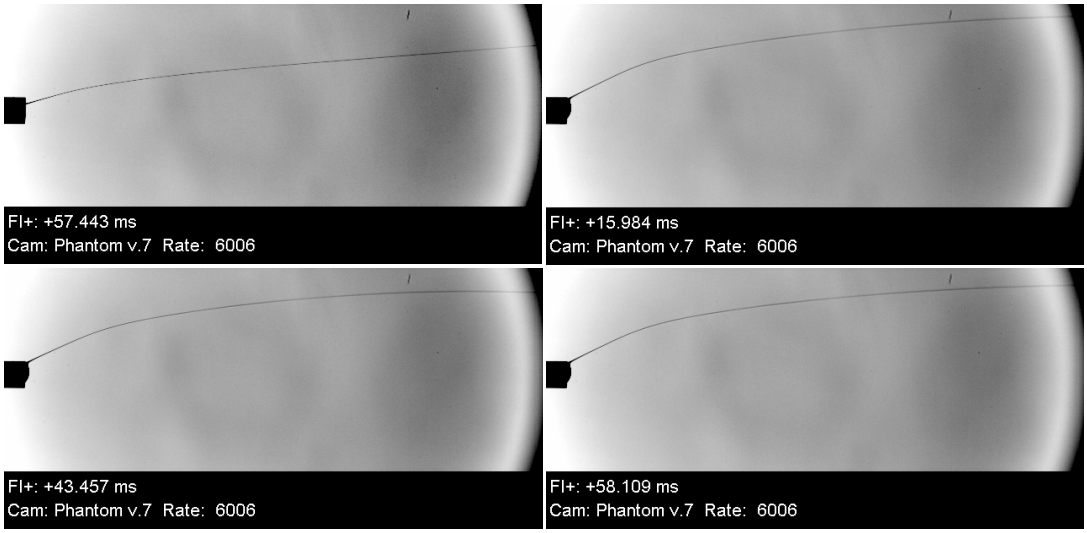

Figure 75. Images of an electrified jet at different times electrospun at 1.2mL/hr, 80kV/m and 3725Ga. The distance for the onset of the whipping instability is a) >31mm; b) >31mm; c) >31mm; d) >31mm. The average distance is >31mm.

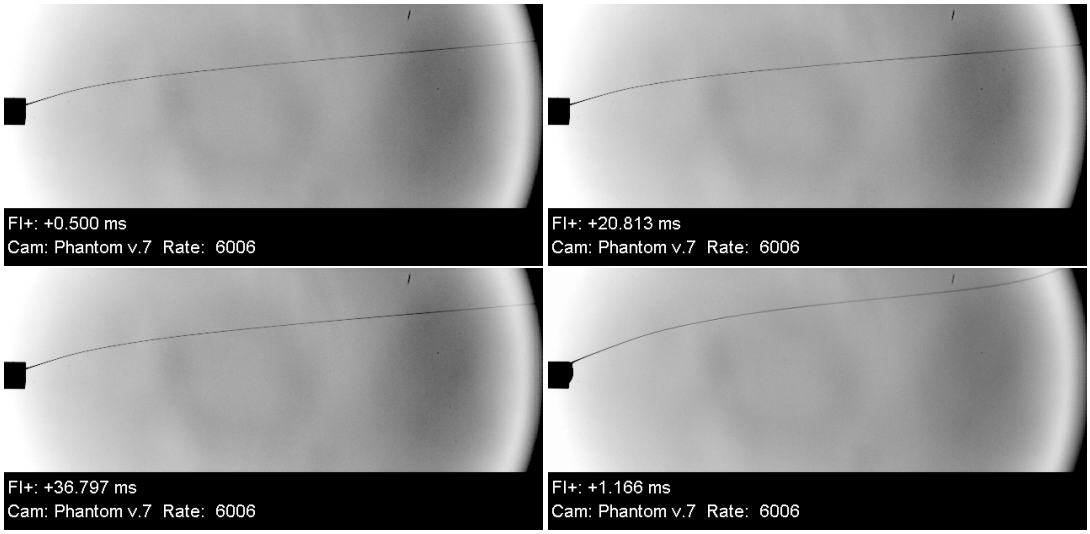

Figure 76. Images of an electrified jet at different times electrospun at 1.2mL/hr, 100kV/m and 3725Ga. The distance for the onset of the whipping instability is a) >31mm; b) >31mm; c) >31mm; d) >31mm. The average distance is >31mm.

APPENDIX II

Transmission electron microscopy of fibers electrospun from a PEO solution loaded with different magnetic materials.

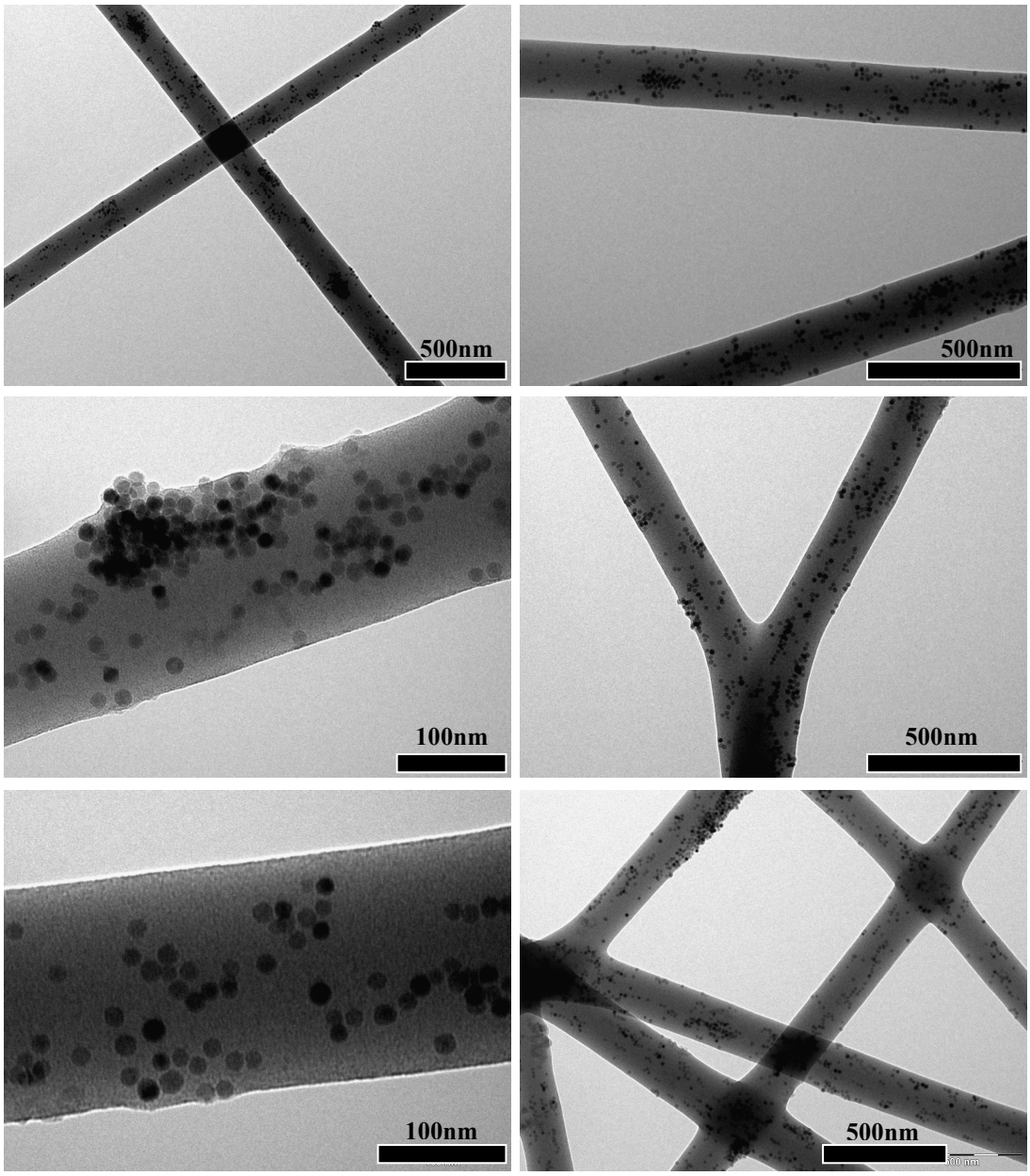

Figure 77. TEM micrographs of fibers electrospun from a PEO solution loaded with 0.04vol%$CoFe_2O_4$.

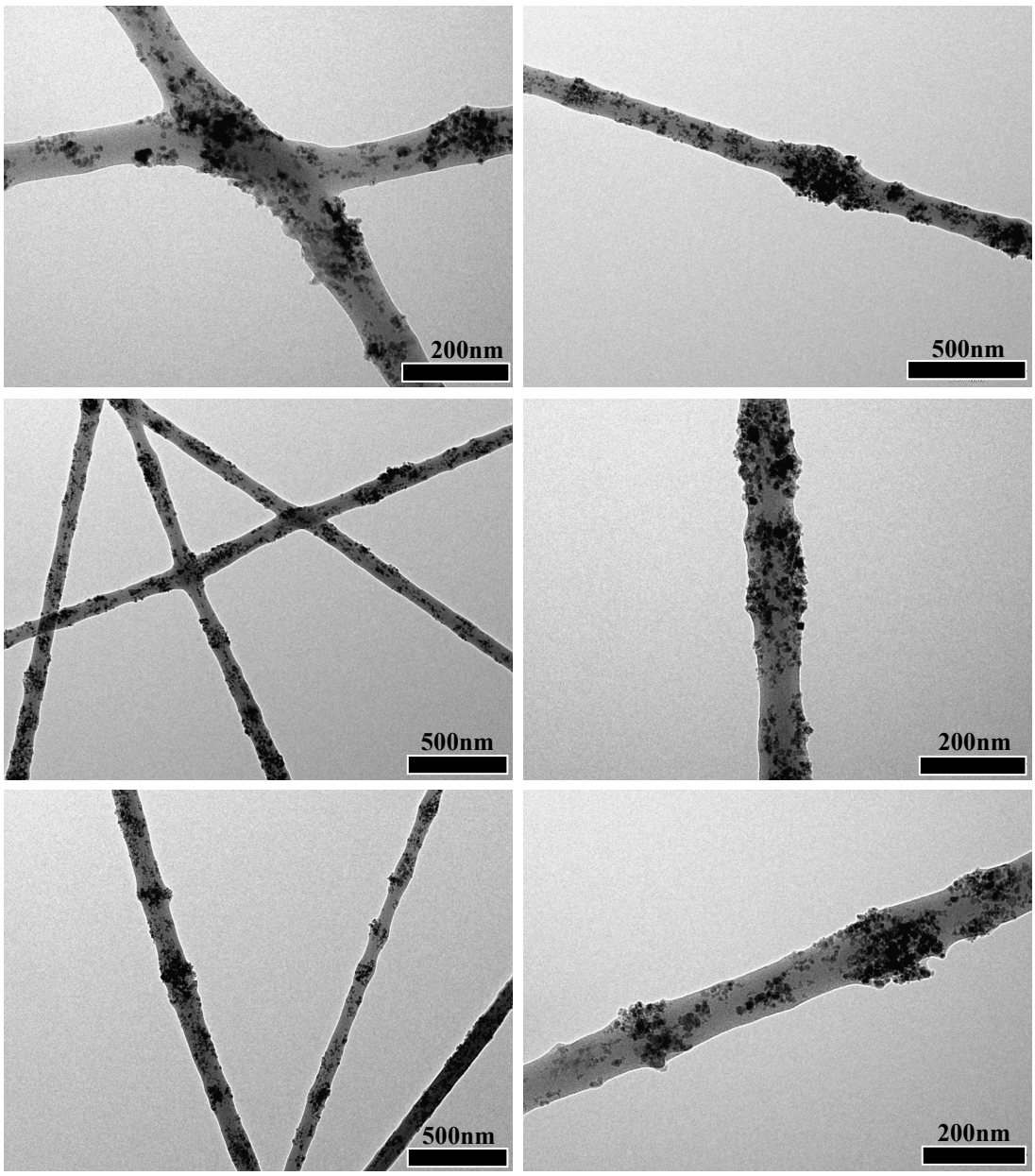

Figure 78. TEM micrographs of fibers electrospun from a PEO solution loaded with 0.04vol%Fe_3O_4

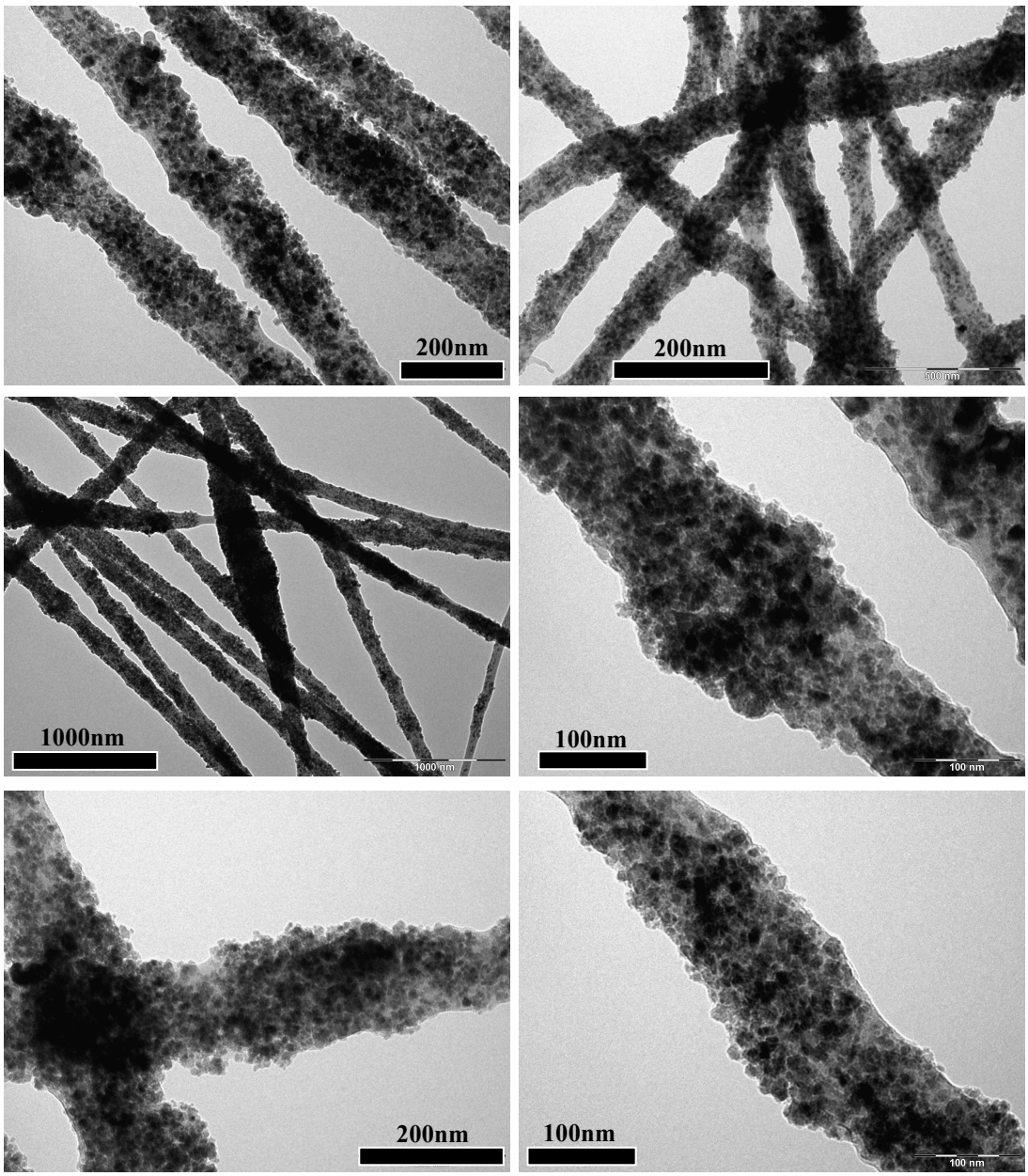

Figure 79. TEM micrographs of fibers electrospun from a PEO solution loaded with 0.2vol%Fe_3O_4.

REFERENCES

(1) Li, D.; Herricks, T.; Xia, Y. *Appl. Phys. Lett.* **2003***, 83*, 4586-4588.

(2) Pankaj Gupta, Ramazan Asmatulu, Rick Claus,Garth Wilkes, *J Appl Polym Sci* **2006***, 100*, 4935-4942.

(3) Gupta, A. K.; Gupta, M. *Biomaterials,* **2005***, 26*, 3995-4021.

(4) Barrera, C.; Gould, T.; Hyde, K.; Montero, G.; Hinestroza, J. P.; Rinaldi, C. *Proceedings of IMECE 2005* **2005**.

(5) Gupta, P.; Elkins, C.; Long, T. E.; Wilkes, G. L. *Polymer* **2005***, 46*, 4799-4810.

(6) Bacri, J. C.; Perzynksi, R.; Shliomis, M. I.; Burde, G. I. *Phys. Rev. Lett.* **1995***, 75*, 2128.

(7) McTague, J. P. *J. Chem. Phys.* **1969***, 51*, 133-136.

(8) Shliomis, M. I.; Morozov, K. I. *Phys. Fluids* **1994***, 6*, 2855-2861.

(9) Theron, S. A.; Zussman, E.; Yarin, A. L. *Polymer* **2004***, 45*, 2017-2030.

(10) Formhals, A. US Patent 2116942, 1938.

(11) Cui, W.; Li, X.; Zhou, S.; Weng, J. *J. Appl. Polym. Sci.* **2007***, 103*, 3105-3112.

(12) Ojha, S.; Afshari, M.; Kotek, R.; Gorga, R. *J Appl Polym Sci* **2008***, 108*, 308-319.

(13) Reneker, D. H.; Hou, H. In *Electrospinning;* Dekker Encyclopedia of Nanoscience and Nanotechnology; Marcel Dekker Inc.: New York, 2004; pp 543-550.

(14) Reneker, D. H.; Yarin, A. L. *Polymer* **2008***, 49*, 2387-2425.

(15) Burger, C.; Hsiao, B. S.; Chu, B. *Annu. Rev. Mater. Res.* **2006***, 36*, 333-368.

(16) Taylor, G. *Proceedings of the Royal Society of London. Series A, Mathematical and Physical Sciences* **1964***, 280*, 383-397.

(17) Tripatanasuwan, S.; Zhong, Z.; Reneker, D. H. *Polymer* **2007***, 48*, 5742-5746.

(18) Teo, W. E.; Ramakrishna, S. *Nanotechnology* **2006***, 17*, R89-R106.

(19) Young You,Seung Jin Lee Byung-Moo Min Won Ho Park *Journal of Applied Polymer Science* **2006***, 99*, 1214-1221.

(20) Reneker, D. H.; Yarin, A. L.; Fong, H.; Koombhongse, S. *J. Appl. Phys.* **2000***, 87*, 4531-4547.

(21) Hohman, M. M.; Shin, M.; Rutledge, G.; Brenner, M. P. *Phys. Fluids* **2001***, 13*, 2201-2220.

(22) Shin, Y. M.; Hohman, M. M.; Brenner, M. P.; Rutledge, G. C. *Polymer* **2001***, 42*, 09955-09967.

(23) Dersh, R.; Greiner, A.; Wendorff, J. H. In *Polymer Nanofibers Prepared by Electrospinning;* Dekker Enciclopedia of Nanoscience and Nanotechnology; Marcel Dekker, Inc: New York, 2004; pp 2931-2938.

(24) Reneker, D. H.; Chun, I. *Nanotechnology* **1996***, 7*, 216-223.

(25) Shin, Y. M.; Hohman, M. M.; Brenner, M. P.; Rutledge, G. C. *Appl. Phys. Lett.* **2001***, 78*, 1149-1151.

(26) Yarin, A. L.; Koombhongse, S.; Reneker, D. H. *J. Appl. Phys.* **2001***, 90*, 4836-4846.

(27) Thompson, C. J.; Chase, G. G.; Yarin, A. L.; Reneker, D. H. *Polymer* **2007***, 48*, 6913-6922.

(28) Deitzel, J. M.; Kleinmeyer, J.; Harris, D.; Beck Tan, N. C. *Polymer* **2001***, 42*, 261-272.

(29) Andrew, J. S.; Mack, J. J.; Clarke, D. R. *J. Mater. Res.* **2008***, 23*, 105.

(30) Zuo, W.; Zhu, M.; Yang, W.; Yu, H.; Chen, Y.; Zhang, Y. *Polym. Eng. Sci.* **2005***, 45*, 704-709.

(31) Wang, C.; Hsu, C.; Lin, J. *Macromolecules* **2006***, 39*, 7662-7672.

(32) Fong, H.; Chun, I.; Reneker, D. H. *Polymer* **1999***, 40*, 4585-4592.

(33) Rodriguez, F.; Cohen, C.; Ober, C. K.; Archer, L. A. In *Principles of Polymer Systems;* Taylor and Francis: New York, 2003; .

(34) McKee, M. G.; Wilkes, G. L.; Colby, R. H.; Long, T. E. *Macromolecules* **2004***, 37*, 1760-1767.

(35) Shenoy, S. L.; Bates, W. D.; Frisch, H. L.; Wnek, G. E. *Polymer* **2005***, 46*, 3372-3384.

(36) Bazbouz, M. B.; Stylios, G. K. *J. Appl. Polym. Sci.* **2008***, 107*, 3023-3032.

(37) Tan, S. H.; Inai, R.; Kotaki, M.; Ramakrishna, S. *Polymer* **2005***, 46*, 6128-6134.

(38) Wang, M.; Singh, H.; Hatton, T. A.; Rutledge, G. C. *Polymer* **2004***, 45*, 5505-5514.

(39) Lin, T.; Wang, H.; Wang, H.; Wang, X. *Nanotechnology* **2004***, 15*, 1375-1381.

(40) Ogata, N.; Shimada, N.; Yamaguchi, S.; Nakane, K.; Ogihara, T. *J. Appl. Polym. Sci.* **2007***, 105*, 1127-1132.

(41) Lyons, J.; Li, C.; Ko, F. *Polymer* **2004***, 45*, 7597-7603.

(42) Qin, X.; Yang, E.; Li, N.; Wang, S. *J. Appl. Polym. Sci.* **2007***, 103*, 3865-3870.

(43) Megelski, S.; Stephens, J. S.; Chase, D. B.; Rabolt, J. F. *Macromolecules* **2002***, 35*, 8456-8466.

(44) Eda, G.; Liu, J.; Shivkumar, S. *Mater. Lett.* **2007***, 61*, 1451-1455.

(45) Casper, C. L.; Stephens, J. S.; Tassi, N. G.; Chase, D. B.; Rabolt, J. F. *Macromolecules* **2004***, 37*, 573-578.

(46) Heikkila, P.; Taipale, A.; Lehtimaki, L.; Harlin, A. *Polym. Eng. Sci.* **2008***, 48*, 1168-1176.

(47) Aussawasathien, D.; Teerawattananon, C.; Vongachariya, A. *Journal of Membrane Science* **2008***, 315*, 11-19.

(48) Guo, B.; Zhao, S.; Han, G.; Zhang, L. *Electrochimica Acta* **2008***, 53*, 5174-5179.

(49) Matthews, J. A.; Wnek, G. E.; Simpson, D. G.; Bowlin, G. L. *Biomacromolecules* **2002***, 3*, 232-238.

(50) Yang, Y.; Jia, Z.; Li, Q.; Guan, Z. *IEEE Trans. Dielectr. Electr. Insul.* **2006***, 13*, 580-585.

(51) Blackwood, K. A.; McKean, R.; Canton, I.; Freeman, C. O.; Franklin, K. L.; Cole, D.; Brook, I.; Farthing, P.; Rimmer, S.; Haycock, J. W.; Ryan, A. J.; MacNeil, S. *Biomaterials* **2008***, 29*, 3091-3104.

(52) Yoshimoto, H.; Shin, Y. M.; Terai, H.; Vacanti, J. P. *Biomaterials* **2003***, 24*, 2077-2082.

(53) Ji, Y.; Li, B.; Ge, S.; Sokolov, J. C.; Rafailovich, M. H. *Langmuir* **2006***, 22*, 1321-1328.

(54) Ji Hye Hong, Eun Hwan Jeong, Han Sup Lee, Du Hyun Baik, Seung Won Seo,Ji Ho Youk, *Journal of Polymer Science Part B: Polymer Physics* **2005***, 43*, 3171-3177.

(55) Ju, Y.; Park, J.; Jung, H.; Cho, S.; Lee, W. *Materials Science and Engineering: B* **2008***, 147*, 7-12.

(56) Ju, Y.; Park, J.; Jung, H.; Cho, S.; Lee, W. *Composites Science and Technology* **2008***, 68*, 1704-1709.

(57) Wu, H.; Zhang, R.; Liu, X.; Lin, D.; Pan, W. *Chem. Mater.* **2007***, 19*, 3506-3511.

(58) McKee, M. G.; Hunley, M. T.; Layman, J. M.; Long, T. E. *Macromolecules* **2006***, 39*, 575-583.

(59) Seth D. McCullen, Kelly L. Stano, Derrick R. Stevens, Wesley A. Roberts, Nancy A. Monteiro-Riviere, Laura I. Clarke,Russell E.Gorga, *J Appl Polym Sci* **2007***, 105*, 1668-1678.

(60) X. Lu, Y. Zhao,C.Wang, *Adv Mater* **2005***, 17*, 2485-2488.

(61) Kakade, M. V.; Givens, S.; Gardner, K.; Lee, K. H.; Chase, D. B.; Rabolt, J. F. *J. Am. Chem. Soc.* **2007***, 129*, 2777-2782.

(62) Shao, C.; Kim, H.; Gong, J.; Ding, B.; Lee, D.; Park, S. *Materials Letters,* **2003***, 57*, 1579-1584.

(63) Lee, K. H.; Kim, H. Y.; Khil, M. S.; Ra, Y. M.; Lee, D. R. *Polymer,* **2003***, 44*, 1287-1294.

(64) Wu, H.; Zhang, R.; Liu, X.; Lin, D.; Pan, W. *Chem. Mater.* **2007***, 19*, 3506-3511.

(65) Guhados, G.; Wan, W.; Hutter, J. L. *Langmuir* **2005***, 21*, 6642-6646.

(66) Rinaldi, C.; Franklin, T.; Zahn, M.; Cader, T. In *Magnetic Nanoparticles in Fluid Suspension: Ferrofluid Applications*; Dekker Encyclopedia of Nanoscience and Nanotechnology; Marcel Dekker Inc.: New York, 2004; pp 543-550.

(67) Zeuner, A.; Richter, R.; Rehberg, I. *Journal of Magnetism and Magnetic Materials,* **1999***, 201*, 191-194.

(68) Chatterjee, J.; Haik, Y.; Chen, C. *J Magn Magn Mater* **2002***, 246*, 382-391.

(69) Kasap, S. O. In *Principles of Electronic Materials and Devices;* Mc. Graw Hill: New York, 2006; .

(70) Solymar, L.; Walsh, D. In *Electrical properties of materials;* Oxford University Press: Oxford, 2003; , pp 402.

(71) Friedman, J. F.; Voskoboynik, U.; Sarachik, M. P. *Phys. Rev. B* **1997***, 56*, 10793.

(72) Cabuil, V. *Dekker Encyclopedia of Nanoscience and Nanotechnology* **2004**, 1715.

(73) Ohring, M. In *Engineering Materials Science;* Academic Press: London, UK, 1995; .

(74) Zhang, D. *Dekker Encyclopedia of Nanoscience and Nanotechnology* **2004**.

(75) Rosenweig, R. E. In *Ferrohydrodynamics;* 1985; .

(76) Kobayashi, Y.; Horie, M.; Konno, M.; Rodriguez-Gonzalez, B.; Liz-Marzan, L. M. *J. Phys. Chem. B* **2003***, 107*, 7420-7425.

(77) Odenbach, S. In *Ferrofluids, Magnetically Controllable Fluids and Their Applications;* Lecture Notes in Physics; Springer: Germany, 2002; .

(78) Nedkov, I.; Merodiiska, T.; Slavov, L.; Vandenberghe, R. E.; Kusano, Y.; Takada, J. *Journal of Magnetism and Magnetic Materials,* **2006***, 300*, 358-367.

(79) Kim, D. K.; Zhang, Y.; Voit, W.; Rao, K. V.; Muhammed, M. *Journal of Magnetism and Magnetic Materials,* **2001***, 225*, 30-36.

(80) Jiang, W.; Yang, H. C.; Yang, S. Y.; Horng, H. E.; Hung, J. C.; Chen, Y. C.; Hong, C. *Journal of Magnetism and Magnetic Materials,* **2004***, 283*, 210-214.

(81) Vayssieres, L. *J. Colloid Interface Sci.* **1998***, 205*, 205-212.

(82) Bee, A.; Massart, R. *J Magn Magn Mater* **1995***, 149*, 6-9.

(83) Carpenter, E. E. *Journal of Magnetism and Magnetic Materials,* **2001***, 225*, 17-20.

(84) Pillai, V.; Shah, D. O. *Journal of Magnetism and Magnetic Materials,* **1996***, 163*, 243-248.

(85) O'Connor, C. J.; Kolesnichenko, V.; Carpenter, E.; Sangregorio, C.; Zhou, W.; Kumbhar, A.; Sims, J.; Agnoli, F. *Synthetic Metals,* **2001***, 122*, 547-557.

(86) Zhou, W. L.; Carpenter, E. E.; Lin, J.; Kumbhar, A.; Sims, J.; O'Connor, C. J. *The European Physical Journal D - Atomic, Molecular, Optical and Plasma Physics* **2001***, 16*, 289-292.

(87) Y. Lee, J. Lee, C. J. Bae, J.-G. Park, H.-J. Noh, J.-H. Park,T.Hyeon, *Advanced Functional Materials* **2005***, 15*, 503-509.

(88) Kim, D. K.; Mikhaylova, M.; Zhang, Y.; Muhammed, M. *Chem. Mater.* **2003***, 15*, 1617-1627.

(89) Wang, J.; Deng, T.; Lin, W.; Yang, C.; Zhan, W. *J. Alloys and Comp.* **2008***, 450*, 532-539.

(90) Liu, Q.; Sun, J.; Long, H.; Sun, X.; Zhong, X.; Xu, Z. *Materials Chemistry and Physics,* **2008***, 108*, 269-273.

(91) Ban, Z.; Barnakov, Y. A.; Golub, V. O.; O'Connor, C. J. *Journal of materials chemistry* **2005***, 15*, 4660-4662.

(92) Ban, I.; Drofenik, M.; Makovec, D. *Journal of Magnetism and Magnetic Materials,* **2006***, 307*, 250-256.

(93) Hochepied, J. F.; Pileni, M. P. *J. Appl. Phys.* **2000***, 87*, 2472-2478.

(94) Dale L. Huber, *Small* **2005***, 1*, 482-501.

(95) Odenbach, S. *J. Phys. Condens. Matter.* **2004***, 16*, R1135-R1150.

(96) Huang, K.; Ehrman, S. H. *Langmuir* **2007***, 23*, 1419-1426.

(97) Butter, K.; Philipse, A. P.; Vroege, G. J. *Journal of Magnetism and Magnetic Materials,* **2002***, 252*, 1-3.

(98) Shafi, K. V. P. M.; Gedanken, A.; Prozorov, R.; Balogh, J. *Chem. Mater.* **1998***, 10*, 3445-3450.

(99) Burke, N. A. D.; Stover, H. D. H.; Dawson, F. P. *Chem. Mater.* **2002***, 14*, 4752-4761.

(100) Koltypin, Y.; Fernandez, A.; Rojas, T. C.; Campora, J.; Palma, P.; Prozorov, R.; Gedanken, A. *Chem.Mater.* **1999***, 11*, 1331-1335.

(101) de Caro, D.; Bradley, J. S. *Langmuir* **1997***, 13*, 3067-3069.

(102) Ely, T. O.; Amiens, C.; Chaudret, B.; Snoeck, E.; Verelst, M.; Respaud, M.; Broto, J. -. *Chem. Mater.* **1999***, 11*, 526-529.

(103) Osuna, J.; de Caro, D.; Amiens, C.; Chaudret, B.; Snoeck, E.; Respaud, M.; Broto, J. -.; Fert, A. *J. Phys. Chem.* **1996***, 100*, 14571-14574.

(104) Jeyadevan, B.; Shinoda, K.; Justin, R. J.; Matsumoto, T.; Sato, K.; Takahashi, H.; Sato, Y.; Tohji, K. *Magnetics, IEEE Transactions on* **2006***, 42*, 3030-3035.

(105) Bonder, M. J.; Zhang, Y.; Kiick, K. L.; Papaefthymiou, V.; Hadjipanayis, G. C. *Journal of Magnetism and Magnetic Materials,* **2007***, 311*, 658-664.

(106) Petit, C.; Taleb, A.; Pileni, M. P. *J Phys Chem B* **1999***, 103*, 1805-1810.

(107) Sun, S.; Murray, C. B. *J. Appl. Phys.* **1999***, 85*, 4325.

(108) Zubris, M.; King, R. B.; Garmestani, H.; Tannenbaum, R. *J. Mater. Chem.* **2005***, 15*, 1277.

(109) Sun, S.; Murray, C. B.; Weller, D.; Folks, L.; Moser, A. *Science* **2000***, 287*, 1989-1992.

(110) Chinnasamy, C. N.; Jeyadevan, B.; Shinoda, K.; Tohji, K. *J. Appl. Phys.* **2003***, 93*, 7583-7585.

(111) Chaubey, G. S.; Barcena, C.; Poudyal, N.; Rong, C.; Gao, J.; Sun, S.; Liu, J. P. *J. Am. Chem. Soc.* **2007***, 129*, 7214-7215.

(112) Elkins, K. E.; Vedantam, T. S.; Liu, J. P.; Zeng, H.; Sun, S.; Ding, Y.; Wang, Z. L. *Nano Lett.* **2003***, 3*, 1647-1649.

(113) D. Kodama, K. Shinoda, K. Sato, Y. Konno, R. J. Joseyphus, K. Motomiya, H. Takahashi, T. Matsumoto, Y. Sato, K. Tohji,B.Jeyadevan, *Adv Mater* **2006***, 18*, 3154-3159.

(114) Fu, W.; Yang, H.; Hari-Bala; Liu, S.; Li, M.; Zou, G. *Materials Chemistry and Physics,* **2006***, 100*, 246-250.

(115) Aslam, M.; Fu, L.; Li, S.; Dravid, V. P. *Journal of Colloid and Interface Science,* **2005***, 290*, 444-449.

(116) Liu, Z. L.; Ding, Z. H.; Yao, K. L.; Tao, J.; Du, G. H.; Lu, Q. H.; Wang, X.; Gong, F. L.; Chen, X. *Journal of Magnetism and Magnetic Materials,* **2003***, 265*, 98-105.

(117) Lattuada, M.; Hatton, T. A. *Langmuir* **2007***, 23*, 2158-2168.

(118) C. Flesch, C. Delaite, P. Dumas, E. Bourgeat-Lami,E.Duguet, *Journal of Polymer Science Part A: Polymer Chemistry* **2004***, 42*, 6011-6020.

(119) Chen, H.; Snyder, J. D.; Elabd, Y. A. *Macromolecules* **2008***, 41*, 128-135.

(120) Sahoo, Y.; Pizem, H.; Fried, T.; Golodnitsky, D.; Burstein, L.; Sukenik, C. N.; Markovich, G. *Langmuir* **2001***, 17*, 7907-7911.

(121) Portet, D.; Denizot, B.; Rump, E.; Lejeune, J.; Jallet, P. *Journal of Colloid and Interface Science,* **2001***, 238*, 37-42.

(122) Lin, J.; Zhou, W.; Kumbhar, A.; Wiemann, J.; Fang, J.; Carpenter, E. E.; O'Connor, C. J. *Journal of Solid State Chemistry,* **2001***, 159*, 26-31.

(123) Bao, Y.; Krishnan, K. M. *Journal of Magnetism and Magnetic Materials,* **2005***, 293*, 15-19.

(124) Iglesias-Silva, E.; Rivas, J.; León Isidro, L. M.; López-Quintela, M. A. *Journal of Non-Crystalline Solids,* **2007***, 353*, 829-831.

(125) Gohy, J. -.; Varshney, S. K.; Jerome, R. *Macromolecules* **2001***, 34*, 3361-3366.

(126) Aqil, A.; Vasseur, S.; Duguet, E.; Passirani, C.; Jerome, R.; Jerome, C. *J. Mater. Chem.* **2008***, 18*, 3352-3360.

(127) Barrera, C.; Herrera, A. P.; Rinaldi, C. *J. Colloid Interface Sci.* **2009***, 329*, 107-113.

(128) Willis, A. L.; Turro, N. J.; O'Brien, S. *Chem. Mater.* **2005***, 17*, 5970-5975.

(129) Rosensweig, R. E.; Kaiser, R.; Miskolczy, G. *J. Colloid Interface Sci.* **1969***, 29*, 680-686.

(130) Shliomis, M. I. *Sov. Phys. JETP* **1972***, 34*, 1291-&.

(131) Odenbach, S. In *Magnetoviscous Effects in Ferrofluids;* Lecture Notes in Physics; Springer: Germany, 2002; .

(132) Hall, W. F.; Busenberg, S. N. *J. Chem. Phys.* **1969***, 51*, 137-144.

(133) Zeuner, A.; Richter, R.; Rehberg, I. *Phys. Rev. E* **1998**, *58*, 6287.

(134) Zubarev, A.; Iskakova, L. *Physical Review E* **2000**, *61*, 5415-5421.

(135) Zubarev, A. Y.; Fleischer, J.; Odenbach, S. *Physica A: Statistical Mechanics and its Applications,* **2005**, *358*, 475-491.

(136) Zubarev, A. Y.; Odenbach, S.; Fleischer, J. *Journal of Magnetism and Magnetic Materials,* **2002**, *252*, 241-243.

(137) Park, J.; An, K. J.; Hwang, Y. S.; Park, J. G.; Noh, H. J.; Kim, J. Y.; Park, J. H.; Hwang, N. M.; Hyeon, T. *Nature Mater.* **2004**, *3*, 891.

(138) Barrera, C.; Herrera, A.; Zayas, Y.; Rinaldi, C. *J. Magn. Magn. Mater.* **2009**, *321*, 1397-1399.

(139) Kanwal, F.; Liggat, J. J.; Pethrick, R. A. *Polym. Degrad. Stab.* **2000**, *68*, 445-449.

(140) Mehrdad, A.; Rostami, M. R. *Iran. Polym. J.* **2007**, *16*, 795.

(141) Desai, V.; Shenoy, M. A.; Gogate, P. R. *Chemical Engineering and Processing: Process Intensification* **2008**, *47*, 1451-1455.

(142) Taghizadeh, M. T.; Asadpour, T. *Ultrason. Sonochem.* **2009**, *16*, 280-286.

(143) Harkal, U. D.; Gogate, P. R.; Pandit, A. B.; Shenoy, M. A. *Ultrason. Sonochem.* **2006**, *13*, 423-428.

(144) Ebagninin, K. W.; Benchabane, A.; Bekkour, K. *J. Colloid Interface Sci.* **2009**, *336*, 360-367.

(145) Morrison, F. A. In *Understanding Rheology;* Oxford University Press, Inc.: United States, 2001; .

(146) Mackay, M. E.; Tuteja, A.; Duxbury, P. M.; Hawker, C. J.; Van Horn, B.; Guan, Z.; Chen, G.; Krishnan, R. S. *Science* **2006**, *311*, 1740-1743.

(147) Tuteja, A.; Mackay, M. E.; Hawker, C. J.; Van Horn, B. *Macromolecules* **2005**, *38*, 8000-8011.

(148) Devanand, K.; Selser, J. C. *Macromolecules* **1991**, *24*, 5943-5947.

(149) Tuteja, A.; Duxbury, P. M.; Mackay, M. E. *Macromolecules* **2007**, *40*, 9427-9434.

(150) Uyar, T.; Besenbacher, F. *Polymer* **2008***, 49*, 5336-5343.